THÈSE

PRÉSENTÉE A

L'UNIVERSITÉ BORDEAUX 1

ÉCOLE DOCTORALE DES SCIENCES PHYSIQUES ET DE L'INGENIEUR

Présentée par:

Thi Ngoc Huyen TRAN

POUR OBTENIR LE GRADE DE

DOCTEUR

SPÉCIALITÉ : MECANIQUE

STUDY OF COMPRESSION BEHAVIOR OF WOOD-BASED FIBERBOARD: CHARACTERIZATION FROM NON-DESTRUCTIVE IMAGE TECHNIQUES

Directeur de Recherche : Christine DELISEE
Pascal DOUMALIN

Soutenue le : 03/12/2012

Devant la commission d'examen formée de :

M.	JEULIN Dominique	Professeur, Mines ParisTech, Paris	Rapporteur
Mme.	POQUILLON Dominique	Professeur, Cirimat-Ensiacet, Toulouse	Rapporteur
M.	BERNARD Dominique	Directeur de Recherche, ICMCB, Bordeaux	Examinateur
M.	CLOUTIER Alain	Professeur, Université Laval, Québec	Examinateur
Mme.	DELISEE Christine	Professeur, Bordeaux Sciences Agro, Bordeaux	Superviseur
M.	DOUMALIN Pascal	Maître de Conférences, Institut P', Poitiers	Superviseur
M.	IRLE Mark	Professeur, ESB, Nantes	Examinateur
M.	LUX Jérôme	Maître de Conférences, Université La Rochelle	Examinateur

Résumé/Summary

La thèse a pour but de caractériser les propriétés mécaniques de matériaux à base de fibres de bois en relation avec leur microstructure complexe. Ce type de matériau est hétérogène à différentes échelles : à l'échelle microscopique de la fibre, à l'échelle mésoscopique du réseau des fibres et à l'échelle macroscopique du matériau. Pour observer ces hétérogénéités, différents moyens expérimentaux de caractérisation sont utilisés, notamment la microtomographie aux rayons X et la corrélation d'images volumiques. Ces deux techniques permettent à la fois de numériser les différentes fibres à l'échelle microscopique dans le volume, et d'obtenir le champ tridimensionnel de déformation à coeur. Comme résultats, le matériau étudié montre un comportement non-linéaire avec une déformation résiduelle et un effet d'hystérésis en charge/décharge, qui suit le modèle de Van-Wyk. A l'échelle microscopique, le champ de déformation 3D fortement hétérogène est intimement lié aux porosités locales.

This thesis aims at characterizing the mechanical properties of wood-based fibrous material in relation with the intrinsic properties of fibers and the complex architecture of random fibrous assembly. This material, whose characteristics strongly depend on its configuration, is heterogeneous at different scales: microscopic scale of individual fibers, mesoscopic scale of fiber assembly and macroscopic scale of material. To observe these heterogeneities, different experimental characterization methods are used, especially X-ray microtomography and Digital Volume Correlation. These techniques allow us to visualize and digitize the spatial position of different phases of material at microscopic scale and the full 3D strain field inside the material. The results are: the material shows a non-linear mechanical behavior with hysteresis and residual deformation respecting Van Wyk's model. At microscopic scale, the 3D strain field is strongly heterogeneous and related to local porosities.

Mots clés/Key words

Matériau fibreux, Bois, Compression, Microtomographie, Corrélation d'image volumique, Caractérisation microstructurale, Champs de déformation 3D

Fibrous material, Wood, Compression, Microtomography, Digital volume correlation, Microstructural characterization, 3D full field strain.

ACKNOWLEDGEMENT

I would like to express my deepest appreciation to my supervisors, Christine DELISEE and Pascal DOUMALIN for their valuable guidance with their deep research knowledge while giving me the most autonomy, for their countless encouragement not only in research but also in life, and, their no-giving-pressure attitude that gave me more pressure than usual.

I wish to express my sincere gratitude to Professor Dominique POQUILLON and Professor Dominique JEULIN for being my reviewers for thesis defences, their remarks will be valuable for my future research.

My gratitude also goes to Professor Dominique BERNARD, Professor Alain CLOUTIER and Professor Mark IRLE for being committee members.

I also wish to thanks my tutors, Jérôme MALVESTIO, Jean-Christophe DUPRE and Arnaud GERMANEAU for all technical support, discussions and for offering a friendly, humorous and quite solid team even though it is hard for me solely to battle against.

This thesis is my deepest thank to Patrick CASTERA who gives me warm and care like a father when I live and study in France

Thanks are also due to Philippe TARIS and Bernard SOLBES for helping me with all my tests at I2M, to Michel CHASSAGNE who is always smiling and shining, for being my "living library", to Christophe FERNANDEZ, for solving all problems of my computer, to Amadou NDIAYE, Franck TAILLANDIER, Kamal KANSOU for sharing with me excellent moments at laboratory. I would also like to thank my other colleagues at the GCE laboratory for their support.

I would like to extend my heartfelt to my parents, my sisters for giving me unlimited encouragement, understanding and love.

Finally, for my husband, Anh PHAN, there are really no words or no ways for me to express my appreciation for him being always where my eye can see, for his endless love, his non-stop support and sacrifice and his unbelievable understanding without which none of this would have been materialized.

Dedication

For my beloved parents, my sisters, my dearest husband, Anh PHAN and for my angel son, Hong Dat...

TABLE OF CONTENT

Introduction

Wood-based fibrous materials play an important role in various industrial applications, especially for building, as thermal, acoustic insulators, deformable structures. The desire to find good, new industrial products must be based on available and abundant resources as wood fibers in the Aquitaine region. A nonwoven textile process has been adapted for wood fibers, making use of new properties of wood fibers when mixed with textile fibers. The obtained material possesses good strength, good thermal performance and is environmentally friendly but gives back a strongly complex structure.

Commercial products of the wood-based fibrous material, that have a similar structure and constitution, are used as interior roof, interior walls, intermediate floors and interior partitions. A number of studies concentrate on the thermal and acoustic properties of the materials. However, it is easy to see that some mechanical solicitations may affect these thermal properties. For example, during transportation, storage or execution on the construction site, the fiberboards are always compressed to a certain level. If the compression is too high and the sample does not recover its initial thickness, the thickness reduction leads certainly to a cut off in thermal insulation capacity. The question is raised: at what level of compression, can the material recover and maintain its initial properties after unloading? This subject is quite interesting and challenging as it attacks in the same time mechanical behavior and thermal characteristics of the material as well as the time-and-loading-dependent characteristics of the sample thickness recovery (a property of viscoelastic material). This thesis is a preliminary step in understanding how the material responds to compressive solicitations by identifying the local strain mechanisms as a function of the microstructure evolution.

The compressive behavior of the fibrous materials is an issue which has challenged research scientists for many years since 1946 with Van Wyk's study. Other studies have been proceeded by developing Van Wyk's model and improving its limitations. The model, which is based on modelling fiber contacts and other properties such as fiber length between contacts, fiber segment behavior or Young's modulus, is still valid today. The fact that there are still many researchers using Van Wyk's model in their studies of various fibrous materials shows that this model may still be efficiently applied and gives good results for a new and complex fibrous material as a preliminary step for further research. However, even though these models are considered as micromechanical models, at the time of Van Wyk and even later in the 1980s, accessing to the real microstructure of the material was impossible or very complex process. Consequently, the microstructure is simplified

through statistical and probabilistic approaches. Then Young's modulus was also derived from statistical and probabilistic analysis of fiber contacts, fiber length and fiber section. Plus, major studies have been carried out on fibrous networks that have fibers of constant section and constant length. Quite a few studies are actually devoted to the mechanical behavior for complex structure as in wood-based fibrous materials. However, a pure wood network similar to that extracted from studied material does not exist in reality. So even if there are a number of studies on textile or polymer fiber assembly, we cannot deduce the behavior of real material by superposing the existing models of each fiber network. The challenge is that we must study the configuration of the whole system while trying to clarify the distribution of each fiber population.

So, we can say that the two most important keys for understanding the compressive behavior of fibrous assemblies are structural characterization and mechanical modeling. The first key focuses on the geometrical and physical properties of fiber architecture such as fiber orientation, fiber diameter and pore distribution. For 3D microstructure, these characteristics are extracted from tomographic images obtained from compression tests under X-ray microtomography, a technique employed to observe *in situ* the evolution of the microstructure related to its mechanical solicitations. The microstructural properties are analysed thanks to mathematical morphological operations. The second key aims at a multiscale mechanical modelization. Macroscopic behavior of fibrous assembly can be splendidly found in the literature by many theoretical and experimental studies. Fibrous materials, regardless of the material constitution and configuration, all exhibit non-linear behavior with hysteresis and residual deformation. So some modeling may be actually applied for different fibrous assemblies. However, as one cannot be satisfied with macroscopic behavior, researchers have always aimed at understanding what happens inside the material with early technique named the finite element method, and then later with the image correlation technique. Digital image correlation (DIC) and Digital volume correlation (DVC) are two techniques based on the same root, the image correlation technique, allowing us to access strain characterization at a much smaller scale. DVC is the 3D extension of DIC which was originally applied to measure displacement and strain fields on the surface of the sample during mechanical solicitations. DVC and 3D mark tracking method, beside the finite element method, are two other approaches for 3D analysis. However, the 3D mark tracking method requires regular marks to be tridimentionally distributed inside the

material, which is difficult to be obtained without modifying the material. Thereby, DVC is actually the most recent technique enabling us to study the 3D strain field inside a material or a structure at the scale of several micrometers which has been applied to analyse and characterize several heterogeneous materials and recently fibrous materials.

The main objective of this thesis is to construct a multiscale methodology for studying the compressive behavior of wood-based fibrous material as a function of the microstructure by connecting different approaches: theory, experimentation, simulation. Three scales are considered: the macroscopic scale which gives the unidirectional global response of the material; the mesoscopic scale which demonstrates the 2D behavior on the sample surface at more local zones in order to investigate the influence of local structure on local response of the material; however, as the studied material is strongly 3D heterogeneous, 2D information becomes insufficient, 3D study at the microscopic scale, which refers to the arrangement of individual fibers in a zone of order of several micrometers, is required. This latest study is performed inside the material in order to eliminate the edge effect because of the softness, the flexibility and the complexity of the material. This ultimate objective can be detailed by following main objectives which are presented in the order in which they are discussed in this dissertation:

Constructing a multiscale experimental methodology for wood-based fiberboards: at the macroscopic scale, the global behavior obtained from classical uniaxial compression tests on sample respecting adequate norms. At the mesoscopic scale, compression tests under CCD cameras are carried out. At the microscopic scale, compression tests under microtomography X-ray are conducted. These tests are carried out taking into account the difficulties coming from the complex structure of the material by creating a test set-up adapted to this kind of material, so that we can obtain the most correct experimental results.

Characterizing the microstructure of fiber assembly thanks to the theory of mathematical morphology. Segmentation of wood fibers from textile fibers allows us to extract information of the microstructure not only of the whole sample but also of each different fiber population such as fiber diameters, pore sizes, fiber orientations.

Determining the mechanical behavior of the material at different scales by means of different techniques: the stress-strain relationship at the macroscopic scale which is next fitted to several theoretical and experimental models where Van

Wyk's model gives the best agreement with experimental data; at the mesoscopic scale, the full strain field on the sample surface is obtained by the DIC method; finally, at the microscopic scale, the 3D full strain field is obtained using DVC.

Establishing the relationship between the local strain field and microstructural properties. Here, we expand on previous work of structure at the global scale (whole sample) by focusing on the microstructure at the microscopic scale of some micrometers. The comprehension of the mechanical behavior necessitates the analysis of the microstructure and the role of each material phase since each phase has its own structure functions. Comprehension of the underlying structure is an important step to understand, to control and to predict material behavior or applications.

Proposing a simple expression of Young's modulus at the macroscopic and microscopic scale through numerical simulation using the finite element method implemented in Cast3M software. The model and input parameters used in Cast3M are assumed from global behavior and from microstructural analysis. The longest interest of simulation is to confirm and validate our hypothesis about the influence of the microstructure not only on the 3D local strain field but also on the whole sample.

The thesis is organised into six chapters:

Chapter I of the thesis is an overview of the relevant approaches to the mechanical characterization of fibrous assemblies, not forgetting the introduction of the studied material and its elaboration process in section I.1. Section I.2 discusses several approaches to the mechanical characterization of fibrous assembly. Three main approaches are presented: theoretical approaches which focus on Van Wyk's model, experimental approaches on stress-strain relation and full strain field characterization based on the image correlation techniques (digital image correlation for the 2D strain field and digital volume correlation for the 3D strain field). Section I.3 describes recent observation methods in which optical microscopy, SEM and X-ray microtomography are discussed.

Chapter II is destined to describe the studied material with its properties which will be a reference for morphological studies in chapter IV.

Chapter III describes experimental procedures for compression tests at different scales and the measurement methods of strain field by the image correlation technique. Section III.1 gives a general description of the methodology as well as of test protocol. Section III.2 describes the sample preparation procedure

since it is complicated for samples to be prepared. The whole of section III.3 enters into the detail of all compression tests: test set-up, test preparation, test execution and the volume extraction from tomographic images which will be exploited with digital volume correlation for strain field determination and for microstructural analysis. Section III.4 gives the detail of measurement methods of strain field by image correlation.

Chapter IV focuses purely on microstructural analysis: a brief description of mathematical morphology, essential since it is the theoretical base of all structure operations, is presented is section IV.1. Section IV.2 describes structure operations such as the segmentation of the fibrous/porous phase, lumen filling and the separation of wood fibers from PES fibers where the latest is the most concentrated on. The advantages and limitations of each operation are discussed. Section IV.3 follows section IV.2 by giving the principle of morphological measurements on microstructure properties such as: fiber diameters, pore sizes, fiber orientation etc. for whole fiber assembly and for the wood or the PES network.

Chapter V presents the results of mechanical characterization in four correlated sections: section V.1 describes the stress-strain relation at the global scale which is then examined and validated with Van-Wyk's theory. The superposition of stress-strain curves of different samples is also carried out to validate the chosen sample size in CT-test. Section V.2 presents the results of the 2D strain field of the sample surface thanks to digital image correlation (DIC) which is validated by the mark tracking method. In this chapter, we propose and validate the image correlation method as a good technique for obtaining the strain characterization of wood-based fibrous material. We can say that DIC is a preliminary step for digital volume correlation analysis from which the results and analysis is fully presented in section V.4.

Chapter VI concentrates on establishing the relation between mechanical behavior and microstructural characteristics; it is the most important part of the thesis. Section VI.1 exploits this relation at the macroscopic scale. Section VI.2 studies the relation at the microscopic scale, using the 3D full strain field. For both sections VI.1 and VI.2, four microstructure properties taken into consideration are fiber volume fraction, fiber/pore size, fiber/pore spatial distribution and fiber local orientation. Section VI.3 initiates preliminary studies in computational simulation based on experimental and structural results to find an expression of the local

Young's modulus (at the microscopic scale) which can be deduced from the Young's modulus at the macroscopic scale.

Chapter I: Literature review- Materials and Methods

I.1 Wood fibers and elaboration processes of fiberboards

Fibers have been used in textile and materials for a long time. The Egyptians had known the existence of cotton fibers since 12000 years B.C. These fibers were used to make fabrics for at least 7000 years. Today, a whole host of different fibers are used in textile industry (cotton, wool, silk, etc.), for material reinforcements (plastic fibers, metal fibers…), for thermal or acoustic insulation (glass fibers, mineral fibers, wood fibers…) etc. A survey led by the INRS (Institut National de Recherche et de Sécurité) in 2008 on fiber quantity/ types, fiber exploitation, fiber applications even the fiber-based activities of French businesses, found that 93% of natural vegetable-origin fibers are wood fibers and 68% of organic fibers derived from polymer family come from polyester fibers [1]. These two types of fibers possess great advantages such as low-cost and high specific mechanical strength. Wood fibers are well-known for their good impact to ecological environment as well as non-polluting and recyclable materials.

I.1.1 Wood fibers

Wood fibers are obtained from defibration of wood using chemical or mechanical processing. Its specific properties come from the fiber wall and the internal lumens which assure liquid transport in wood. Differencies are particularly evident in softwoods, where cell walls are much thinner and lumens are much larger in the spring (earlywood) (Figure I.1).

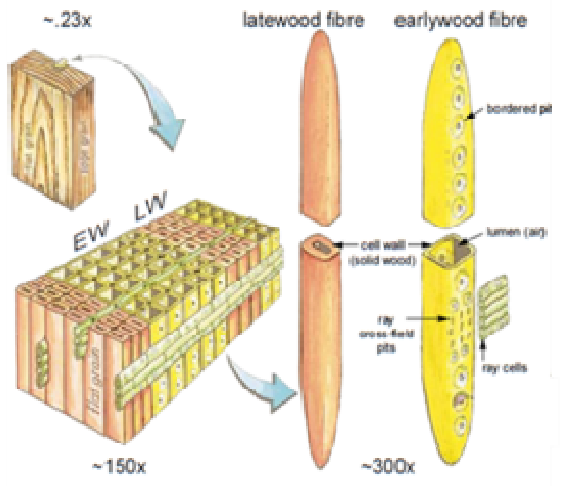

(a) (b)

Figure I.1: Wood fiber in earlywood and latewood [2]

The cell wall consists of hemicellulose (25-40%), lignin (20-35%) and mainly cellulose (40-50%) in the form of microfibrils, whose sections, thickness and

orientation, along with fiber defects, determine the mechanical properties of wood fibers [3], [4]. In addition to this, wood fibers show a great variability in terms not only of its morphology but also of properties between different wood species, among a wood specie, inside the same tree (i.e. juvenile and mature wood, normal and reaction wood, early and late wood) and inside individual wood fiber (i.e. each wood fiber introduces a different variation of microfibril orientation) (Figure I.2). As presented in Figure I.3, the tensile Young's modulus of fiber dramatically decreases with the increase of the microfibril angle in the S2 layer (Figure I.3).

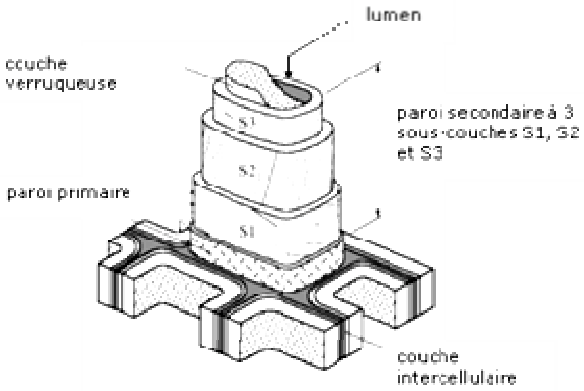

Figure I.2: Schematic illustration of a wood fiber [5]

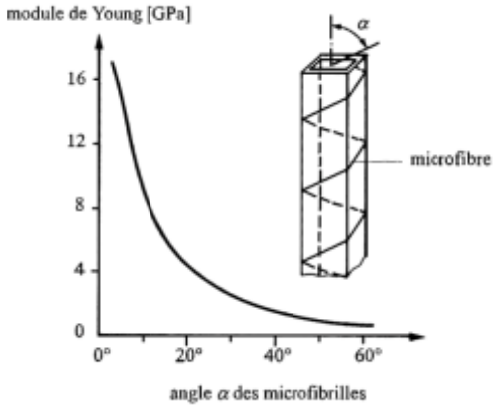

Figure I.3: Elasticity modulus at different angle of wood microfibril in spring [6]

A major part of wood fibers are used in the paper industry which is manufactured through a wetlaid process into paper sheets. Wood fibers are also found in combination with other materials to create fiberboards in engineering (i.e. MDF, hardboard), wood/thermoplastic composites using wood fibers as reinforcement by replacing traditional fibers such as mineral fibers or glass fibers, to be used as thermal insulators for building major constitution such as walls and floors (i.e. Sylvactis produced by ACTIS society). It is all thanks to wood fibers

possessing good mechanical properties (Figure I.4) [7], easily manufactured and shaped while remaining light and inexpensive. Some characteristics of natural fibers are presented in Table I.1.

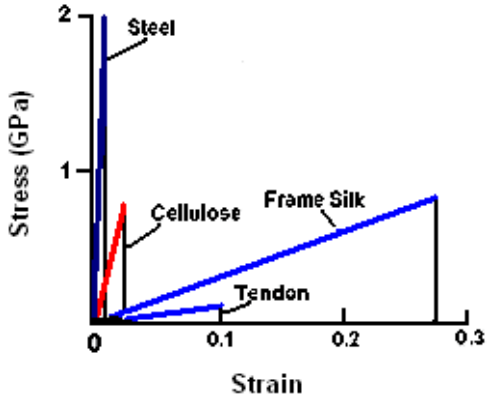

Figure I.4: Tensile stress-strain curve of cellulose compared to different materials[7]

Table I.1: Properties of some natural fibers [8], [9]

Fiber	Length (mm)	Diameter (µm)	Tensile modulus (GPa)	Maximum deformation (%)
Cotton	25	12 - 25	6 - 10	6 - 8
Linen	4 - 8.5	12 - 30	50- 70	1.3 - 3.3
Hemp	5 - 40	16 - 50	30 - 60	1.7 - 2.1
Sisal	100 125	100 - 400	9 -22	3 - 14
Banana	4.5 - 10	50 -250	7 - 20	1.8 - 3.5
Wood	1 - 7	15 - 65	10 - 80	

I.1.2 Different processes for the elaboration of wood-based fiberboards

Wood-based fiberboards can be elaborated using two classical processes: the wet process (which is close to the process used in the paper industry) and the dry process which necessitates the presence of thermosetting resin to ensure the cohesion between fibers [10]. The wet process requires a large volume of water, which is then classified into polluting categories. The wood fibers are obtained by thermo-mechanical defibration of 30g of dry wood chips with 1 litre of water at a

temperature of 160°C and a saturated vapour of 7 bars. The cohesion in this kind of fiberboard is achieved essentially through the presence of hydraulic group -OH at the nanometric scale. The fiberboard has a quite homogenous density along its thickness and fibers are basically oriented in a privileged direction, parallel to the board faces.

The dry process, on the contrary, demands thermosetting resin in the process to insure fiber cohesion. The wood fibers obtained in this procedure are much shorter than those in the previous procedure. Wood fibers are sprayed under pressure with about 12% resin. Then it is mixed cold, distributed and pre-consolidated inside a cold press. Finally, the mat is pressed to achieve the desired thickness and to ensure fiber cohesion by polymerization of the adhesive. The fiber density is higher at the two surfaces and fibers have the tendency to orient perpendicularly to the press direction (Figure I.7a).

The nonwoven process, which is an adaptation of textile process to wood fibers, allows us to produce a 3D structure of great thickness with very weak density while assuring a very good cohesion between fibers. The nonwoven process has overcome the limitations of the two previous processes: specimen thickness is no longer limited and reduced density no longer causes the decreasing in fiber cohesion. Although these products are soft, porous and voluminous, it requires much less material (fiber) to form a stable structure, compared to granular porous media requiring more material (granules) to form a comparably stable structure. This characteristic allows nonwoven products possessing strong insulation performance as thermal insulators. Normally, nonwoven materials obtained from the dry process (drylaid) are much lighter and have better thermal performance than nonwoven products obtained from the wet process (wetlaid) (Figure I.5).

Figure I.5: Density of wood-based fiberboard elaborated by different processes

In the nonwoven process, wood fibers are mixed with textile fibers in order to reduce density while profiting the cohesion capacity of textile fibers during the consolidation procedure (Figure I.6). The consolidation is basically of a mechanical, chemical or thermal type. Depending on the nature of the textile fibers (monocomponent or bicomponent), liaisons between fibers endow the network with different properties. Insulation properties decrease in the case of

monocomponent fibers as liaisons may fill the pore network. The detail of this elaboration process will be discussed in the following paragraph.

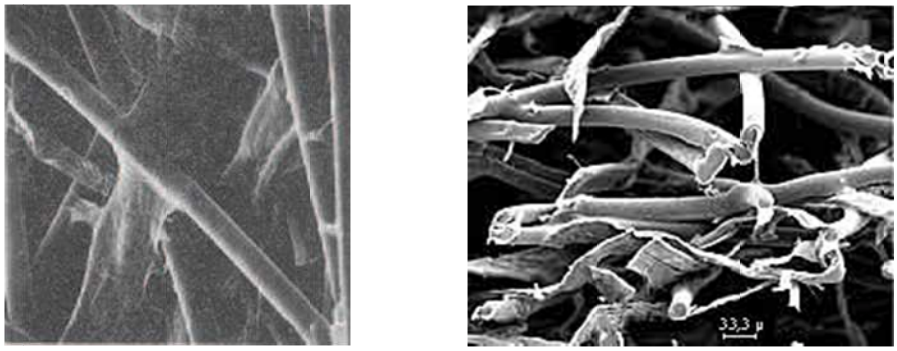

(a) (b)

Figure I.6: SEM image of fiber cohesion by thermofusion in case of (a) monocomponent fiber and (b) bicomponent fiber

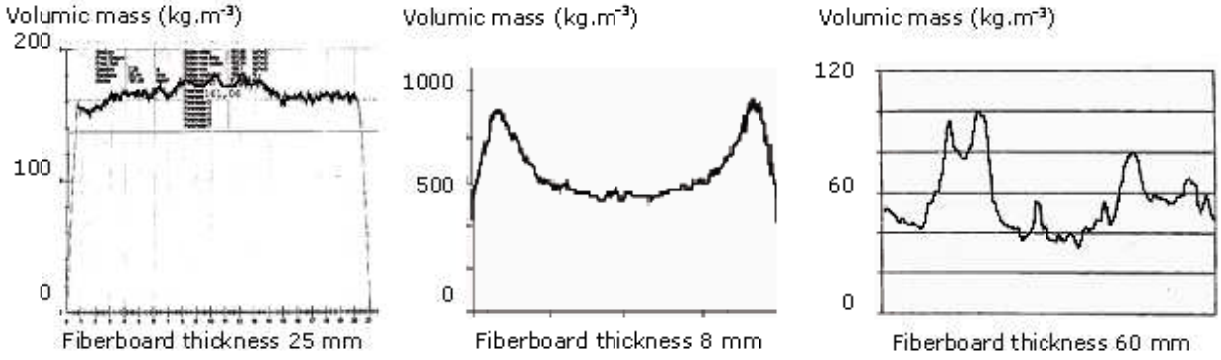

(a) (b) (c)

Figure I.7: Density profile of wood-based fiberboard in (a) wet process (b) dry process (c) nonwoven process

As wood-based fiberboards are increasingly commonly used, the interest of the mechanical behavior of these materials is increased. The need to optimize the material performances (thermal, acoustic, etc) requires a full understanding of every aspect of the material, especially its mechanical properties since all properties have a mutual influence. Compared to numerous studies that describe thermal and acoustic characteristics, only a few studies have been devoted to the mechanical characterization. The next section will give a literature review on the mechanical characterization of fibrous assembly.

I.2 Mechanical characterization of fibrous assembly

Wood-based fibrous materials, which are elaborated in the non-woven textile process, have a strong 3D structure and a strong variability of fiber characteristics relating to length, diameter, orientation etc. However, there is actually no mechanical model that specifically addresses the compressive behavior of this material. Therefore, the models that have been developed for random fiber networks may give some interests to solve the problems of this material.

It is well-known in the literature that the macroscopic behavior is mainly related to the nature, configuration, and architectural properties of the material. Materials are naturally inhomogeneous because it consists of dissimilar constituents or phases. These phases are distinguishable at certain scale. At the macroscopic scale, the material is normally considered to be homogenous on the whole specimen, which gives effective characteristics of the material or the characteristics that are based on the local characteristics of each dissimilar phase. However, there are many phenomena such as local fracture, stress localization that cannot be understandable from the point of view of average strain or stress. This thesis is only interested in mechanical modelling that incorporates most possibly the participation of the microstructure: the mechanical response of the material is deduced in function of the microstructure such as fiber volume fraction, fiber diameters, fiber orientations etc. That's why a brief description of the distribution law of the microstructure is necessary in the next paragraphs.

In this thesis, three mechanical characterizations are considered: the theoretical approach, the experimental approach and the approach based on imaging technique. The theoretical approach is established on certain assumptions linked to the nature of the microstructure to obtain macroscopic response of fibrous assemblies. The experimental approach gives macroscale stress-strain relation by fitting experimental data to some mathematical expressions and by obtaining empirically material constants. These expressions may be purely empirical or deduced from theoretical theory. Compared to the first two approaches, the approach based on imaging technique is the most recent mechanical characterization which allows us to get all local strains on the surface (2D) or inside the material (3D) based on the properties of structure pattern of the material. However, this method does not provide us with any information on the local stresses.

I.2.1 Theoretical approach of mechanical characterization

As mentioned above, the microstructure plays an important role in the mechanical behavior of the material, it is appropriate to give a brief literature review on the microstructure characteristics.

A common point of all fibrous assembly types is that all fiber properties (geometrical, physical, mechanical) respect a statistical nature [11] where distribution of properties such as fiber diameter, fiber length or fiber strength may be approximated by following normal distribution

$$f(x) = \frac{1}{\sigma.\sqrt{2\pi}} \exp\left(-\frac{\left(x - \overline{x}\right)^2}{2\sigma^2} \right) \tag{1.1}$$

where

x Random variable

$\overline{x}$ Mean value of x

σ Standard deviation of x

Fiber diameter distribution may be given by using a weighted-sum of normal distributions [12] while assuming the fiber section is circular:

$$f\left(d\right) = \sum_{i=1}^{n} \frac{\alpha_i}{\sigma_i \sqrt{2\pi}} e^{-\frac{\left(d-\overline{d_i}\right)^2}{2\sigma_i^2}} \tag{1.2}$$

with

n Number of components of function f

α_i Weight coefficient of component i

σ_i, d_i Standard deviation and mean diameter of component i

The same law may be found with pore size distribution for nonwoven fibrous materials in Jaganathan et al.'s study [13] as illustrated in Figure I.8.

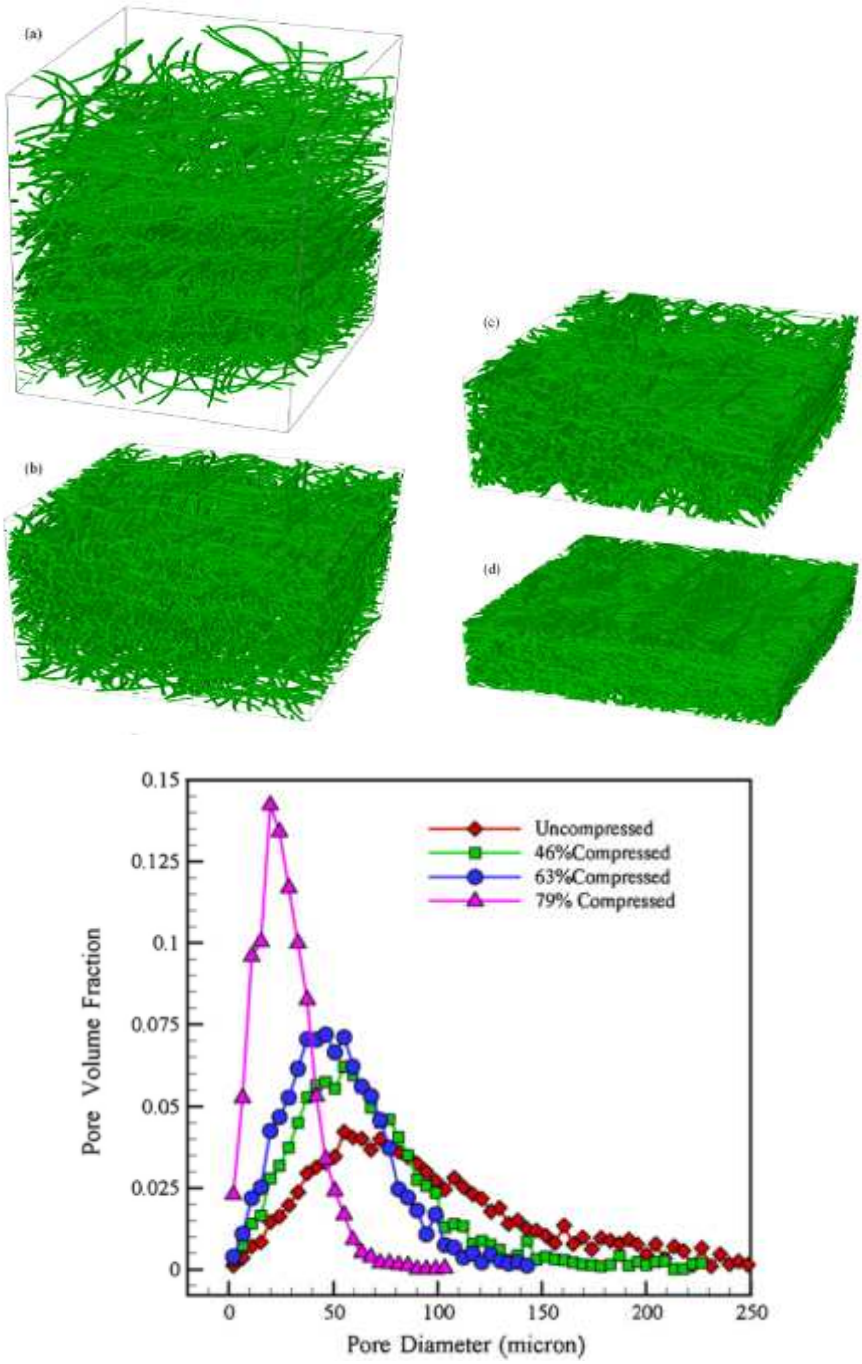

Figure I.8: Effect of compression on pore size distribution of fibrous structure [13]

However, the application of this distribution law to other properties demands some modifications to compensate the deviation from normal distribution [11]. Plus, the distribution law relating to similar properties of different material is not always the same, i.e. Peyrega [14] and Lux [15] found that the fiber diameters respect a gamma distribution instead of normal distribution in [11].

The theoretical approach can be considered as officially beginning with the study of Van-Wyk in 1946 and all later researches on the compressive behavior of textile assembly have aimed at improving Van Wyk's model, namely Komory and

Makishima [16], Komory and Itoh [17], Pan [18], Carnaby [19], Pan [20], Pawlak [21], Neckar [22], [23] etc. In Van Wyk's model, only bending deformation of individual fibers between fiber-fiber contact points is considered, the effect of slippage, extension, twisting and friction during compression is neglected. The number of contacts or the mean distance between contacts creates fiber elements of finite length inside the system which are considered as beams connected at two ends. Therefore only bending deformation is taken into account. Pawlak [21] applied this model to simulate the compressive response of paper structure. He allow for a factor to compensate for finite length in the overall stress expression which increases significantly as fiber length decreases. Recently, Rodney [24], Barbier [25], [26] employed discrete simulation, originated from molecular dynamics techniques for polymers, in order to characterize entangled fibrous networks by discretizising fibers in segments at cross-link points and thus 3 main deformation modes of fiber as traction, bending and buckling can be reproduced. Among theoretical approaches, some models incorporate the mechanics of continuous medium theories [27]. These continuum-based models employ homogenization methods to study the material response through energetic approaches, which demands knowledge of a representative element volume (REV) in which the stress, strain of the material is summed up over the whole REV. Three continuum-based models for compressed fibrous material may be named as: model based on the elongation of constituent fibers at the microscopic scale which is introduced by Narter et al. [28], model based on bending and torsion of fibers using the rate theory for granular solids developed by Alkhagen et al [27] and model based on fiber bending at microscale introduced by Neckar et al [22]. However, even though the heterogeneity of fibrous assemblies is introduced through statistical microstructures, continuum-based models have the tendency to blur the heterogeneity of the material which is the cause of local mechanical phenomena. As the influence of heterogeneity on material behavior is also a main subject of this thesis, however, these models seem complicated to be used for actual study, material continuum models will then not be employed in this thesis.

As the studied material is complex, the objective is firstly to validate Van Wyk's model while verifying with some other simplified models of mechanical response-structure at the macroscopic scale. Consequently, only the detail of Van Wyk's model is presented in this section.

In 1946, Van Wyk proposed the relation between applied pressure and fiber assembly characteristics as

$$p = \frac{KEm^3}{\rho^3}\left(\frac{1}{V^3} - \frac{1}{V_0^3}\right) \tag{1.3}$$

where

E Young's modulus

m mass of fiber assembly

ρ fiber density

K constant depending on fiber assembly properties

V_0, V respectively the sample volume at initial and deformed state corresponding to applied pressure p.

In this relation, Van Wyk assumed that:

- Fibers are all of constant length and diameter, randomly oriented and the mass of fibers is uniformly packed.

- Only bending deformation of individual fibers between fiber-fiber contact points is considered, the effect of slippage, extension, twisting and friction during compression being neglected.

The number of fiber contacts in a random network in a unit mass containing cylindrical fibers is estimated as

$$\overline{n_m} = \frac{8m}{\pi\rho^2 d^3 V} \tag{1.4}$$

and the average distance $\bar{b}$ between contacts is determined as

$$\bar{b} = \frac{2V}{\pi d L} \tag{1.5}$$

where d is the fiber diameter and L is the total length of fibers in the volume.

The fiber volume fraction is defined as

$$f_v = \frac{V_{fib}}{V} \tag{1.6}$$

so

$$f_v = \frac{f_{v0}}{1+\varepsilon} \tag{1.7}$$

where V_{fib} is the fiber volume, V is the volume of fiber assembly, f_{v0} is the fiber volume fraction at the initial state where no load is applied, $\varepsilon = h / h_0$ is the engineering strain.

Later Van Wyk corrected Eq. (1.3) by including the incompressible volume V' due to the formation of fiber contacts in some volumes that prevents these zones from receiving solicitation.

$$p = \frac{KEm^3}{\rho^3}\left(\frac{1}{(V - V')^3} - \frac{1}{(V_0 - V')^3}\right) \tag{1.8}$$

The limitation of the classical Van Wyk's model is that it may be employed for only straight and randomly oriented cylindrical fibers with a similar diameter and length. This model does not explain the residual deformation along with hysteresis during cyclic compression tests and it fails to account for different compression properties of different fiber types which have the same parameter in Eq. (1.3) [29], which is the basis for later studies.

Following Komori and Makishima [16], the probability of finding the fiber orientation in the infinitesimal angle range θ to $\theta + d\theta$ and φ to $\varphi + d\varphi$ (Figure I.9) is $\Phi(\theta,\varphi)\sin\theta d\varphi d\theta$ in which $\Phi(\theta,\varphi)$ is the fiber orientation distribution function which satisfies the normalization condition over the orientation space as

$$\int_0^{\pi}\int_0^{\pi}\Phi(\theta,\varphi)\sin\theta d\varphi d\theta = 1 \tag{1.9}$$

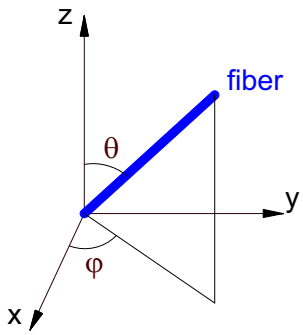

Figure I.9: Polar coordinates (θ,φ)

The probability ζ of fiber $A(\theta,\varphi)$ contacting fiber $B(\theta',\varphi')$ of length L_f and diameter d in the assembly of volume V is

$$\zeta = \frac{2dL_f^2}{V}\sin\chi \tag{1.10}$$

where

$$\cos\chi = \cos\theta\cos\theta' + \sin\theta\sin\theta'\cos(\varphi - \varphi') \tag{1.11}$$

The number of contacts per unit length of fiber

$$\bar{n} = \frac{2dL}{V}I \tag{1.12}$$

where L is the total fiber length within the volume V and

$$I = \int_0^{\pi} d\theta \int_0^{\pi} d\varphi \int_0^{\pi} d\theta' \int_0^{\pi} d\varphi' \sqrt{\left\{1 - \left[\cos\theta\cos\theta' + \sin\theta\sin\theta'\right]^2\right\}} \times \Phi(\theta,\varphi)\Phi(\theta',\varphi')\sin\theta\sin\theta' \tag{1.13}$$

However, this probability can only be correct for the first contact, which is pointed out by Pan [18] in 1993. Following Pan, when the first contact is created, it will occupy a certain fiber length and reduces the appearance probability of next contacts. The probability for the $(i+1)^{th}$ contact may be calculated as

$$\zeta_{i+1} = \frac{2dl_f^2 \sin\chi_i}{V}\left(1 - \frac{\left(\frac{d}{\sin\chi_1} + \frac{d}{\sin\chi_2} + \ldots + \frac{d}{\sin\chi_i}\right)}{l_f}\right) \tag{1.14}$$

Another approach used to determine contact number was proposed by Neckar [22] using Poisson process for the distribution of the number k of contacts on any arbitrary fiber with direction (θ,φ). In 1994, Komori and Itoh [17] made further improvement by introducing forbidden length and forbidden volume occupied by certain fibers in contacts which prevent the formation of other contacts on the same fibers. Consequently, this volume may absorb energy or be deformed during compression. This theory allowed Neckar [22] in 1997 to review Van Wyk's model by excluding this volume in the pressure-volume relation as

$$p = KEV^3\left(\frac{1}{(V - V_{ex})^3} - \frac{1}{(V_0 - V_{ex})^3}\right) \tag{1.15}$$

or in terms of fiber volume fraction [22] as

$$p = KE\left(\frac{f_v^3}{\left(1-\frac{f_v}{f_{vm}}\right)^3} - \frac{f_{v0}^3}{\left(1-\frac{f_{v0}}{f_{vm}}\right)^3}\right) \tag{1.16}$$

where f_{vm} is the maximum fiber volume fraction when all pores are squeezed out of the fiber network.

I.2.2 Experimental approaches of mechanical characterization

Parallel to analytical approaches, some authors have tried to understand the compressibility of the fibrous material through empirical methods where they establish the relationship between the applied stress and the sample thickness. These relations fit well for their own material and experimental methods. Normally such approaches are easily applied, yet it does not account for change in the microstructure of the materials, except for the fiber volume fraction. Figure I.10 shows a study on the compression behavior of many fibrous mats done by Poquillon [30]. Each material has its own response but the responses of different fibrous assemblies show the same tendency: the material exhibits a non-linear behavior with hysteresis and residual deformation

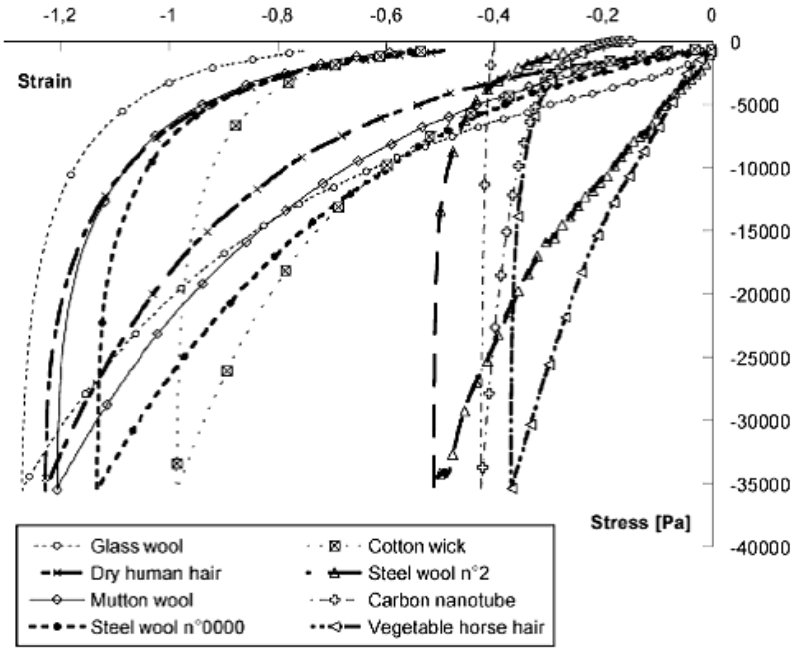

Figure I.10: Compressive behavior of different fibrous mats in cyclic compression test [30]

The most popular experimental formula must be Van Wyk's for fibrous mat in compression without taking into account either friction or the fact that this mat is created by different populations of fibers in which stress is related to global strain following an exponential law as

$$\sigma = a\exp\left(\varepsilon_{tr} b\right) \tag{1.17}$$

where *a, b* are negative constants, depending on own properties of each material. The exponent is a function of the fiber configuration and *b* is found around -3. σ, ε_{tr} are respectively the stress and the true strain defined as

$$\varepsilon_{tr} = \ln\left(\frac{h}{h_0}\right) \leq 0 \tag{1.18}$$

and

$$\sigma = \frac{F}{A} \tag{1.19}$$

where h, h_0 are the initial and deformed thickness, A is the surface area and F is the applied load on the sample.

In fact, Eq. (1.16) is derived from the other theoretical expression of Van Wyk (Figure I.11) as

$$p = KE\left(f_v^3 - f_{v0}^3\right) \tag{1.20}$$

Where f_v and f_{v0} are fiber volume fraction at initial and deformed state.

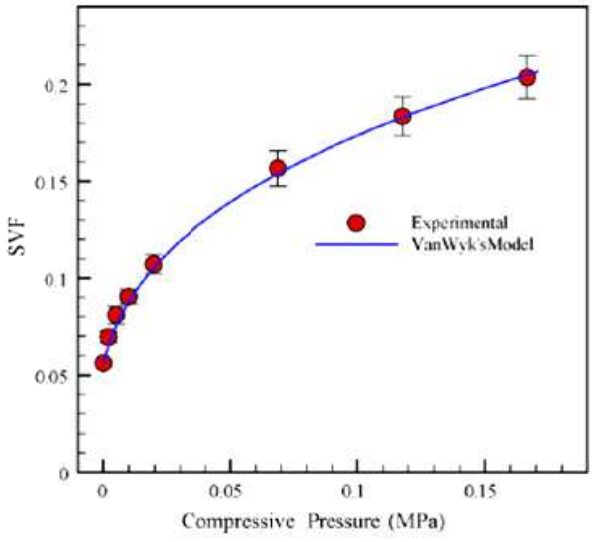

Figure I.11: Theoretical Van Wyk's model fitted to experimental data [31] following Eq. (1.20). SVF stands for solid volume fraction.

Toll [31] shows a general exponent power law of n for variety of tangled fiber assemblies where he indicated n=3 for 3D orientation (in agreement with Van Wyk's model for 3D) and n=5 for 2D orientation and higher exponents for unidirectional systems.

Also, basing on Van Wyk's model, Durville [32] modifies Eq. (1.19) to better fit the behavior of his materials, where he adds the relative variation of the volume fraction f_v/f_{v0} in its relation to vertical load F following the relation below

$$F \propto \left(\frac{f_v - f_{v0}}{f_{v0}} \right)^{-\frac{3}{2}} \tag{1.21}$$

He found it fits well with his materials until 85% of compression state.

Baudequin et al. [33], from their analytical and experimental data, derive the expression of applied force in function of the compressive strain as

$$F \propto \left(\varepsilon^* - \varepsilon\right)^{-\frac{3}{2}}, \quad \varepsilon^* > 0, \varepsilon > 0 \tag{1.22}$$

with $\varepsilon = h/h_0$ (h, h_0 are respectively the deformed and initial thickness of the material under compression) and ε^* is the maximum compression strain. In his study, Baudequin estimates $\varepsilon^* \approx 0.96$. For fibrous materials, if the deformation only happens in the pores, ε^* may be considered equal to the total porosity of the assembly. However, there exists several closed pores that cannot be compressed. Consequently, ε^* is normally smaller than the total porosity and should be experimentally determined.

Hysteresis is observed in cyclic compression tests for almost all fibrous assemblies, which is due to the loss energy in assembly during the slippage between fibers, or so-called friction between fibers and the irreversible rearrangement of fibers [30]. Normally, fibrous materials show hysteresis with residual deformation (Figure I.10).

I.2.3 Strain fields based on image correlation

The main technique used to obtain the displacement and strain field is based on the principle of image correlation named Digital Image Correlation (DIC) in two dimensions and Volume Image Correlation (DVC) in three dimensions. Both DIC and DVC are full field and non-contact strain measuring methods, having the same principle and the same features. They demand the presence of a pattern on the

surface or random texture (Figure I.12) for DIC and a random pattern in the grey level in the microstructure in case of DVC (Figure I.13). As these techniques are similar, DIC is only briefly presented. Image correlation consists in finding, in the deformed image, a small domain of pixels that is the most similar to the chosen domain in the reference image (Figure I.12). They are all carried out in 3 steps [34]:

- Acquisition of digital images by using CCD cameras.

- Determination of mark displacement by comparing two successive images, one of which is called "reference image" and the other called "deformed image".

- Numerical calculations of deformations by some image treatment softwares.

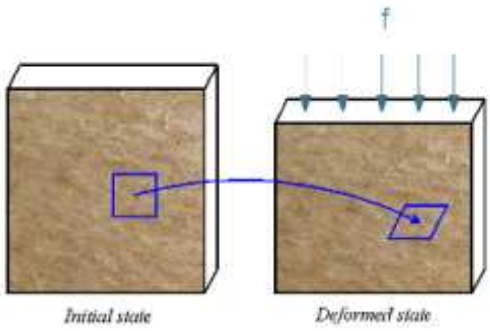

(a)

Figure I.12 : 2D image correlation (DIC)

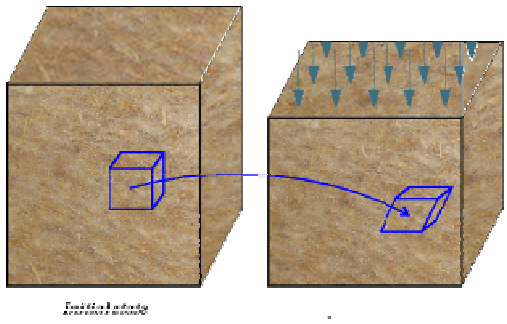

Figure I.13 : Digital volume correlation (DVC)

Most materials are very complex and so strongly heterogeneous that surface characterization alone is not sufficient [35]. For example, the overall failure of the material starts with a micro-crack inside the material which cannot be detected with DIC. But DVC should not be mistaken for 3D surface deformation that relies on two-angle planar images, i.e. stereovision [36], [37], it is a full 3D tool that allows us to determine the strain field inside the material. This technique was first proposed by Bay in 1999 [38], as an extension of 2D image correlation to measure strain field

in trabecular bone tissue under compression. The strain field is obtained by minimizing the correlation coefficient of a sub-volume centered at considered point in undeformed and deformed image data. The minimisation reaches next the subvoxel scale by using the Levenberg-Marquardt variation of the Gauss-Newton technique. The strain field is calculated from the displacement fields by gradient estimation techniques. However, as the author himself recognised, this approach is more sensible to the overall background intensity between two studied images since he tries only to minimize the correlation coefficient and it does not account for the rotation of the sample since he only uses three translation degrees of freedom. But later on, with his colleagues, he improved the correlation accuracy by adding rotation degree of freedom in minimization [39]. Verhulp et al [40], Germaneau [41] extend DVC to twelve degrees of freedom to attain a full linear transformation, including three degrees of translation and nine components of transformation gradient tensor. DVC has been a powerful tool for strain analysis of complex materials such as bone [38], [39], [42], rock [43], synthetic foam [44], wood [35], etc. Recently, DVC has been also employed on fibrous materials [45], [46]. Compared to rigid material like polymer foam and wood specimen, fibrous materials may be considered as soft and flexible materials. Three principal aspects make it more difficult to use DVC in the case of the fibrous materials than other materials. Firstly, fibrous materials are strongly porous (i.e. more than 95% for wood-based fiberboard) so that there are maybe a few of 3D grid point system of DVC and its subvolume may be found in the space in two consecutive deformation states if the size of subvolume is not large enough. We still obtain strain for these zones where should not have any deformation. Secondly, during the solicitation, the configuration of fibrous assembly changes significantly, so different undeformed zones. At the initial state may give the same deformed configuration, consequently generating false displacement and false strain. Plus, the deformation of the material is a multi-mechanism deformation: compression, tension, bending, torsion etc., which demands a higher degree of rigid body motion combined with homogeneous deformation. The solution containing higher degrees costs a lot of time and efforts to obtain. In this study, for simplification, only the first order is taken into account. However, the influence of heterogeneity of local strain on the minimisation procedure is limited by performing the correlation technique on consecutive compression steps with a small strain increment.

For DIC or DVC methods, in order to obtain an accurate strain-field, two aspects must be carefully considered: one is the accuracy of measurement obtained

through the intensity minimisation procedure of correlation domains and the other is the size of the correlation domain [18]: a small size of correlation window may not provide sufficient solid phase information (or contain only pore phase), but a large domain size will lead to inaccuracy since it is linked to the heterogeneity of the material transformation and cost computation time of measurement. For DVC, the correlation window or the correlation domain is the other term for subvolume centered at the grid point that helps us to find the displacement of grid points. The computational time depends strongly in the choice of correlation domain size, i.e. for network having a quasi-homogeneous material transformation, the larger the domain is, the more accurate the displacement determination is but the longer the time is to compute. Furthermore, this larger size costs a lot of system memory.

The development of Digital Volume Correlation (DVC), coupled with X-ray microtomography has enabled the 3D full field strain analysis inside the material during solicitations [38], [39], [40], [47]. However, the existence of defects in CT-images influences not only on the morphological study but also measurement accuracy for DVC [47], [48], [49].

I.3 Microstructural characterization and observation of the fibrous materials

Fibrous materials are naturally heterogeneous and consist of dissimilar constituents (or “phases") that can be visibly distinguishable. However the heterogeneity of the fibrous materials can be evaluated at different scales: (i) configuration of different phases, distribution of fiber contacts, distribution of fiber diameter and pore position when considering the whole structure (ii) the variability of length, diameter, curvature in different segments of each individual fiber, not to mention the heterogeneity of fiber wall constitution when we go to smaller scale etc. This heterogeneity cannot be seen with a naked eye. As the role of structure on smaller scales is well known by all researchers, it is necessary to employ adequate observation methods which allow us to observe and then exploit the characteristics of the microstructure. For fibrous materials, all recent observation methods are based on imaging techniques such as optical microscopy, scanning electron microscopy (SEM) and X-ray computed microtomography, which allows us to investigate material characteristics at different scales, from less than 1µm to several millimeters. Each technique has its own advantages and limitations, that’s why we will now discuss each of the three techniques in the short following section.

I.3.1 Optical microscopy

Optical microscopy is a 2D imaging technique which uses visible light and a system of lenses to observe small objects. Optical microscopy involves the diffraction, reflection or refraction of electromagnetic radiation/electron beams interacting with the specimen in order to create an image. The limitation of diffraction can be surpassed by other techniques using other kinds of wave (SEM, X-ray microtomography). Nowadays, by adding more adequate equipment to the basic optical microscopy, we can extract more data of the material instead of only observation (Confocal microscopy, Microspectroscopy, Ultraviolet microscopy…). Among these techniques, confocal microscopy enables the reconstruction of 3D structures from 2D images acquired along the thickness of the material, this thickness being limited. Delisée et al. [50] used CLSM (Confocal laser scanning microscopes) to observe and characterize wood based laboratory MDF fiberboards. 3D information such as size of the pores, size of the fibers, contact numbers was extracted from 2D images of the projection of the maxima using mathematical morphology (Figure I.14) and Poisson process. CLSM was used also in Batchelor and al. [51] to determine the number of fiber contacts and the fractional contacts area of paper sheet following Poisson probability. They found a good agreement between experimental data and the analytical model. However, these techniques are then limited by long acquisition time and the capacity to observe further from the sample surface [10] (about 200µm of depth). Consequently, optical microscopy is not used in this thesis.

(a) (b) (c)

Figure I.14: Simulation procedure of MDF sample (a) greyscale image (b) binary image (c) simulated image [50]

I.3.2 Environmental scanning electron microscopy (SEM)

Environmental scanning electron microscopy is essentially a two-dimensional imaging technique used in a wide variety of applications: biology, medicine, industry, paper characterization etc. SEM uses electron beam and electromagnetic lenses to focus and direct the beam on the small spot of several manometers on specimen surface. Thanks to its properties, SEM may be used to quantify the surface and cross section of fibrous assembly, which allows to determine the topography of fiber surface (orientation, anisotropy…) [52], the fiber wall thickness distribution and the evolution of fiber cross-section during some process [53], [54]. Moreover SEM gives necessary quantitative and qualitative information on the fibrous networks, which helps us to define both pixel resolution and size of the sample for further microtomographic tests. Tomczak and al. [55] used SEM to characterize morphologically the coir fibers under undamaged and fracture conditions during tensile tests. It allows them to detect some surface defects and to observe the evolution of fracture evolution of fibers. Aronsson [56] developed a method to characterize individual wood fibers in a three-dimensional image. This 3D image is reconstructed from a sequence of 2D images obtained through the combination of microtomography and SEM. SEM or optical technique lately was combined with digital image correlation in order to study the strain and displacement on the surface of heterogeneous materials [32],[57],[58] but not yet on fibrous materials. Figure I.15 presents SEM images of longitudinal section of Wood/PES fiberboard given by ISOROY, giving quantitative and qualitative information on the entangled structure and the size of pores or fibers.

Figure I.15 : SEM images of Wood/PES fiberboard - longitudinal section of 2700x2700μm^2 [10]

The biggest limitation of SEM for fibrous studies is its poor energy resolution and sensitivity to elements present in low abundances compared to the X-ray

microtomography that will be presented in the next section. A good energy is demanded to pass through fibers in order to have enough contrast between phases and to insure a sufficient sample size for analysis. Thereby, the SEM is also not used in this thesis.

I.3.3 X-ray microtomography

X-ray microtomography is a non-destructive imaging technique which allows us to characterize tridimentionally the interior of the materials up to a spatial resolution inferior to 1μm. Although there are many X-ray microtomography setups, the basic principles of this technique stay the same [49]. A X-ray beam, conic or parallel, is transmitted through the sample at different angular positions (Figure I.16). The X-ray intensity attenuation, which gives X-ray absorption at each particle, is recorded for each angular position through a CCD camera. Giving different X-ray absorption capacity, different phases of the material can be distinguished and reconstructed by filtered back-projection algorithm [49], [59]. We obtain then the reconstructed structure of the material inside tomographic images (Figure I.16).

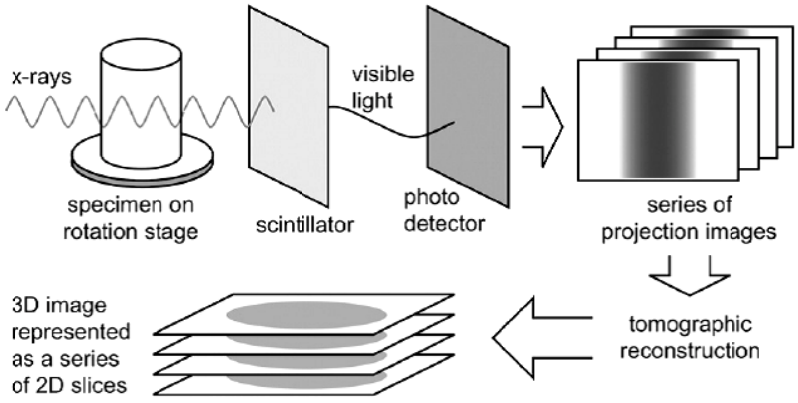

Figure I.16 : X-ray microtomography principle [53]

The appearance and development of X-ray microtomography allows us to access to real microstructure of the material: from tomographic images (Figure I.17), we are able to extract fiber orientation, fiber diameter, the distance between fibers, etc (Figure I.18). These properties are obtained thanks to mathematical morphology [60] [61] and supporting softwares such as Aphelion™ [62], ImageJ [63], AVIZO [64].

Figure I.17: Longitudinal slice of a microtomographic images of size 400x400pixels (1,9x1,9mm^2) at resolution of 4,91µm/pixel. ID 19 beam Line, ESRF Grenoble [65]

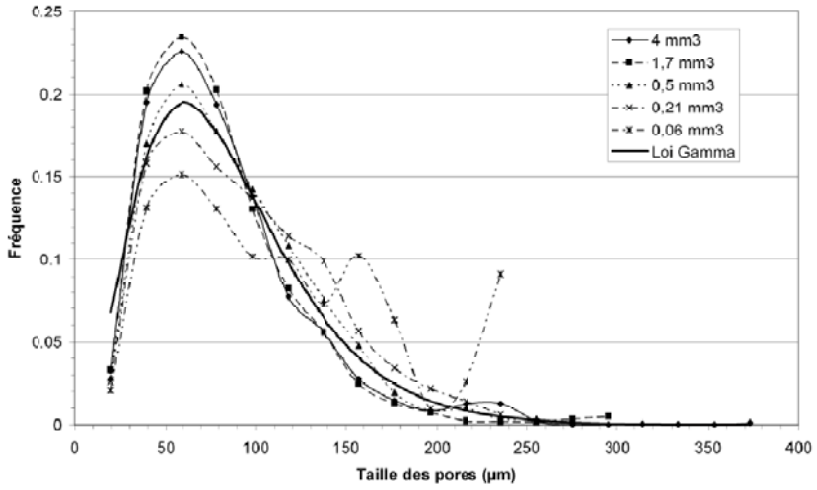

(b)

Figure I.18: Distribution of pore size at different analyzed volume [65]

Consequently, X-ray microtomography is found itself in a lot of applications: establishing relation between mechanical properties and the structure [31], [66], [67], determination of influence of the microstructure on thermal conductivity [31], [58], [68] or acoustic properties [69], [70].

Chapter II: Studied material - Wood-based fiberboard: Properties and Elaboration process

II.1 Wood-based fiberboard

The wood-based fiberboard is a prototype elaborated with framework of an industrial project (Agence de l'Environnement et de la Maîtrise de l'Energie), in collaboration between Isoroy society, LRBB (Laboratoire de Rhéologie du Bois de Bordeaux, I2M), TREFLE (Transferts Ecoulements Fluides Energétique, I2M) and IFTH (Institut Français du Textile et de l'Habillement) [71]. Containing about 77,5% of maritime pine fibers and 22,5% thermofusible textile fibers (mass fraction), the material is dedicated for thermal insulator of buildings, showing a thermal conductivity around 0.045W/mK. Obtained from nonwoven textile process, the studied fiberboard possesses a real 3D structure, strongly porous, with a very low density (about 45kg.m^3) (Figure II.1) but a good cohesion between fibers, allowing a thickness up to 65mm (Figure II.2).

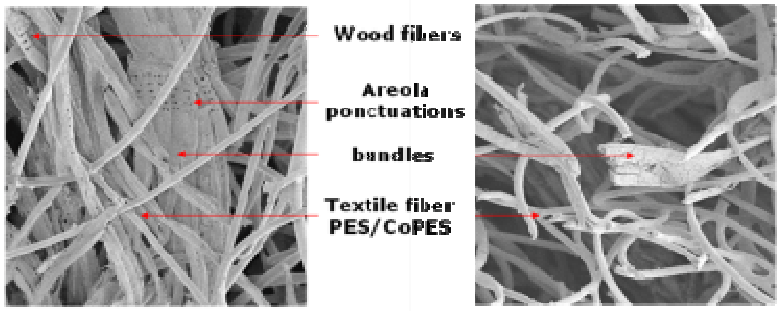

Figure II.1: SEM image of fiberboard Wood/PES (940µm) in (a) longitudinal section (b) transversal section

Figure II.2: Wood/PES fiberboard (100x100x65mm)

The aerodynamic procedure and the thermobonding, which are applied in order to fabricate the wood/thermoplastic fiberboard in this study, is an adaptation of dry nonwoven textile process. During the thermal bonding process, as polyester (PES) fibers are of bicomponent type, the sheath of fibers is melt in order to create the bonding contacts between fibers (Figure II.3) and reduce the board thickness. Its low melting temperature allows us to decrease the temperature in bonding

process and retain the fiber rigidity at the same time, which ensures the high porosity ratio and insulation properties of the studied material.

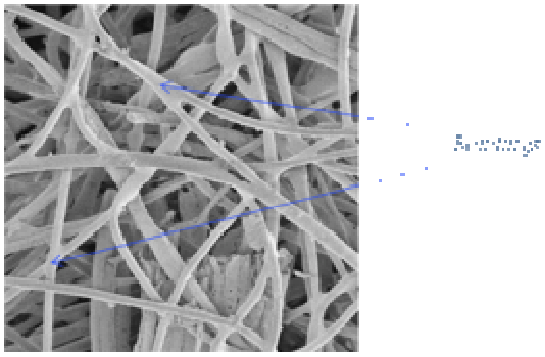

Figure II.3 : Fiber bondings

The fabrication of the material is carried out through two principal steps. The first step consists in pre-web formatting following the aerodynamic procedure where the pre-web is fed via a feed table and a feed roll to a fast rotating cylinder. Fibers taken-off from the cylinder are supported by a blowing air stream so that the fibers are oriented in all directions (Figure II.4). The second step is to web-bonding by a thermal process, thanks to the fusion of textile fibers.

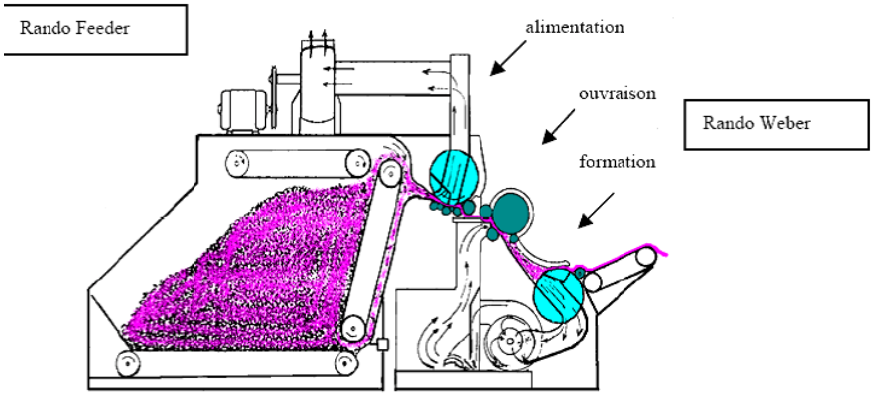

Figure II.4: Aerodynamic procedure

Because of the consolidation process which employed a pressing process to obtain the desired thickness, the fibers (wood, PES) show a privileged orientation perpendicular to the sample thickness [72].

II.2 Elementary fibers for elaboration process

II.2.1 Wood fibers and properties

Wood fibers are presented under the form of individual fibers or bundles (Figure II.2) of strong variability of length and diameter. Following [71], Fiber less than 7mm length occupies about 40% in mass of wood fiber population. These

fibers have a mean width of 32µm with standard deviation of 14µm and mean length of 0,6mm with standard deviation of 0,3mm. The bundles are longer than 7mm with mean width of 580µm and standard deviation of 134µm; having a mean length of 11mm with standard deviation of 7,5mm [71]. Figure II.5 shows the diameter variation of a wood fiber population and of the fibers that are eliminated during the elaboration process by aspiration.

The input parameters of wood fibers for the elaboration process are:

- Species: Maritime pine

- Method of defibration: thermo-mechanical defibration of 30g wood chips with 1liter of water under 160°C and saturated vapour of 6bars.

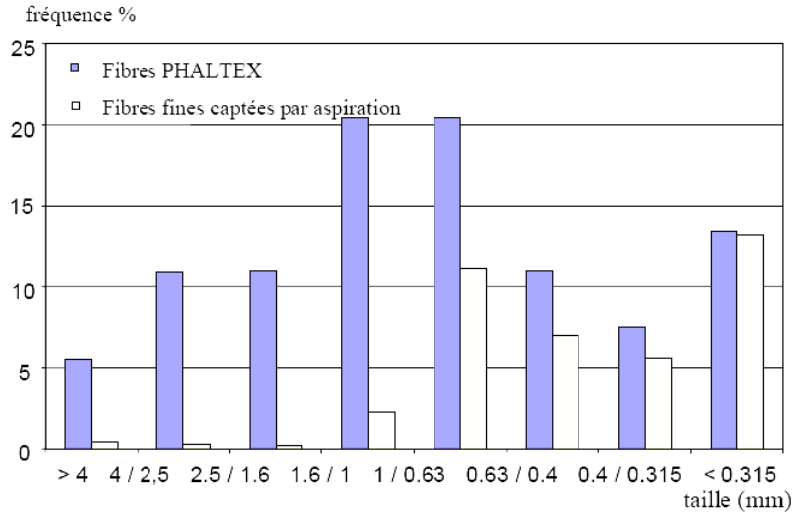

Figure II.5: Granulometry of wood fibers and eliminated wood fibers during the elaboration process [71]

II.2.2 PES fibers and properties

The thermoplastic fibers used for studied material are bicomponent fibers which are made by mixing polyester as the core and coPolyester as the sheath of the fiber; we will call it PES fibers for short. This combination allows us to exploit the best properties of each polymer component. PES is a thermoplastic polymer resin of the polyester family which is recyclable. CoPES is obtained by modifying polyester's molecular formulation. However, coPES has a much lower melt temperature than that of PES [73].

The input parameters of textile fibers for the elaboration process are:

- Fibers WELLBOND M1440 given by WELLMAN society, bicomponent core/sheath of PES/coPES respectively

- Titer: 4.8 dtex or 4.8g/10km

- Fiber length: 55mm

- Mean diameter: 20µm

- Fusion temperature of the sheath (CoPES) : 110°C

A study on the variation of tensile strength and diameter of PES fibers before the elaboration process is carried out at IFTH, on a population of thirty PES individual fibers. The objective of the study is to obtain the real properties of textile fibers and to compare these properties to given properties.

Diameter of thirty individual PES fibers is deduced from its linear mass density, the mass per unit of length or so-called single fiber's titer in tex (g/km), obtained by causing the fiber to oscillate transversely under the couple of ultrasound and low-tension halogen. The fiber titer is derived from the resonance frequency thanks to a vibroscop (LENZING SA) (Figure II.6) in respecting NF EN ISO 1973 standard, with accuracy up to ±1%. The fiber diameter d in μm is determined as expressed by the following relation

$$d = 200\sqrt{\frac{\rho_f}{10\pi\rho_{textile}}} \qquad (2.1)$$

where $\rho_{textile}$ represents the material density in g/cm^3, i.e. $\rho_{textile} = 1.38 g/cm^3$ and ρ_f is the linear density of textile fiber.

Figure II.6 : Vibroscope LENZING

Table II.1 : Textile diameters obtained by Vibroscope LENZING

Specimen	Tex	Diameter (µm)	Specimen	Tex	Diameter (µm)	Specimen	Tex	Diameter (µm)
1	0.428	19.87	11	0.445	20.26	21	0.491	21.28
2	0.414	19.54	12	0.576	23.05	22	0.58	23.13
3	0.61	23.72	13	0.566	22.85	23	0.426	19.83
4	0.442	20.19	14	0.545	22.42	24	0.527	22.05
5	0.442	20.19	15	0.401	19.23	25	0.64	24.30
6	0.442	20.19	16	0.41	19.45	26	0.708	25.56
7	0.44	20.15	17	0.463	20.67	27	0.54	22.32
8	0.645	24.39	18	0.452	20.42	28	0.374	18.58
9	0.552	22.57	19	0.505	21.59	29	0.515	21.80
10	0.54	22.32	20	0.445	20.26	30	0.329	17.42

The textile diameters (Table II.1) are found between 17.4µm and 25.6µm with an average of 21.4µm and a standard deviation of ±1.8µm (Figure II.7).

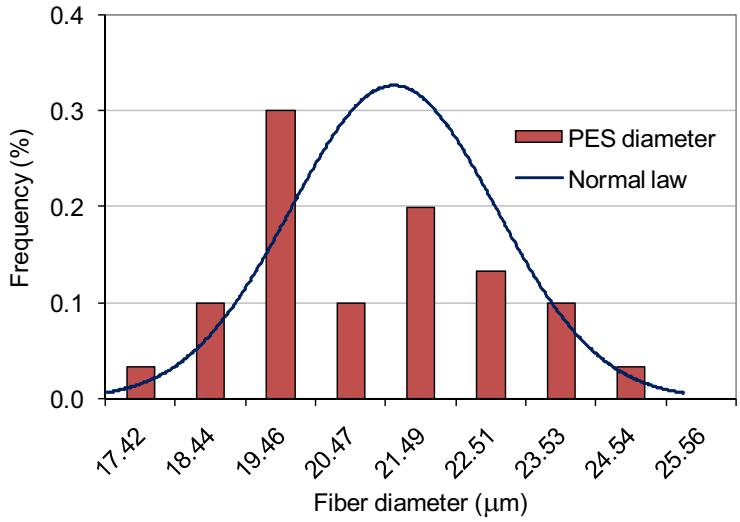

Figure II.7 : Histogram of textile fiber diameters

Then thirty textile fibers WELLBOND M1440 (WELLMAN) are tested in tension until failure, using a mono-column dynamometer (Hounsfield, Figure II.8), in accordance with EN ISO 5079 (Textile fibers - Determination of breaking force

and elongation at break of individual fibers) at the strain rate 20mm/min. The load was recorded by a transducer with a 5N-capacity cell. All fibers, whose tested length is of 20mm, are pre-tensioned at 0,04N. The tests allow us to determine the tensile strength of textile fibers (Figure II.9). These tests are carried out at IFTH (Institut Français du Textile et de l'Habillement de Lyon).

Figure II.8 : Tensile test by mono-column dynamometer (Dynanomètre mono-colonne)

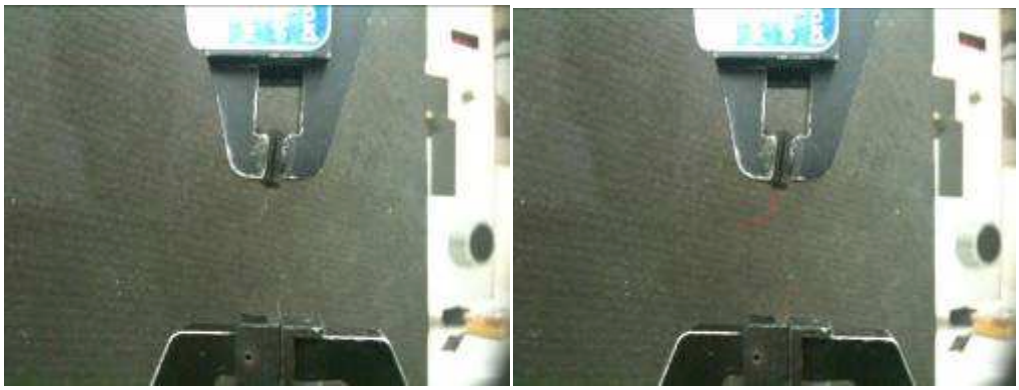

Figure II.9 : Textile fiber at failure state

A graphical representation of stress-strain curves of tensile tests on thirty textile monofibers is shown in Figure II.10 in which the engineering strain is used. These curves follow different paths but they have two common trends: first, the behavior of all fibers is rather ductile containing two zones, the first zone is elastic and is the same for all fibers and found until 7 to 8% of tension. After this threshold value, the fibers are hardened in the second zone and can attain its limit elongation of more than 30% (some fibers attains 40-50%). The next common tend is that fibers have a similar Young's modulus which is found at about 2000MPa for the first linear path, and around 400MPa for the second linear path.

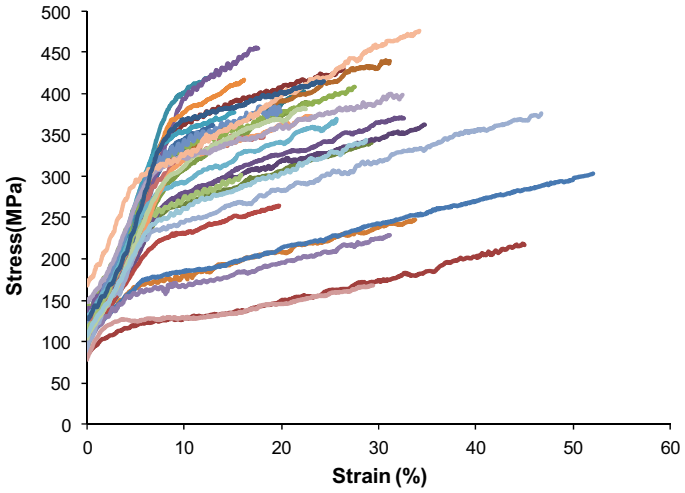

Figure II.10 : Stress-strain curves of mono textile filaments

However, each fiber exhibits its own behavior due to its different section constitution since used textile fibers own bicomponent section. We do not have any study on the initial textile section, i.e. the position of the core in comparison to the sheath, the mass ratio between these two layers etc., and also the changes in textile section after the consolidation process. Consequently, the quantitative analysis of textile fibers before consolidation is strictly for reference.

II.3 Conclusion

In chapter I and II, we have presented the studied material with its characteristics as well as mechanical characterization approaches in the literature employed for fibrous materials. In order to study mechanical properties of the material in the whole, we propose the corresponding methodology: (i) determination of stress-strain response at the macroscopic scale; (ii) analysis of the strain field by image correlation methods (DIC, DVC) at the mesoscopic and the microscopic scale; (iii) extraction of morphological parameters of the microstructure thanks to X-ray microtomography supported by the mathematical morphology.

The need of determining the mechanical characteristics of such a fibrous material is increased, since it is recently among the most numerous, diverse and developed products. However, characterizing the behaviour of the fibrous material is always a challenge due to some specific difficulties. The first difficulty relates to the complex microstructure of fibrous assemblies: mechanical modeling still addresses only some kinds of fiber population containing fibers of constant geometrical properties. Some researchers start to address the problem of fiber

populations which contain more variable fibers but their mechanical theories are always based on some simplified assumptions on the microstructure [16], [19], [74], etc. The properties of the real microstructure properties are now achievable thanks to X-ray microtomography, the technique allows us to observe the evolution of the microstructure undergoing solicitations. The second difficulty concerns the mechanical characterization at the small scale which cannot be performed with classical models. We show that DVC is a powerful tool which allows us to investigate the evolution of local strains at the scale of several micrometers.

Indeed, the studies at different scales are required, since the characteristics at each scale play an important role and help us to understand what happens with other scales. Plus, the coupling of local strains and of microstructure allows us to explain the deformation mechanisms that govern the whole behavior of the material.

In the next chapter, we put into practice an experimental methodology which will give us the data on the mechanical response of the material, as well as tools for microstructure exploitation.

Chapter III: Mechanical tests and Measurement methods of strain field on wood-based fibrous materials

III.1 Description, methodology, protocol of compression tests

Determining mechanical characteristics of the fibrous materials at different scales is far from simple because of its complex structure and deformation mechanisms. Samples are extracted from wood-based fiberboards as described in section III.2 and tested at two different sizes (Figure III.1): the larger ones are parallelepipeds around 100x100x65mm, according to the European norm NF EN 826 [75], the smaller ones are cylinders of about 9mm diameter and 9-11mm height where sample size depends on the chosen pixel resolution and the X-ray machine capacity.

A brief description of compression tests is illustrated in Figure III.1 and Table III.1.

Large samples are uniaxially compressed with or without confinement, under or not under CCD cameras. The first tests that we carry out are compression tests until maximum consolidation, which gives us global behavior at the macroscopic scale. Regarding the real working condition of the sample which is compressed while being confined by the surrounding material, some samples are confined during the test. However, the confinement creates friction between the samples and the confinement device, which may influence the compression behavior, especially the contact zone. We try to limit as much as possible this friction by means of an anti-friction film pasted on the confinement device. Other tests at this sample size also consist of cyclic tests at different compression states where we observe well a non-linear behavior with a residual deformation and hysteresis. These tests have for objective to measure the elastic limit, and also to evaluate the friction between the sample laterals and confinement device. Consequently, CCD cameras are employed where the surfacic strain of the sample is observed and computed thanks to the mark tracking method and to the digital image correlation (DIC).

An experimental set-up is built for smaller samples. A sample is compressed at different compression states under cone-beam X-ray microtomography (CT-test for short), which is next object for the study of the 3D strain field inside the material. Tests at the same sample size are added in order to validate the representativity of the sample in the CT-test and to establish the multi-scale behavior. The common difficulties for all tests are preparation of the samples, determining initial test conditions (initial load, initial sample thickness etc.) and exploiting the experimental data.

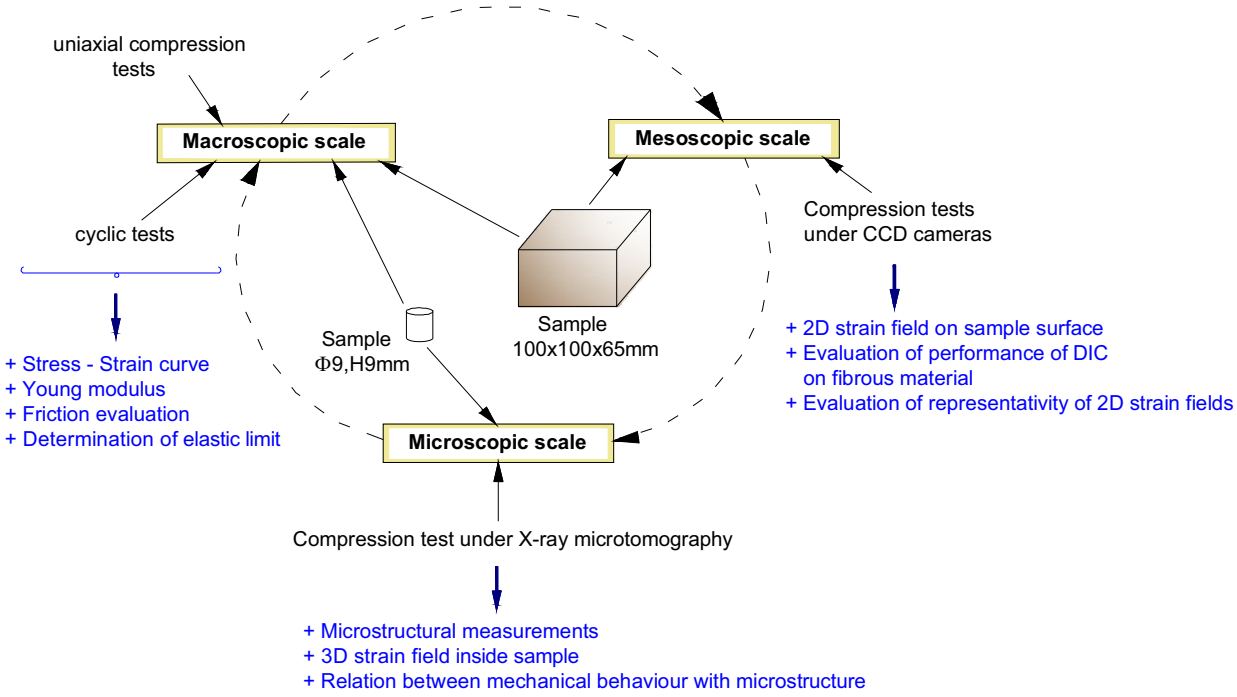

Figure III.1: Description of compression tests at different scales

Table III.1: Summary of number and sample size in different compression tests

N°	Type of test	Sample size	Number of samples
I01 – I05	Classical test (Large samples)	~100x100x65mm	05
IC01-IC12	Classical test (Small samples)	Φ9mm, H9mm	12
P01-P02	Test under CCD cameras	~100x100x65mm	02
	X-ray microtomography test	Φ9mm, H9-10mm	02

III.2 Sample preparation

The sample preparation is complicated, coming firstly from the physical properties of the material: complex, porous and easily deformed under external mechanical solicitations. The PES fibers, even though its role is to create bondings inside the material, are quite hard to be cut through. A long and not enough strong cut causes only destruction of the sample by drawing a part of the material off on sample surface. However, a short and strong cut may give danger for operators. Consequently, the sample preparation must be carried out with much caution.

Large samples are extracted from parts of laboratory panels elaborated in the framework of the ISOROY Project [71] into required dimensions 100x100x65mm,

90x90x65mm and 100x80x65mm (Figure III.2). There is no pre-treatment for samples such as conditioning or prestressing.

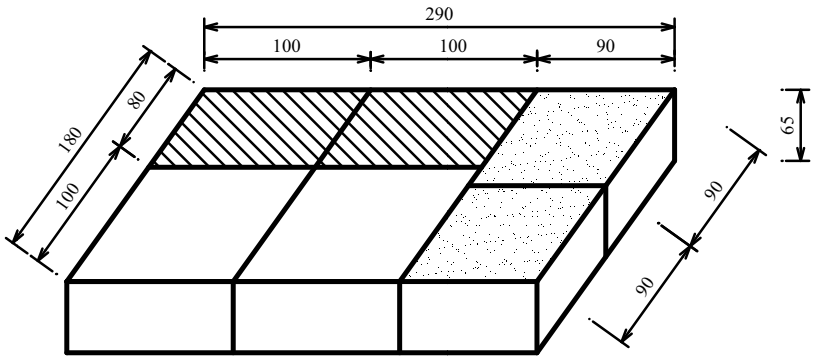

Figure III.2 : Extracted samples

Small cylindrical samples are extracted through a rotary die cutting (Figure III.3c) with an exact diameter of 9mm and thickness around 9mm obtained from slices of about 100x100x9mm (Figure III.3b). Not as large samples, small specimens are quite influenced by cutting method, including the chosen size and the cutting machine. In order to get the desired thickness of slices, solid wood pieces are measured and cut to validate the shearer (Figure III.3a).

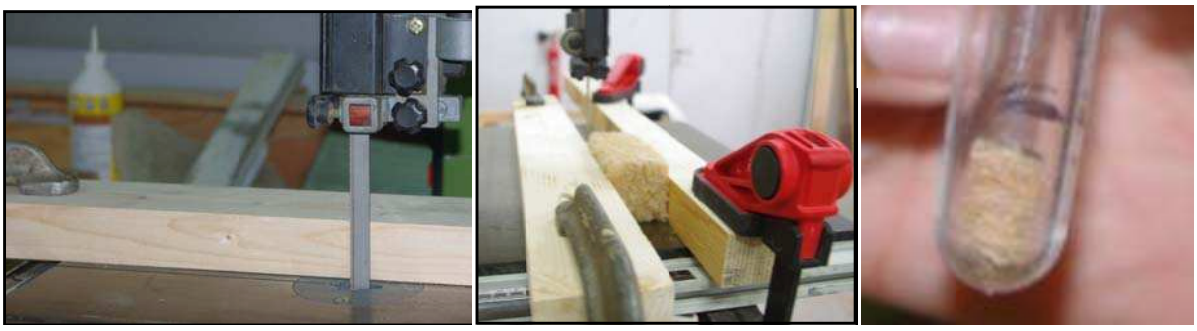

(a) (b) (c)

Figure III.3: (a) Validation of shearer (b) Slice cutting (c) Small sample [75]

However, we cannot obtain the same thickness on fibrous wood slices compared to plain wood because of cutting difficulty mentioned above. This thickness varies from slice to slice around the desired size, and it is difficult to decide whether it is the real slice thickness or the thickness modified when passing the sample through the shearer. The phenomenon is clearer for small cylindrical samples: it rebounds as soon as being pulled out of die cutting while losing some materials at the sample surface. Several solutions are considered to choose adequate initial conditions. A quantitative analysis of the sample (height, thickness, mass, etc.) [76] will allow us better understanding the behavior of the material.

III.3 Compression tests

III.3.1 Compression tests on large samples (~100x100x65mm)

a) Compression tests without CCD cameras

The used compression machine at the I2M laboratory is a MTS testing machine, in which the applied load is recorded by a load transducer with a 100kg capacity load cell, and the displacement is measured by using a displacement transducer. The displacement transducer is placed on the moving plate because of some technical difficulties.

Five samples are tested at the same strain rate of 3mm/min for loading and unloading. The first sample I01 (100x95x63mm) is totally compressed where "I" designs for samples tested at I2M laboratory. Several cycles are then imposed for the second sample I02 at different strain levels 20%, 25%, 30%, 35%, 40% and three cycles per level. All tests are carried out at the same strain velocity of 0.077%/sec. Sample I02 is used to put into practice the cyclic test.

Table III.2: Summary of compression tests on large size samples without CCD cameras

Name	Sample size (mm^3)	Conf.*	Cycle	Teflon	Initial thickness (mm)	MCR* (%)	DR* (mm/sec)	Notes
I01	95x100x63				63	Maximum	0.05	Test until maximum consolidation
I02								Put into practice cyclic test
I03	80x100x65	×	×	×	65			Check Teflon's antifriction capacity
I04	100x100x65	×	×	×	65	20, 25, 30, 35, 40	0.05	Determine the destructive starting zone/point of the material in confined test.
I05	90x90x65		×		65	20, 25, 30, 35	0.05	Determine the destructive starting zone/point of the material in non-confined test. Compare with confined test.

with : *Conf.* = Confinement*

MCR= Maximum compression rate*

DR = Displacement rate*

The confinement device composes of four PMMA plates combined to machine jaw through bolts and glued in order to obtain an interior space of 100x100x100mm. Consequently, the upper jaw deviate 0.5mm from each confinement device side so that the applied force is distributed all over the sample surface while assuring that no fiber is able to be pulled out through these holes during the tests (Figure III.5, Figure III.8b).

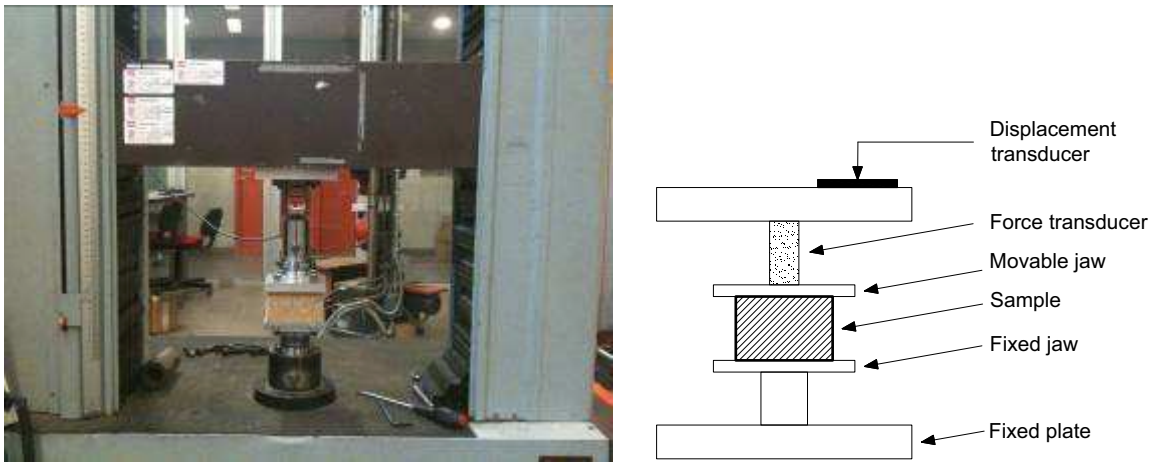

Figure III.4 : Test set-up without CCD cameras

Figure III.5: Confinement device

The friction influence is well-observed during confined tests at Institute P' of Poitiers as the confined test is firstly carried out under CCD cameras there. If we can limit this influence, the behavior of the material becomes purely compressive without taking into account the friction between the sample lateral with the

confinement device. A transparent ultra-thin film of Teflon of 3-5µm thickness is then given as a solution for anti-friction which will be verified by test with sample I03. Teflon will be pasted on 2 parallel faces as indicated in Figure III.6. However, as observed, Teflon may only reduce the friction but not totally eliminate it (Paragraph IV.1), however it is still pasted on four confinement device for cyclic test with sample I04 in order to reduce as much as possible friction effect on sample behavior. A pre-load of 2N will be applied to assure a plan shape of the sample surface. Another cyclic test is also carried out on sample I05 without confinement in order to have full comprehension of the material behavior under different working conditions.

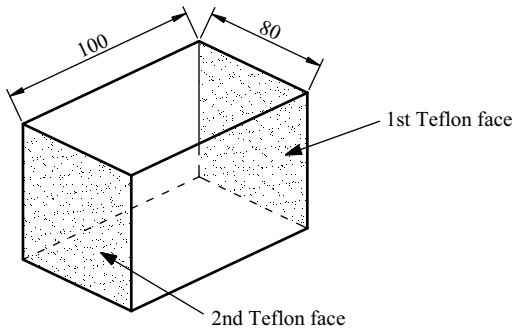

Figure III.6 : Teflon position in compression test with sample I02

b) Compression tests under CCD cameras

In Institute P' of Poitiers, two samples are tested at the same strain rate of 5mm/min for loading and unloading. The first sample P01 (100x100x63mm) is totally compressed in order to put into practice compression test under CCD cameras as well as to test correlation softwares. The second sample P02 is compressed until 50%. The detail description of each test is presented in the Table III.3 where "P" at the beginning of the sample name signifies for samples tested at Institute P' of Poitiers.

Table III.3: Summary of compression tests on large size samples with CCD cameras

Name	Conf.*	Cycle	Teflon	Initial thickness (mm)	MCR* (%)	Strain velocity (%/sec)	DR* (mm/sec)	Notes
P01	×	×		65	50	0.128	0.083	Validation of compression test. Test non-exploited
P02	×	×	×	65	50	0.128	0.083	

Where :

Conf. = Confinement*
MCR = Maximum compression rate
DR = Displacement rate

Compression tests are carried out on an Instron Model 1185 testing machine with 10T of load capacity and 200kg of calibre, operating at a constant displacement rate 5mm/min for loading and unloading, in which every single sample is placed between two CCD cameras (Figure III.7). These two cameras are positioned to obtain the same resolution of about 65µm/pixel with light-supported by an adjustable lamp, which then gives us desired contrast of images. The confinement device is the same with the one used in the tests without CCD cameras (Figure III.8b). This experimental set-up allows us to record at the same time the evolution of the deformation of two parallel faces of the mats during the compression. The result data of one face will be then exploited by the mark tracking method while the result of the other will be explored by the image correlation method, in order to obtain surface strain field (Figure III.8, Figure I.12). The details of image correlation technique will be described in section III.4. The mark tracking method demands a surface preparation where artificial marks are uniformly created with a horizontal distance of about 10cm by a felt-tip. Marks have a circular form of about Ø2-3mm. These marks are not required to be the same but to have enough contrast to be captured by camera and analyzed with the mark tracking method (Figure III.8b, Figure I.12a). A test at the microscopic level (resolution 8µm/pixel) is also carried out in for thermal surface analysis; however the results are not clear enough to be presented. Consequently, this test stays as an experiment without being exploited.

Figure III.7 : Set-up for test under CCD cameras

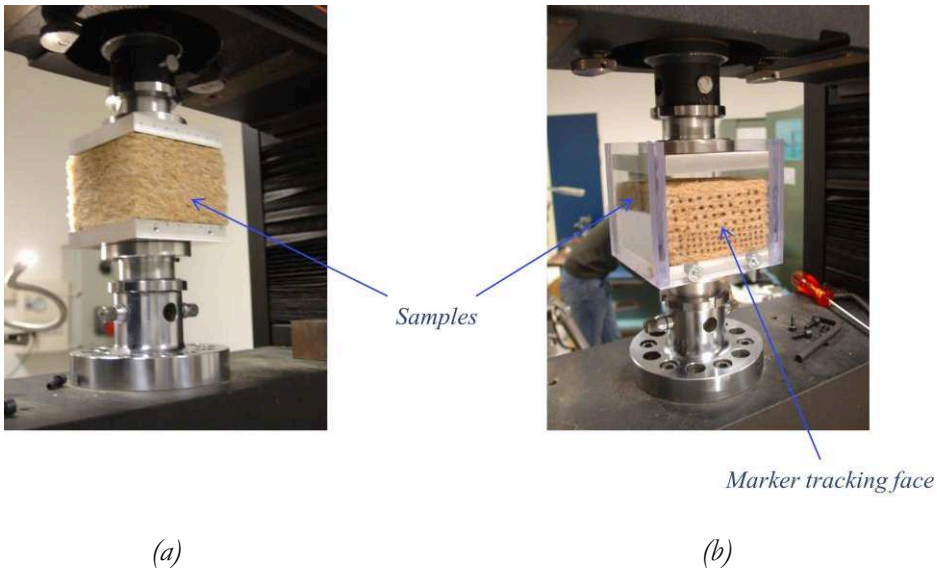

Figure III.8: Sampled tested in unconstrained (a) and constrained (b) compression tests.

The image recording devices are CCD cameras, equipped with a highly sensitive SONY type 1/1.8 progressive CCD sensor, Marlin F-201B, used in monochrome mode. The cameras possess a resolution of 1600x1200pixels and give out a sequence of 10-bits digital images in which each image corresponds to a different load step. The maximum frame rate of the camera is 12.5Hz with IEEE 1394 IIDC interface. However, in this study, images are acquired at 0.5fps (frame per second), corresponding to 0.00128 uniaxial strain or 0.0833mm. The images of two different faces of the sample are then transferred to a frame grabber plugged into two different PC computers equipped with correlation softwares, where images are stored and directly analyzed to cohe mpute the strain field thanks to digital image correlation: DEFTAC software for tmark tracking technique and CORRELAV software for the DIC technique.

As the tests are carried out in the laboratory, good image quality demands a light-support from a lamp. Laboratory room conditions are constantly preserved during image acquisition process.

Precision synchronization among the cameras, frame grabber and operators are necessary in order to capture in the same time two image sequences into two different computers, which allow us next to determine the same applied load at each strain step and compare results obtained from two techniques: the mark tracking technique and the image correlation technique. This requirement is manually carried out but no supplement study for the influence of the synchronization on final results.

III.3.2 Compression tests on small samples (H9mm, Ø9mm) at the macroscopic scale

As mentioned above, classical compression tests of cylindrical samples are added in order to validate the representativity of the sample size in the CT-test since there are only two CT-tests. These tests are carried out at the I2M laboratory where each sample is tested at one compression state around 10%, 20%, 30%, 40%, 50%, 60%, 70% at the same displacement rate 7.44µm/s or 0.08%/s. With this rate, the tests may be considered as quasi-static. Samples are introduced into a compression machine which is in fact built for the CT-test and will be described in details in the next section. The compression machine is connected to a load cell of 100N whose results is exported though Picolog software in mV, which allows us to collect continuously and automatically the applied load during the compression test.

In total, twelve cylindrical samples are tested whose details are presented in the following table. Samples are named "IC" which stands for I2M and cylinder.

Table III.4: Summary of compression tests on cylindrical samples

Name	Initial thickness (mm)	MCR* (%)	DR* (µm/sec)	Density
IC01	9	9.9	7.44	0.04
IC02	9	19.4	7.44	0.03
IC03	9	31.4	7.44	0.03
IC04	9	29.7	7.44	0.04
IC05	9	40.8	7.44	0.04
IC06	9	41.2	7.44	0.03
IC07	9	60.5	7.44	0.04
IC08	9	61.8	7.44	0.04
IC09	9	74.7	7.44	0.05
IC10	9	72.1	7.44	0.04
IC11	9	72.1	7.44	0.04
IC12	9	72.1	7.44	0.04

Where :

MCR = Maximum compression rate*

DR = Displacement rate*

III.3.3 Compression tests on small cylindrical samples under microtomography

Two cylinder samples are compressed under microtomography. The first one H9mm, Ø9mm is compressed at different states under cone-beam Nanotom Phoenix X-ray 160NF at the laboratory ICMCB (Institut de Chimie de la matière condensée de Bordeaux). The second one is performed in the beam line ID19 at the European Synchrotron Radiation Facility (ESRF) in Grenoble. These two tests are complementary. This thesis focuses on exploiting the first one at Bordeaux, the second one is studied in one master thesis [77].

a) Test setup for compression

A special set-up has been built in order to carry out compression tests under microtomography. It is composed of two horizontal plates: the lower plate is fixed while the upper plate is mobile and vertically translated with a stepper motorized linear actuator (displacement speed of 2.7mm/s). The sample is constrained in a PMMA tube (internal diameter of about 10mm) guaranteeing an X-ray transparency. The load is transferred perpendicularly to the surface of the sample through the upper plate made in Teflon, which limits the friction with the tube (Figure III.9). The displacement of the upper plate is assured by a Miniature Linear Actuator, 60 mm travel, RS-232 control with ±15µm of precision and this actuator is automatically controlled. The load value is measured by a load cell of 100N. The sample is preloaded from 9.3mm to 9mm.

b) In-situ compression test at laboratory I2M on the Nanotom Phoenix X-ray

The machine is an ultra-precise high-resolution CT system. It is specifically designed for laboratory applications, scanning samples up to 1 kg and 120 mm diameter with a spatial resolution up to 0.5µm/voxel. The chosen spatial resolution of 6µm/voxel depends primarily on the object size (spatial resolution ≤ fiber diameter), which is compatible to observe the full sample with details of the microstructure [14], [15], [58], [72]. The distance between the X-ray source and the detector is 200mm, which assure the most X-ray energy passing through fibers. The spatial resolution of the X-ray machine depends on the distance between the

sample and the X-ray source, which is limited by compression machine size (Figure III.9): it is positioned as much close to the X-ray source as possible. Consequently, the resolution of 6μm/voxel is the optimum resolution that we can obtain. This resolution was proved to adapt for compression tests on the studied material [72]. The chosen sample size is larger than the one of morphological representative elementary volume (REV) which was determined to be about 13mm^3 (3.8×3.8×0.9mm^3, 0.9 corresponding to the direction of fiberboard thickness) in the previous study [72] and depends on the capacity X-ray machine.

The parameters of the X-ray microtomography test are presented in the following Table III.5.

Table III.5 : Parameters of microtomography test

Sample	Cylinder H9mm, Ø9mm at I2M, Bordeaux
X-ray machine	Nanotom Phoenix X-ray
Acceleration Voltage	65kV
e-Beam current	240μA
Tube operation mode	2
X-ray filter	Non
Focal spot size	≤ 1μm
CCD X-ray detector	2304x2304pixels
Scanning volume	1849x1864x1804voxels
Spatial resolution	6μm/voxel
Projection number	1440
Angular increment	0.36°
Scanning time	33min

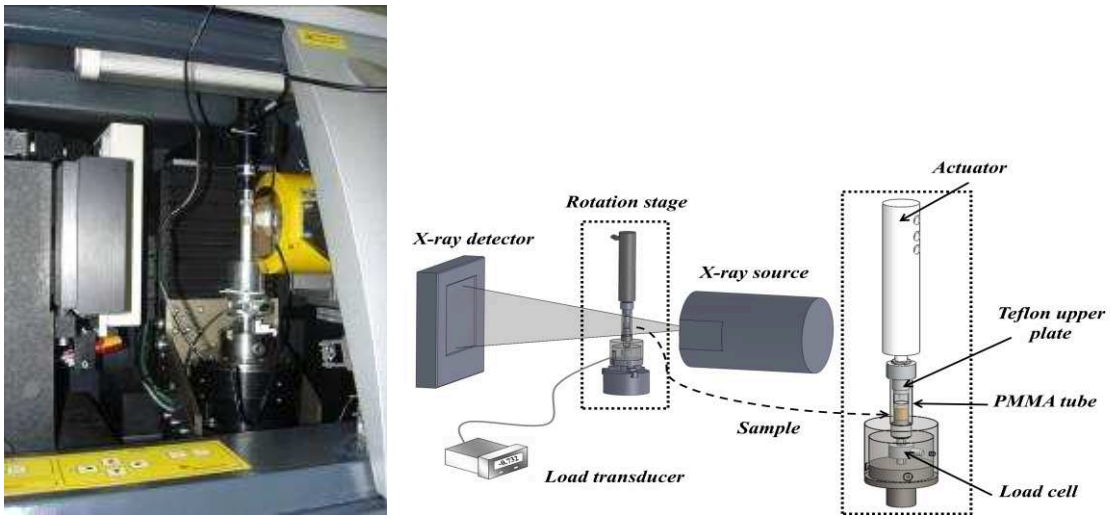

Figure III.9 : Schematic image of Nanotom Phoenix X-ray scanner, developed in laboratory for Wood/PES material

The test protocol is: from a reference state, the sample is loaded from a predetermined displacement corresponding to each compression increment of about 5% in small deformation (or 4.9% when converted into large deformation). This displacement value is required by DVC process in order to obtain good correlation between two consecutive states. For each loaded state, 1440 radiographies are acquired (acquisition time 33min, U=65kV, I=240µA) after the applied force becomes stable (about one minute after finishing loading). Then the sample is subjected to the next scan. Table III.6 summarize eight compression states that are performed on sample.

Table III.6: Imposed compression rate in case of large deformation

State	Displacement (µm)	Imposed compression rate (%)
0	0	0
1	450	4.9
2	870	10
3	1332	15
4	1770	20
5	2220	25
6	2640	30
7	3102	34.6
8	3546	40

As the compression machine is moved and repositioned after each scan in order to verify and to assure the intensity uniformity of the CCD detector, a linear state of branch DomiLine 30 is used to accurately reposition in one direction the whole compression device (center of detector), including the actuator, the sample and the load cell. The whole sample displacements do not influence the morphological measurements but is quite sensible for DVC strain measurement. This device has a stainless steel slide guide, external and internal slides in aluminium profile with a low coefficient of friction and a very fine adjustment (0.05mm). The adjustment direction is perpendicular to the X-ray source (Figure III.10).

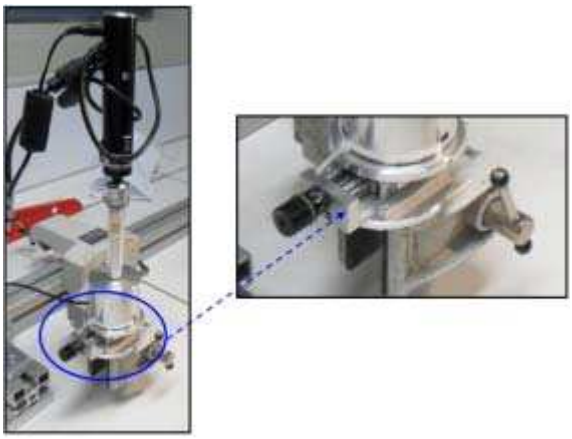

Figure III.10: Linear stage DomiLine 30

c) In-situ compression test at the ID19 beamline in ESRF

This test is to complement the first CT-test carried out at I2M laboratory. Same test set-up is used for the second test. The X-ray machine performs parallel-beam source with the energy of 12keV (with 1.03 Angstrom of wave length) with a spatial resolution of 7.48µm. The sample, which is a cylindrical of Φ9mm and 10,8mm height, is tested at 15 compression states (from 4.9% to 38%). The microtomographic images are recorded on a CCD camera of 2048x2048pixels and then reconstructed into a volume of 2048^3voxels. This resolution is chosen based on CT-test at I2M laboratory in order to in the same time obtain a sufficiently large volume and have lumens disappeared. This choice will facilitate the morphological analysis while still assuring a good acquisition of the PES fibers. The exploitation of this test is made otherwise in the context of a master student work which gives similar results [77].

d) Volume extraction from X-ray microtomography test

3D CT-images are reconstructed as a sequence of 3D raw greyscale volumes (along the z-direction) from 1440 rotated radiographies where each voxel represents the X-ray absorption at that point, thanks to the filtered back projection algorithm in 32bits images. Each 32bits image occupies about 30 GB of memory which is too big for storage and analysis. Consequently, it is downloaded to 8bits greyscale while preserving the dynamic of voxel intensity and obtaining a good contrast between the fibrous phase and the porous phase. However, there is no difference of contrast between the wood fibers and the PES fibers.

We observed also defaults such as "ring-artifact" and noise on microtomographic images which may be due to the reconstruction software, the beam hardening and the temperature of the X-ray tube (Figure III.11). Almost all defaults will be eliminated later after the binarization and the filtering operations.

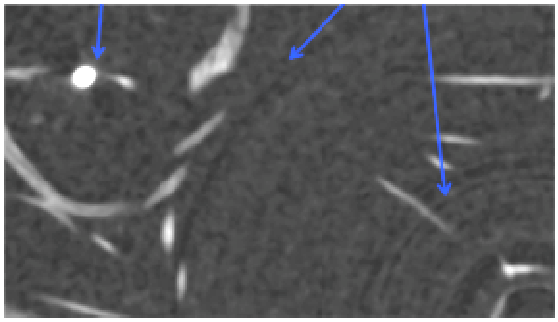

Figure III.11: Defaults in CT-images (350x200pixels)

A limitation of the conic X-ray beam is that there are two zones, upper and lower zones in contact with Teflon supports which are not well reconstructed since X-ray absorption at these zones is influenced by the Teflon absorption (Figure III.12, Figure III.14). They cannot be either observed or analyzed. In order to avoid this phenomenon or so-called boundary phenomenon due to cutting and Teflon, sub-volumes are transversally (Figure III.13) and longitudinally (Figure III.14, Figure III.15) extracted depending on which treatment will be done on the images: morphological measurement or DVC. There is no size difference in transversally extraction; the chosen size is 1024x1024 pixels or 6.144x6.144mm². However, grey level requirements are vertically different for morphological analysis and DVC calculation: the DVC only demands a sufficient distinction in grey level between fibers and pores which can be easily visually perceived. This fact allows us to extract the largest zone possible at almost the same thickness of a non-extracted sample : only about 50 slices are excluded from each support-to-support volumes and support-to-support of initial state is 1501 pixel, corresponding to 9.006mm. But to the contrary, the morphological analysis requires a quite clear contrast between two mentioned phases, i.e. grey level presented as in Figure III.12b can be treated with DVC but not for morphological operations. Therefore, for morphological operations, sub-volumes with slices possessing a constant mean grey level are chosen (Figure III.14).

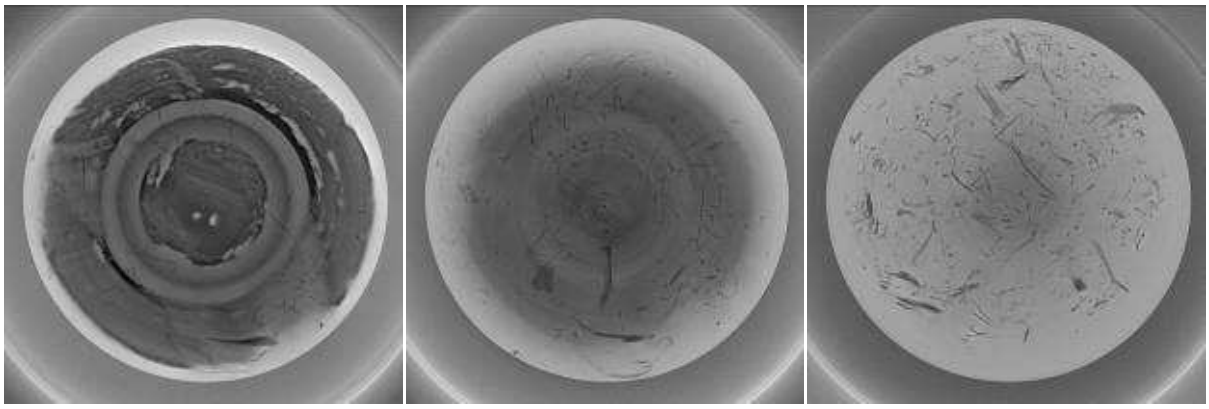

(a) (b) (c)

Figure III.12 : 2D visualization of (a, b) unwell-reconstructed zone and (c) well-reconstructed zone

Sub-volumes are horizontally extracted at the same position with assumption that there is no horizontal displacement of fibers, or this displacement is neglected which results in a very small tranversal strain of the sample. This assumption is confirmed in the next paragraphs V.2 and V.3.

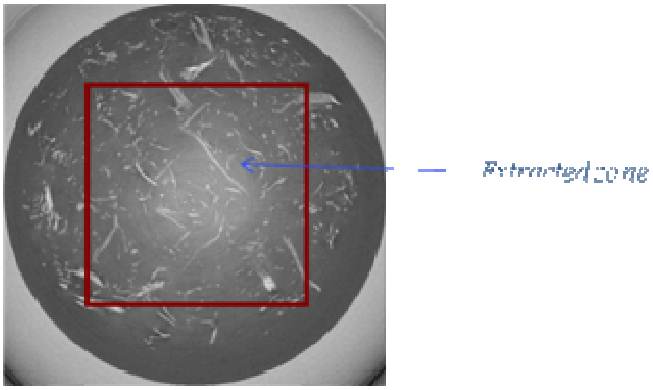

Figure III.13:2D horizontal visualisation of extracted zone 6²mm² (1024²pixels)

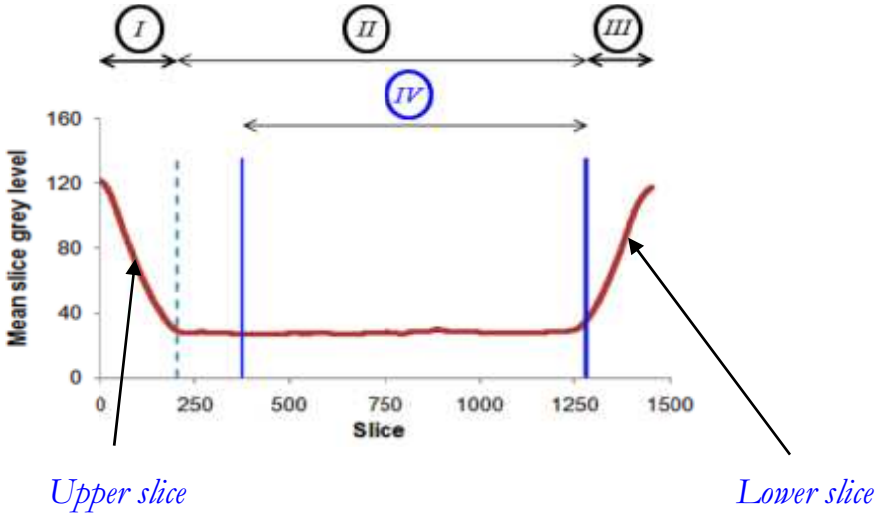

Figure III.14: Mean grey level histogram of each slice along the sample thickness at the initial state (1024x1024x1450pixel). Slice 0 corresponds to upper slice and slice 1450 corresponds to lower slice respectively

(I), (III) Upper and lower unwell-reconstructed zones of the sample

(II) Well-reconstructed zones of the sample

(IV) Well-reconstructed zones of the sample employed in studies with strain field by image correlation

The sub-volume sizes for the DVC analysis are greater than those of the morphological analysis. It means that for the morphological operations, we do not have the same volumes evaluating during the compression, which are then manually and visually obtained and confirmed later with DVC. Starting with the largest well-reconstructed sub-volume of last state (state 8), morphological sub-volumes are determined from a sub-volume to the previous one, which assures the most resemblance of the first and the last slice of two consecutive sub-volumes. The size of extracted volumes is illustrated in Figure III.15.

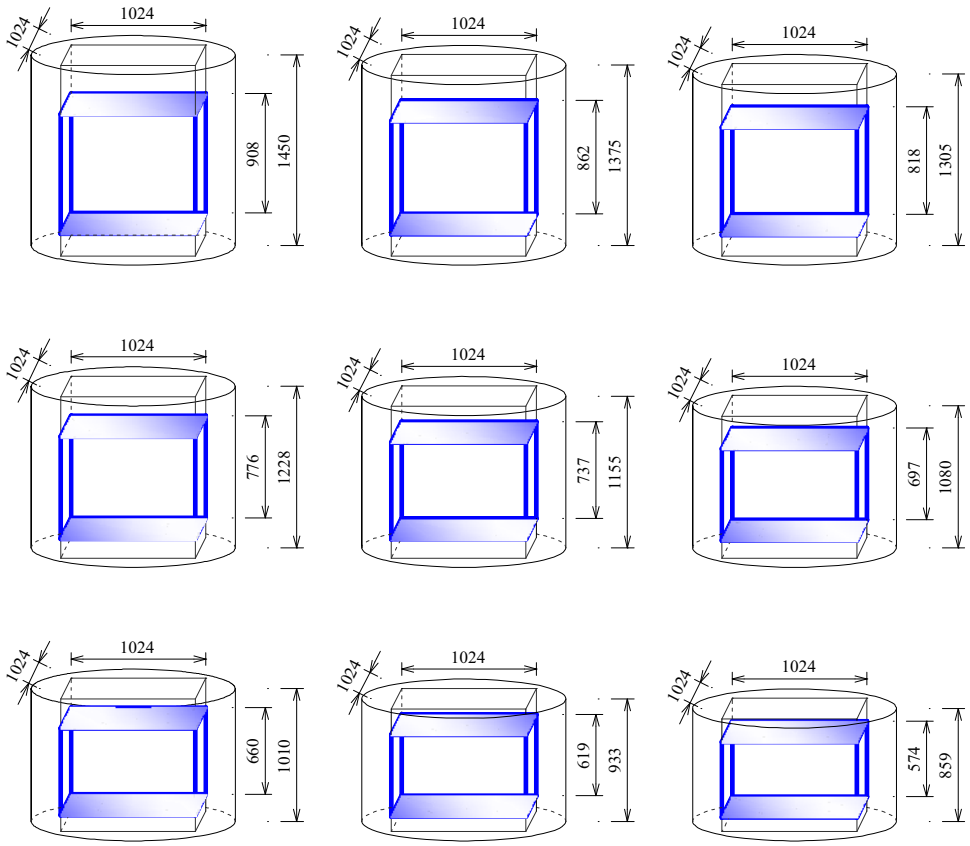

Figure III.15: Well-reconstructed sub-volumes for morphological measurements which evolve during compression

III.4 Measurement methods of strain field by the image correlation

Two techniques that are based on image correlation and studied in this thesis are the digital image correlation (DIC) for 2D strain field analysis and the digital volume correlation (DVC) for 3D full strain field study. DVC is the 3D extension of DIC. As the techniques are similar, we will only describe the detail of DVC technique.

The detail of DVC is described below [41]. The technique consists in tracking the position of the same physical points shown in a reference image and a deformed image (Figure I.13). To achieve this, a volume subset D of voxels is identified on the speckle pattern around point of interest on a reference image and their corresponding location determined on the deformed image (Figure I.13). We note X and x the coordinates, in voxels, of a same point in the reference state and the deformed state. Both configurations are linked by the material transformation $\phi : \underline{x} = \phi(\underline{X})$. For a subset D centered at the point X_0 in the reference state, ϕ is approximated by its expansion at the first order corresponding to a rigid body motion combined with a homogeneous deformation:

$$\underline{\phi}(\underline{X}) = \underline{X} + \underline{U}(\underline{X}) \approx \underline{X} + \underline{U}(\underline{X}_0) + \frac{\partial \underline{U}}{\partial \underline{X}}(\underline{X}_0).(\underline{X} - \underline{X}_0) \quad (3.1)$$

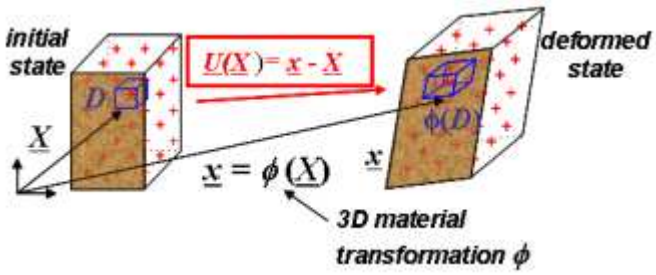

Figure III.16: Principle of DVC [41]

The displacement $\underline{U}\left(\underline{X}_0\right)$ of the subset center gives the intensity $U(u,v,w)$ of the rigid body translation. The local displacement gradient expression $\frac{\partial \underline{U}}{\partial X}(\underline{X}_0)$ includes the rigid body rotation and the local stretch of the subset volume and is characterized by 9 parameters: $\left(\frac{\partial u}{\partial x},\frac{\partial u}{\partial y},\frac{\partial u}{\partial z},\frac{\partial v}{\partial x},\frac{\partial v}{\partial y},\frac{\partial v}{\partial z},\frac{\partial w}{\partial x},\frac{\partial w}{\partial y},\frac{\partial w}{\partial z}\right)$. Generally for small local strains, the local gradient component can be neglected and so the approximation can be simply assimilated to a translation. The best parameters characterizing the approximation (3 or 12 scalars) are those which minimize some correlation coefficient C. It measures the degree of similarity of grey level distributions in D and its transformed one by ϕ . We take a formulation insensitive to small contrast and brightness fluctuations which may appear in images: a normalized cross correlation formulation based on grey level gaps with respect to the average on the subset.

$$C = 1 - \frac{\sum_{\underline{X} \in D} (f(\underline{X}) - \overline{f}_D).(g(\underline{\phi}(\underline{X})) - \overline{g}_D)}{\sqrt{\sum_{\underline{X} \in D} (f(\underline{X}) - \overline{f}_D)^2} . \sqrt{\sum_{\underline{X} \in D} (g(\underline{\phi}(\underline{X})) - \overline{g}_D)^2}} \quad (3.2)$$

where $\underline{X}$ refers to voxels in D, f and g are respectively the grey levels in the undeformed and deformed images, $\overline{f}_D$ and $\overline{g}_D$ are their averages over D and $\underline{\phi}(\underline{X})$.

a) Subvoxel accuracy

A trilinear interpolation of the grey levels in the deformed image is used in order to calculate the grey level variations between two adjacent voxels. In this way, it is possible to achieve the position of the subset D in fractions of voxels thanks to the subvoxel precision. Trilinear interpolation is a method of multivariate

interpolation on a 3-dimensional regular grid. It approximates the grey level of an intermediate point (x, y, z) within the local axial rectangular prism, using data on the lattice points. Considering the voxel with the coordinates $\underline{X}(x, y, z)$ satisfies the condition $j < x < j+1, i < y < i+1, k < z < k+1$ and has the grey level defined by:

$$\begin{aligned} v_{ijk}(x,y,z) = g(i,j,k)) + \varsigma(z-k) + \beta(x-j) + \chi(x-j)(z-k) + \gamma(y-i) \\ + o(y-i)(z-k) + \psi(x-j)(y-i) + \omega(x-j)(z-k) \end{aligned} \tag{3.3}$$

where

$$\begin{aligned} \varsigma &= g(i,j,k+1) - g(i,j,k) \\ \beta &= g(i,j+1,k) - g(i,j,k) \\ \chi &= g(i,j+1,k+1) - g(i,j,k+1) - g(i,j+1,k) + g(i,j,k) \\ \gamma &= g(i+1,j,k) - g(i,j,k) \\ o &= g(i+1,j,k+1) - g(i,j,k+1) - g(i+1,j,k) + g(i,j,k) \\ \psi &= g(i+1,j+1,k) - g(i,j+1,k) - g(i+1,j,k+1) + g(i,j,k) \\ \omega &= g(i+1,j+1,k+1) + g(i,j+1,k) + g(i+1,j,k) + g(i,j,k+1) \\ &\quad - g(i,j+1,k+1) - g(i+1,j,k+1) - g(i+1,j+1,k) - g(i,j,k) \end{aligned} \tag{3.4}$$

b) Minimisation

The parameters of the approximation ϕ are resumed in the vector $\underline{P} = (u, v, w)$ or

$$\underline{P} = \left(u, v, w, \frac{\partial u}{\partial x}, \frac{\partial u}{\partial y}, \frac{\partial u}{\partial z}, \frac{\partial v}{\partial x}, \frac{\partial v}{\partial y}, \frac{\partial v}{\partial z}, \frac{\partial w}{\partial x}, \frac{\partial w}{\partial y}, \frac{\partial w}{\partial z} \right) \tag{3.5}$$

The success of minimization process depends on the start point $\underline{P_0}$. In order to avoid the convergence on a local minimum, $\underline{P_0}$ is chosen near the final solution and is the solution of $\underline{P}$ for a unique translation in entire voxels. According to the retained formulation, $\underline{P_0}$ is equal to (u_0, v_0, w_0) or $(u_0, v_0, w_0, 0, 0, 0, 0, 0, 0, 0, 0, 0)$. This estimation in entire voxels is obtained by a direct systematic calculus which explores all the possible entire translations in the neighbourhood of a position

which has been deduced from the known translation of the previous point. This process is the first step of the measurement procedure. In a second step, we research a finer solution of $\underline{P}$ with an automatic first-gradient minimization procedure whose mathematical expression is given by the following formula:

$$\underline{P}_{n+1} = \underline{P}_n - a \frac{\frac{\partial C}{\partial \underline{P}}(\underline{P}_n)}{\left\| \frac{\partial C}{\partial \underline{P}}(\underline{P}_n) \right\|} \tag{3.6}$$

with $0 < a \leq 1$ and where $\|.\|$ is the Euclidian norm.

The parameter a defines the distance between two successive solutions and is initialized to 0.5, then is divided by 2 when C increases again.

c) Strain calculation by finite difference

As DVC gives displacement at each grid point, displacement tensor $\underline{U}(u,v,w)$ at one grid $\underline{X}_0$ point can be able to determine by displacement of neighbour grid points by the method of finite difference. Considering one point defined by three vectors $(d\underline{X}_1, d\underline{X}_2, d\underline{X}_3)$ (red point in Figure III.17) which are created by six neighbouring points at the initial state (Figure III.17). The length at the initial state for each vector is $2l_0$, corresponding double of distance-to-distance of grid points (Figure III.17).

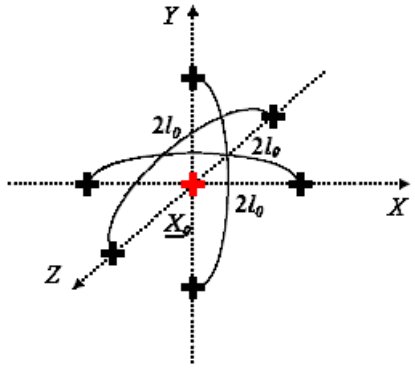

Figure III.17: Studied point in initial grid system

These three vectors define a parallelepipedic volume around the studied point where the deformation tensor is considered homogeneous (Figure III.18a). The three vectors $(d\underline{X}_1, d\underline{X}_2, d\underline{X}_3)$ in initial state are related to its deformed vectors $(d\underline{x}_1, d\underline{x}_2, d\underline{x}_3)$ through the deformation gradient tensor $\underline{\underline{F}}$ as:

$$\begin{bmatrix} d\underline{x}_i = F_{xx}dX_i + F_{xy}dY_i + F_{xz}dZ_i \\ d\underline{y}_i = F_{yx}dX_i + F_{yy}dY_i + F_{yz}dZ_i \\ d\underline{z}_i = F_{zx}dX_i + F_{zy}dY_i + F_{zz}dZ_i \end{bmatrix} \tag{3.7}$$

where $$d\underline{X}_i = \begin{bmatrix} d\underline{X}_i \\ d\underline{Y}_i \\ d\underline{Z}_i \end{bmatrix} \text{ and } d\underline{x}_i = \begin{bmatrix} d\underline{x}_i \\ d\underline{y}_i \\ d\underline{z}_i \end{bmatrix} \tag{3.8}$$

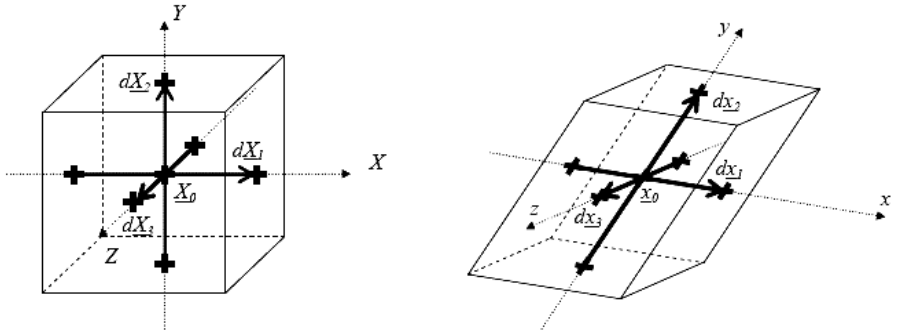

(a) (b)

Figure III.18: Parallelepipedic volume at initial (a) and deformed (b) state

The displacement of $\underline{X}_0(X_0, Y_0, Z_0)$ to $\underline{x}_0(x_0, y_0, z_0)$ through the displacement vector $\underline{U}(u, v, w)$ allows us to determine components of the displacement tensor $\underline{\underline{H}}$ by finite differencies as:

$$\begin{bmatrix} \frac{\partial \alpha}{\partial x} \approx \frac{\alpha(X_0 + l_0, Y_0, Z_0) - \alpha(X_0 - l_0, Y_0, Z_0)}{2l_0} \\ \frac{\partial \alpha}{\partial y} \approx \frac{\alpha(X_0, Y_0 + l_0, Z_0) - \alpha(X_0, Y_0 - l_0, Z_0)}{2l_0} \\ \frac{\partial \alpha}{\partial z} \approx \frac{\alpha(X_0, Y_0, Z_0 + l_0) - \alpha(X_0, Y_0, Z_0 - l_0)}{2l_0} \end{bmatrix} \tag{3.9}$$

where $\alpha = u, v, w$

Considering the initial configuration $\underline{X}(X, Y, Z)$, the current configuration $\underline{x}(x, y, z)$ with displacement tensor $\underline{U}(u, v, w)$, the deformation gradient tensor is defined as:

$$\underline{\underline{F}} = \frac{d\underline{x}}{d\underline{X}} = \underline{\underline{I}} + \frac{d\underline{u}}{d\underline{X}} \tag{3.10}$$

and

$$F_{ij} = \frac{\partial x_i}{\partial X_j} = I_{ij} + \frac{\partial u_i}{\partial X_j} \tag{3.11}$$

The components of the deformation gradient tensor are obtained by solving the equation system (3.7, 3.9).

The Green-Lagrange deformation tensor is determined as:

$$\underline{\underline{E}} = \frac{1}{2}\left(\underline{\underline{F}}^T \underline{\underline{F}} - \underline{\underline{I}}\right) = \frac{1}{2}\left(\frac{\partial \underline{u}}{\partial \underline{X}} + \left(\frac{\partial \underline{u}}{\partial \underline{X}}\right)^T + \left(\frac{\partial \underline{u}}{\partial \underline{X}}\right)^T \frac{\partial \underline{u}}{\partial \underline{X}}\right) \tag{3.12}$$

In the case of small deformation of uniaxial test, the longitudinal strain can be expressed as:

$$\varepsilon = \frac{h}{h_0} - 1 < 0 \tag{3.13}$$

where h, h_0 are respectively deformed and initial sample thickness.

Identically, in the case of a large deformation of uniaxial test, the longitudinal strain is defined as:

$$e = \frac{1}{2}\left(\frac{h^2}{h_0^2} - 1\right) < 0 \tag{3.14}$$

The conversion expression between the small strain and the large strain can be determined as

$$\begin{aligned} e &= \frac{1}{2}\left[\left(1+\varepsilon\right)^2 - 1\right] \\ \varepsilon &= \sqrt{2e+1} - 1 \end{aligned} \tag{3.15}$$

For a better graphical illustration, in the future, we use positive value of ε and e, and Eq. (3.15) becomes

$$\begin{aligned} e &= \frac{1}{2}\left[1 - \left(1-\varepsilon\right)^2\right] \\ \varepsilon &= 1 - \sqrt{1-2e} \\ e, \varepsilon &\geq 0 \quad ; \quad e \leq 0.5 \end{aligned} \tag{3.16}$$

The relation between e and ε is illustrated on Figure III.19.

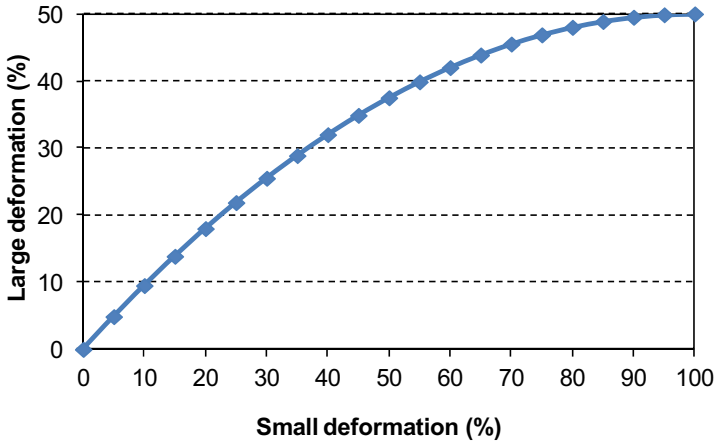

Figure III.19: Relation between large deformation e and small deformation in compression ε

As for the CT-tests, an imposed strain step corresponding 5% in small deformation or 4.9% in large deformation case is carried out, which allows us to treat the strain field in large deformation solution. The conversion of the small deformation values into the large deformation values in the CT-test is presented in Table III.7. In order to have the same base of comparison, experimental data of other scales (macroscopic and mesoscopic) are all converted into the large deformation case.

In this study, DVC and strain calculations are performed by the academic software (CorrelVol [78]) developed in the Pprime Institute, between two consecutive compression steps with small strain increment in order to obtain better correlation results, assuming that the material transformation ϕ *is homogeneous for each correlation domain D. The algorithm of DVC implemented in CorrelVol is presented in*

Figure III.20.

Table III.7: Conversion of small deformation value into large deformation value in CT-test

Small deformation (%)	0	4.9	10	15	20	25	30	34.6	40
Large deformation (%)	0	4.8	9.5	13.9	18	21.9	25.5	28.6	32

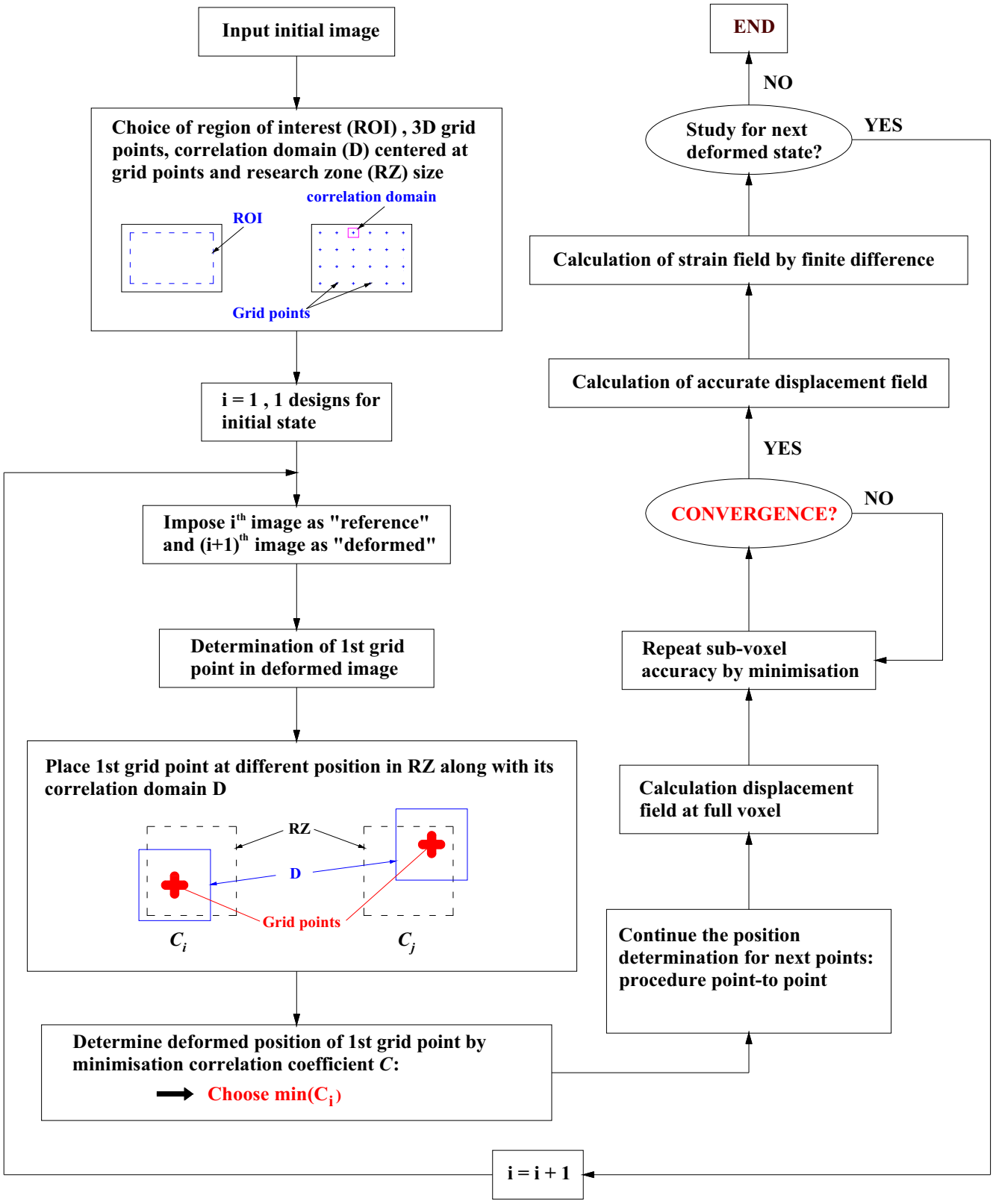

Figure III.20: Algorithm of DVC implemented in the software CorrelVol

III. 5 Conclusion of chapter III

This chapter details all types of compression tests that are carried out in this thesis, including the choice of studied volumes. Each type is destined for different objective and corresponds to different sample scales. Experimental data are then needed to be exploited and then validated by theoretical and experimental models. But in order to do that, we need to gather all necessary information of the microstructure.

This chapter also reveals some specific difficulties for further analysis. Firstly, the difficulty in sample preparation may create samples of similar size but different characteristics; the classical tests on cylindrical samples (Φ9mm, H9mm) must take into account this variation while validating the representativity of the chosen size of the CT-test. Secondly, because of this variation, exploitation based on the CT-test must use the pure parameters obtained from this test (i.e. Young's modulus for numerical simulation) without using the average value from all other samples of the same size. Finally, the defaults such as noise and some ring artifact appearing on microtomographic images during the CT-test will certainly disturb image analysis (microstructure analysis and DVC study). Consequently, we will try our best to decrease these inconveniences during the filtering of the 3D images.

Chapter IV: Morphological characterization of the microstructure

In this chapter, we will introduce the microstructure characterization by image analysis based on principles of the mathematical morphology [60], [61]. The microstructure characterization is performed on microtomographic images obtained from the CT-test. Four microstructure parameters are: the volume fraction, size, orientation and the spatial distribution of different phases (pore network, fiber network: all the fibers and separated wood and PES fibers). In order to obtain these parameters, three principal structure operations are performed : the segmentation of the fibrous phase from the porous phase, the filling the lumens of wood fibers and the segmentation of wood fibers from PES fibers.

The microstructural properties of three among all compression states are mainly studied: the initial one, 18.4% and 31.6%, as there is no clear difference in morphological properties for two consecutive states, which are next put into relation with compression behavior in next chapters.

All structure operations are carried out thanks to two softwares Aphelion™ [62] and ImageJ [63], based on the algorithms developed by J. Lux [72] and during this thesis.

IV.1 Basic theory of mathematical morphology

Mathematical morphology is a theory and technique for morphological analysis of structures, which is based on set theory, lattice theory, topology and random functions. The full detail of these theories, which is not all presented here, can be found in [60], [61]. From the first development by the collaborative work of Georges Matheron and Jean Serra at the École des Mines de Paris, France 1964 to the quantification of mineral characteristics from thin cross sections, mathematical morphology has found itself in many applications such as edge detection, object segmentation and measurement while preserving the most possible shape characteristics and eliminating noise , skeletons [50], [59], [79], etc. Especially, it supplies an access, along with microtomography test, studying real 3D microstructure configuration put under solicitations without destroying material [13], [80]. Nowadays, many morphological operations are available and implemented in many image analysis softwares (as Aphelion™ used in this study). However, in order to decrease the computational runtime of morphological analysis, raw CT-images which are reconstructed in 32-bit float type must be first converted into 8-bit greyscale and then cropped for image treating (section III.3.3). Morphological measurements in this study are focused mainly on binary images in

8-bits greyscale where the grey level of a pixel (2D images) or a voxel (3D image) is 0 or 1. We designate 1 for the fibrous phase and 0 for the porous phase.

In the first section we will briefly present set theory then we will describe some basic operations of mathematical morphology.

IV.1.1 Set theory

As mentioned before, morphology operations treat all structures, objects or a pixel/voxel assembly in image as sets. In set theory, a set Γ is a complete lattice either in continuous space R^2 / R^3 or in discrete space Z^2 / Z^3 in which for each family of subsets $\{X_i\} \in P$ (P is a set), there exists in Γ : a greatest lower bound $\wedge\{X_i\}$ called infimum and a smallest upper bound $\vee\{X_i\}$ called supremum.

A 3D binary image is consequently a subset of Z^3 where position of each voxel is represented by integer coordinates in Z^3.

IV.1.2 Basic operations

The two basic transformations are dilation, erosion, denoted δ_B and ε_B where B refers to the structuring element in the transformation. This structuring element B is a set which has a given geometry such as a sphere, an octahedron or a cube with a predetermined size to interact with a given image, and is consequently also a subset of Z^3. Most morphological operations are based on a selected combination of these two transformations. The two other so called basic operations formed from this combination are then opening and closing, which are respectively an erosion followed by a dilation and inversely.

Dilation and erosion are all based on Minkowski basic set operations, named "addition" and "subtraction" as

$$R \oplus S = \{r+s | r \in R,\ s \in S\} \tag{4.2}$$

and

$$R \ominus S = \{r | S \oplus \{r\} \subset R\} \tag{4.3}$$

where

R, S studied sets

r, s respectively variable of set *R, S*

Let X and B be subsets of the discrete space Z^3: $X, B \subset Z^3$. The dilation of X by a structuring element (SE) B centered at a voxel b of X is defined as:

$$\delta_B(X) = \bigcup_{b \in B} X_{-b} = \{b : B_b \bigcap X \neq \varnothing\} \quad (4.4)$$

Where X_{-b} is the translated set of X_b defined as

$$X_{-b} = \{-x, x \in X_b\} \quad (4.5)$$

The dilation makes images objects grow in size and results objects containing centers of all structuring elements B which has at least one common point with X (Figure IV.1c).

The erosion of X by a structuring element B centered at b is defined as:

$$\varepsilon_B(X) = \bigcap_{b \in B} X_{-b} = \{b : B_b \subseteq X\} \quad (4.6)$$

On the contrary of dilation, erosion makes images objects smaller and results objects containing centers of all structuring elements B which are totally included in X (Figure IV.1d).

Both dilation and erosion are invariant and increasing. Erosion and dilation are dual operations with respect to image complementation. However while the dilation is commutative and associative, erosion is not. Consequently, the operation combination following the order erosion-dilation is not an inverse of dilation-erosion as it is in the case of opening and closing presented below. These two operations cause great changes to object characteristics (length, contour, volume…) especially when the structuring element is large compared to the object size.

The opening of X by a structuring element B centered at b is defined as erosion followed by dilation as:

$$\gamma_B(X) = \delta_B(\varepsilon_B(X)) \quad (4.7)$$

This operation will remove capes, isthmus and islands which are smaller than the structuring element and makes the object contour smoother (Figure IV.1e). These properties allow opening to take part in filtering, removing noise and determining object diameter in image. However, small objects which are not noise cannot be recovered once they are removed by opening.

The closing of X by a structuring element B centered at b is defined as a dilation followed by an erosion as:

$$\varphi_B(X) = \varepsilon_B(\delta_B(X)) \quad (4.8)$$

Closing, on the other hand, will fill gulfs, channels and lakes that are smaller than the structuring element (Figure IV.1f) which allows us to fill internal lumens of wood fibers as in following paragraphs.

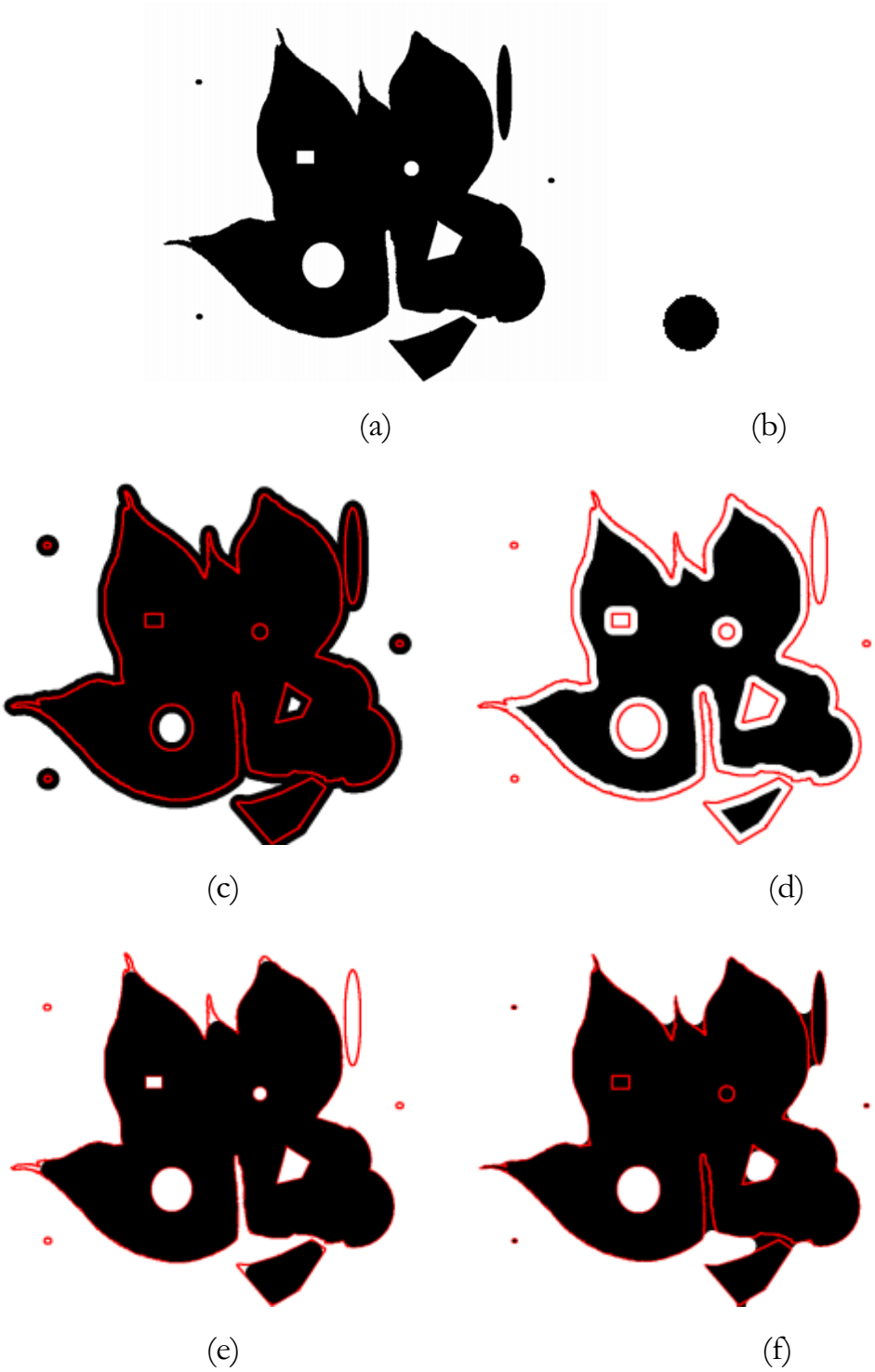

Figure IV.1: Illustration of (a) Initial image (b) Structuring element (c) Dilation (d) Erosion (e) Opening (f) Closing. Red line is the contour of initial objects

IV.1.3 Connectivity

The form of real objects is reflected in images through the grouping of an assembly of pixels or voxels. An assembly of grouped points creates a connected class. In a 3D binary image, there are different types of connectivity (Figure IV.2) depending on which one object can be considered connected or not to another one. Two voxels $p_a(a_1,a_2,a_3)$ and $p_b(b_1,b_2,b_3)$ are considered connected if $|a_i - b_i| \leq m_0$ with $i = 1,2,3$. If $m_0 = 1$, p_a and p_b are connected through 6-connectivity. Respectively, $m = \sqrt{2}, \sqrt{3}$ corresponds to 18-connectivity and 26-connectivity.

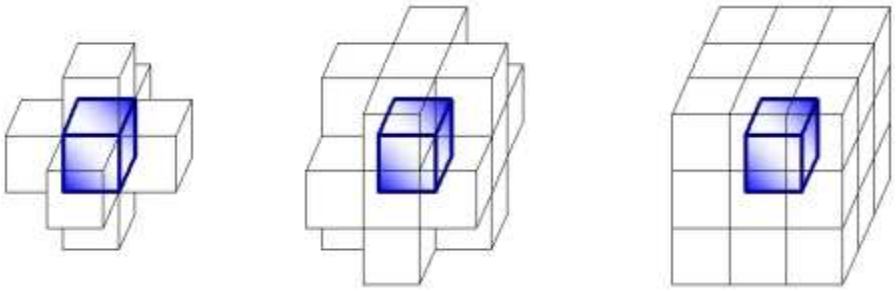

(a) *(b)* *(c)*

Figure IV.2: 3 types of connectivity of a voxel (blue voxel): (a) 6-connectivity (b) 18-connectivity (c) 26-connectivity

Let *T* be an arbitrary space. Any family of set *S* in *P(T)* is called connected class if

- $\varnothing \in S$
- $\forall x \in T : \{x\} \in S$
- $\forall \{R_i\}, R_i \in S : \{\bigcap R_i \neq \varnothing\} \Rightarrow \{\bigcup R_i \in S\}$

with R_i is a subset of *S*.

The notion of connectivity allows us to develop the notion of geodesic reconstruction. Between any two points p_a and p_b of a connected set *X*, the length of the shortest path linking these two points and totally included in *X* is called geodesic distance (Figure IV.3).

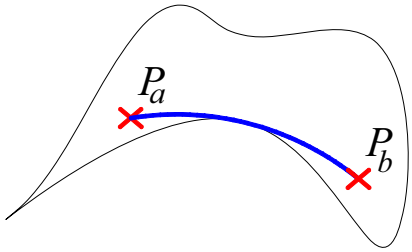

Figure IV.3: Geodesic distance

The notion of geodesic path can be replaced by another notion of the "geodesic disc" $B_{X,\lambda}(z)$ with center z and radius λ which defines a point set in X that has geodesic distance $\leq \lambda$ from z as (Figure IV.4):

$$B_{X,\lambda}(z) = \{y, r_X(z, y) \leq \lambda\} \tag{4.9}$$

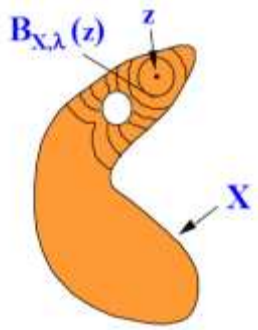

Figure IV.4: Geodesic dilation [61]

Opening by reconstruction can overcome the limitation of opening: while preserving the original contour and section of large objects, it completely removes small and non-connected objects as a good filtering tool. Opening by reconstruction of set Y included in X is carried out in two steps: firstly, erosion on image X with SE of size i which aims at creating a mark image Y for the reconstruction operation. Secondly, reconstruction by dilation is performed on the mark image as reference mask as

$$\delta^{rec}(X,Y) = \bigcup\{\delta_{X,\lambda}(Y), \lambda > 0\} = \bigcup\{\delta_{\gamma_y}(X), y \in Y\} \tag{4.10}$$

This operation is an iterative procedure with λ increasing that applies geodesic dilation $\delta_{X,\lambda}(Y)$ on mark image Y until idempotence as:

$$\delta_{X,i+1}(Y) = \delta_{X,i}(Y) \tag{4.11}$$

where

$$\begin{cases} \delta_{X,i}(Y) = \bigcup \{ B_{X,i}(y), y \in Y \} \\ \delta_{X,i}(Y) = \delta^{(i)}{}_X(Y) = \delta(\ldots\delta(\delta(Y) \cap X) \cap X \ldots) \cap X \end{cases} \quad (4.12)$$

With $\delta_{X,\lambda}(Y)$ and $\delta_X^{(i)}(Y)$ are geodesic dilation on mark image Y based on image X with λ increasing.

By duality, a closing by reconstruction is defined as the reconstruction by erosion from the dilation using a structuring element of size λ (Figure IV.5). In both cases, closing and opening by reconstruction, the contours of objects are not modified.

Figure IV.5: Result of a closing by reconstruction

IV.2 Lumen filling and phase segmentation of wood-based fibrous structure

IV.2.1 Segmentation of fibrous phase from porous phases

The 3D images issued from microtomographic tests show different fiber populations in the same grey level where we can perceive a net contrast between the fibers and the pores, but the frontier between these two phases is blurred and presents a grey level gradient. As mentioned before, the studied material contains about 77.5% in mass of maritime pine fibers and 22.5% thermofusible bicomponent textile fibers or PES fibers for short. Wood fibers are composed of isolated fibers and bundles, showing a strong variability of sizes. Since the wood fibers contain internal lumens, the material exhibits different porosity types: the internal porosity due to the lumens, the external porosity around the fiber and the total porosity including these two porosities. The fibrous phase is separated from

the porous phase by applying a global threshold on the whole image, which directly gives us the total porous and fibrous volume fraction. Normally, the threshold level is obtained in function of the global grey histogram (Figure IV.6). However, since the object boundaries are quite blurred, we have quite a wide range of threshold values to choose. Consequently, porosities obtained from previous studies become precious references [72]. Plus, as a range value of thresholding does not give a large difference of total porosity (Figure IV.6, Table IV.1), we choose the value of 48 as the low level of thresholding which gives the smallest size of internal lumens without dramatically changing fiber contours which allows us to fill easily the lumens of the wood fibers. The noise in the images can be easily removed by simply applying an opening by reconstruction.

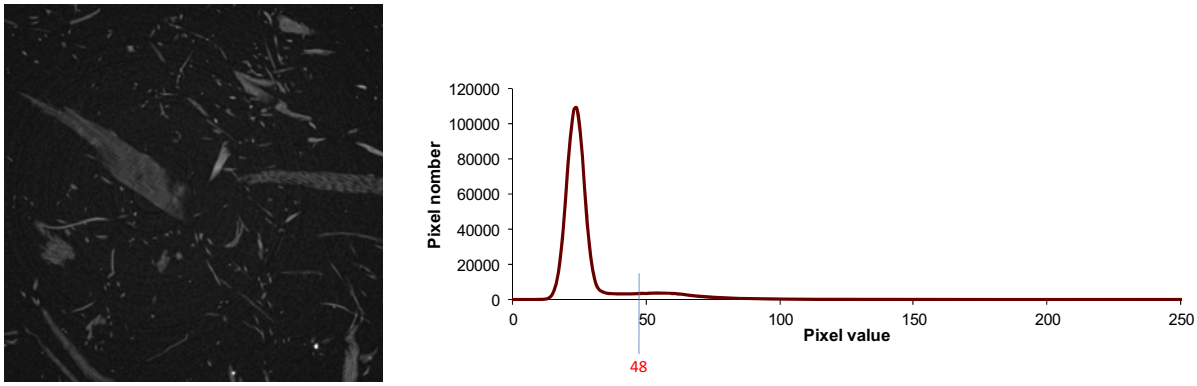

(a) *(b)*

Figure IV.6: Histogram of grey levels (b) of one slice of initial image (a) (Image size 1024x1024pixel)

In a binary image, the porosity is calculated from the black voxel volume as

$$p = \frac{V_p}{V} \tag{4.13}$$

Where V is the total volume of image, V_p may refer to internal, external or total pore volume depending on the volume of the lumens, the pores around fibers or all the pores in the image. Table IV.1 shows the porosity obtained when applying the chosen thresholding value (48) compared to other thresholding values on 3D microtomographic image at the initial state.

Table IV.1: Total porosity of initial image at different threshold values (Image size 1024x1024x908) before lumen filling

Threshold value	Total porosity (%)
45	92,2
46	92,5
47	92,7
48	**92,9**
49	93,2
50	93,4
51	93,6

An estimated porosity can be established in function of the mass fraction and the density of each phase in the material. The estimated external porosity is determined as:

$$p_{ext} = 1 - \rho * (\frac{f_{mPES}}{\rho_{PES}} + \frac{f_{mwood}}{\rho^{*}_{wood}}) \quad (4.14)$$

Respectively for the estimated total porosity:

$$p_{tot} = 1 - \rho * (\frac{f_{mPES}}{\rho_{PES}} + \frac{f_{mwood}}{\rho_{wood}}) \quad (4.15)$$

And the relation between mass fraction and volume fraction is found as:

+ In the case of solid wood fibers:

$$\frac{V_{PES}}{V_{wood}} = \frac{f_{vPES}}{f_{vwood}} = \frac{f_{mPES}}{f_{mwood}} \times \frac{\rho_{wood}}{\rho_{PES}} \quad (4.16)$$

+ In the case of hollow wood fibers:

$$\frac{V_{PES}}{V^{*}_{wood}} = \frac{f_{vPES}}{f^{*}_{vwood}} = \frac{f_{mPES}}{f_{mwood}} \times \frac{\rho^{*}_{wood}}{\rho_{PES}} \quad (4.17)$$

Where

V_{PES}, V_{wood} Volume of PES fibers and solid wood fibers

V^{*}_{wood} Volume of wood fibers including lumens

f_{mPES}, f_{mwood} Respectively mass fraction of PES fibers and solid wood fibers

f_{vPES}, f_{vwood} Respectively volume fraction of PES fibers and solid wood fibers

f^*_{Vwood} Volume fraction of wood fibers containing lumens

ρ_{PES} Density of PES fibers, $\rho_{PES} = 1,38$

ρ_{wood} Density of wood fiber wall, constant for all plants $\rho_{wood} = 1,53$

ρ^*_{wood} Apparent density of wood fiber including lumen, depending on volume fraction of lumen f_{vlumen} : $\rho^*_{wood} = (1 - f_{vlumen})\rho_{wood} < 1,53$

ρ^* Density of the material with internal lumens and external porosity,

$$\rho^* = \frac{m}{V}$$, m is the mass of the material

For example, in the case of wood-based fibrous material with a mass fraction of 77.5% of wood fibers and 22.5% of PES fibers and an estimated volume fraction of 20% of lumen inside the wood fibers, the estimated external and total porosity is respectively 96.4% and 96.6%. However these values are only for reference because we cannot determine exactly the volume fraction of lumens.

IV.2.2 Lumen filling for wood fibers

The internal lumens cannot be well-observed in the CT-images. This depends on the spatial resolution of the CT-tests, the better the resolution is, the larger and the clearer the lumens are. Consequently, the lumens extracted with our CT-tests are not precisely defined. Plus, as later, we are interested in the distribution of fiber diameter, the lumens need to be filled. The algorithm of lumen filling developed by J. Lux [72] which consists of dilation by a SE of an adequate size to disconnect the lumens from external porosity followed by a closing by reconstruction to fill the lumens and ended with an erosion to recover the initial contours of fibers. The porosity of the initial state obtained is 92.3%, about 0.65% less than before filling the lumens. Figure IV.7 and Figure IV.8 show the results of this operation: the contour of fibers does not change significantly, lumens are well filled.

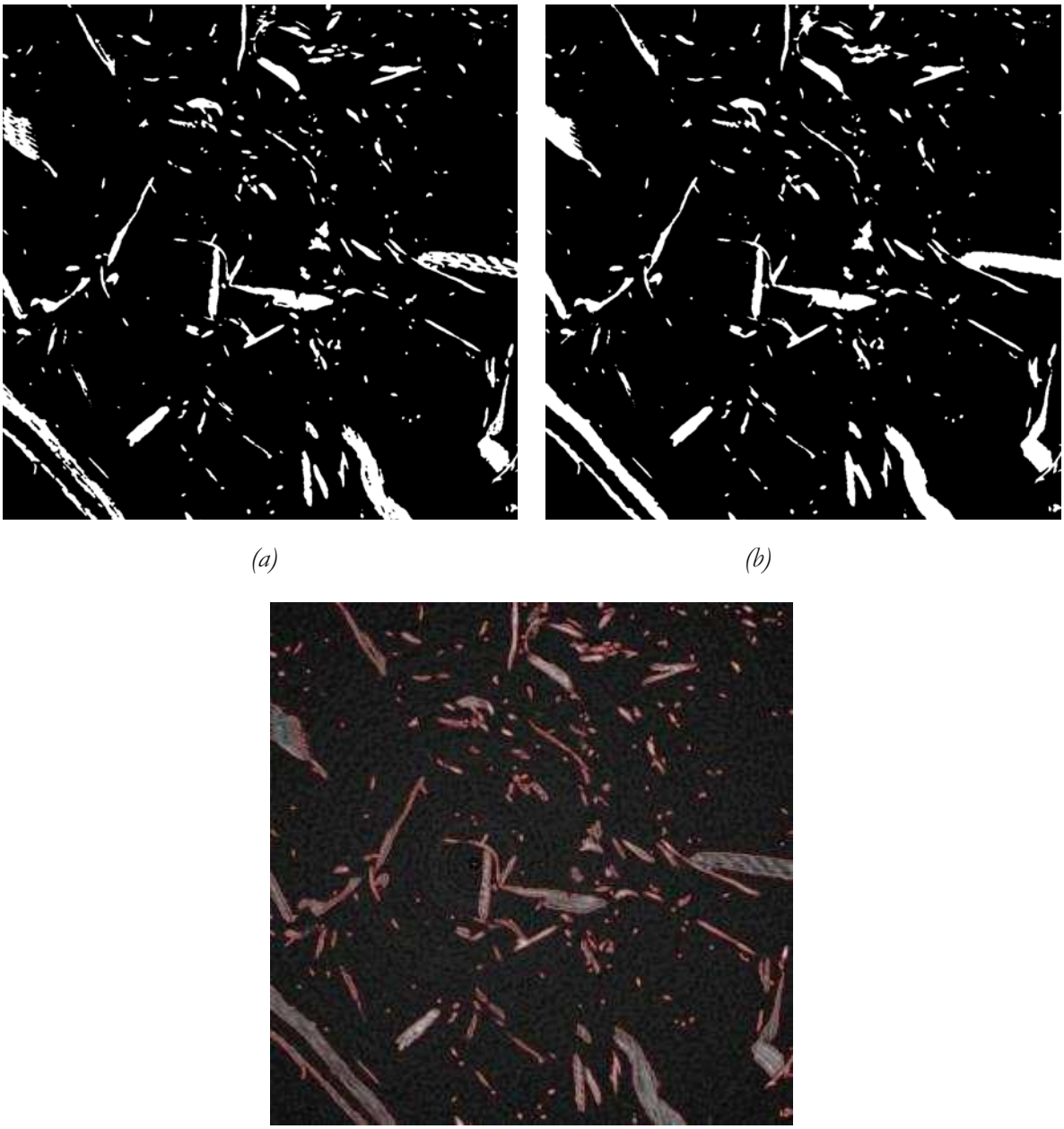

(a) *(b)*

(c)

Figure IV.7: Initial state - Slice 600 in (a) Thresholded image (b) Lumen-filled image (c) Superposition of grey-level image with lumen-filled image contour

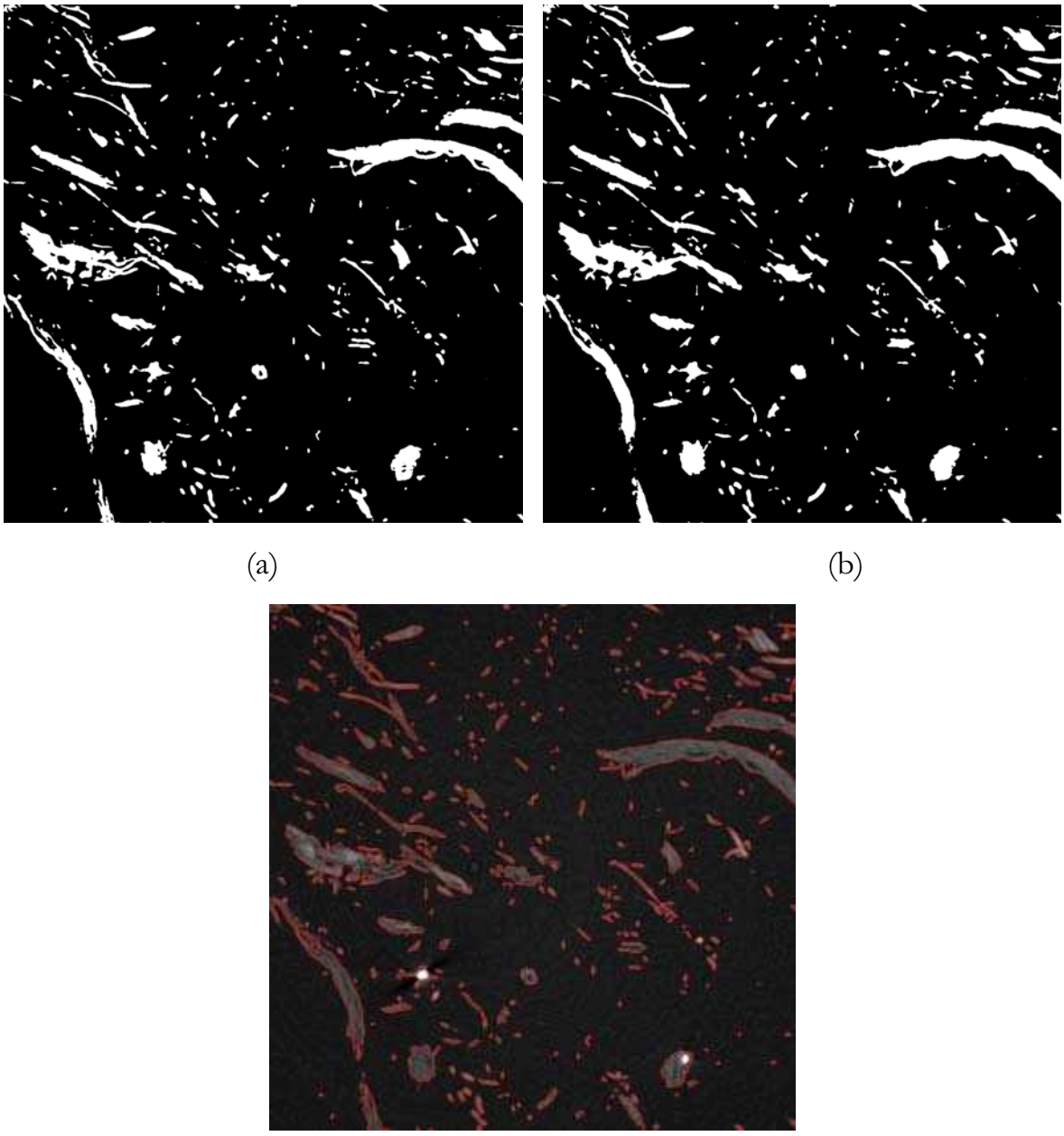

Figure IV.8: Initial state - Slice 800 in (a) Thresholded image (b) Lumen-filled image (c) Superposition of grey-level image with lumen-filled image contour

Applying the chosen thresholding value on lumen-filled images, we obtain the external porosity of the material for all compression states. The results are presented in Table IV.2.

Table IV.2: Summary of sub-volume extraction (Figure III.15)

Compression state	DVC thickness (voxels)	Morphological thickness (voxels)	Imposed compression rate (%) (Large deformation)	External porosity after lumen filling (%)
0	1450	908	0	92.3
1	1375	862	4.8	92.2
2	1305	818	9.5	91.8
3	1228	776	13.9	91.2
4	1155	737	18	90.7
5	1080	697	21.9	89.9
6	1010	660	25.5	89.6
7	933	619	28.6	88.7
8	859	574	32	87.5

IV.2.3 Segmentation of wood network from PES network

From tests at the IFTH, PES fiber diameters were found around 21.4µm with a standard deviation of ±1.8µm (Section II.1.2) but would this be the same after the elaboration process?

a) PES fibers after consolidation

After the thermal consolidation, while connecting through bonding, the diameters of the textile fibers appear to be larger than before consolidation. Considering a SEM image of the material (Figure IV.9), we can easily perceive some textile fibers whose contours are highlighted in red with a diameter measured of about 30-40µm, almost double PES fibers before consolidation, which may be due to fibers' physical and chemical properties and also to the mechanism of fiber fusion during the consolidation process. To the best knowledge of the author, there is no study on the modification of PES fiber section before and after the elaboration process. Nevertheless, knowing the PES diameter is necessary for the next operation of the wood/PES fiber segmentation, in order to understand the distribution of each fiber population on the material behavior. Put another way, the pre-determination of PES fibers is also a method to validate this segmentation.

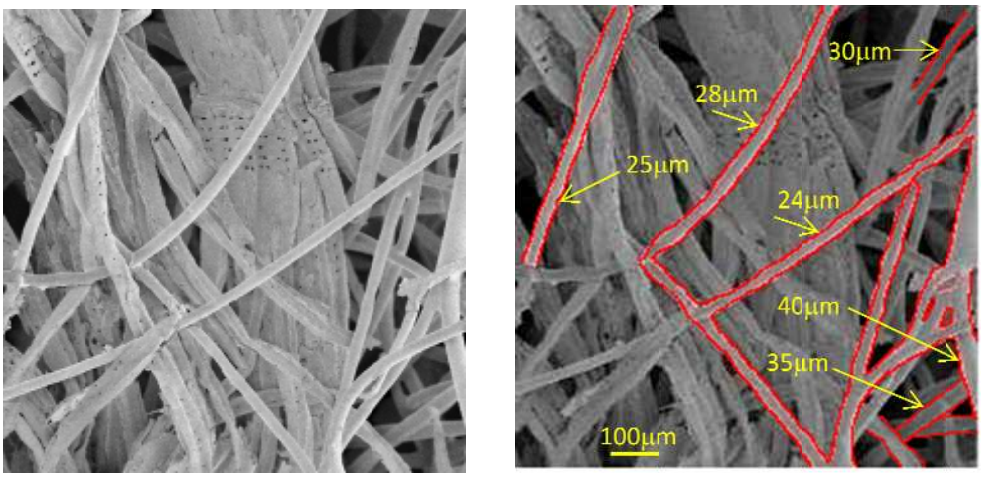

Figure IV.9 : Textile diameter after consolidation process-SEM image of wood-based fiberboard, I2M (size 940x940mm²)

Same PES diameters are observed on microtomographic images. Let's consider a 2D slice of 70x70 pixels which contains PES fibers (Figure IV.10). At each threshold value, the diameter of the fibers is measured through the longest distance in the same direction of two red pixels (assumed to belong to the PES fibers), giving a range of value from minimum (D_1) to maximum (D_2) (Table IV.3). There is no much difference between D_1 and D_2 between the chosen thresholding (with threshold value of 48-255) compared to other threshold operations. D_1 and D_2 are found to be about 30-40µm.

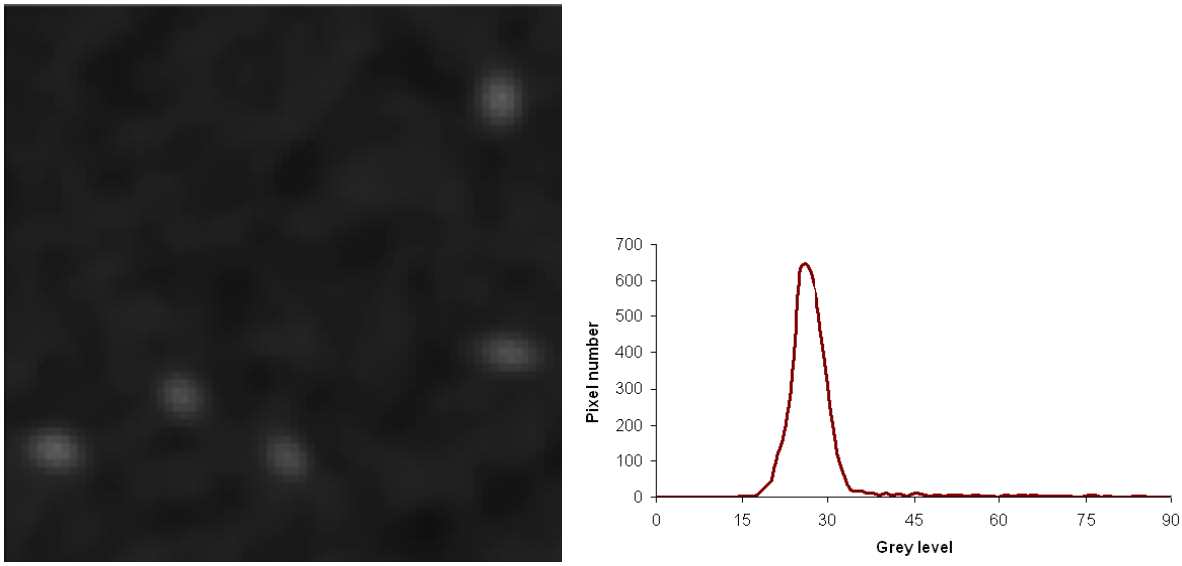

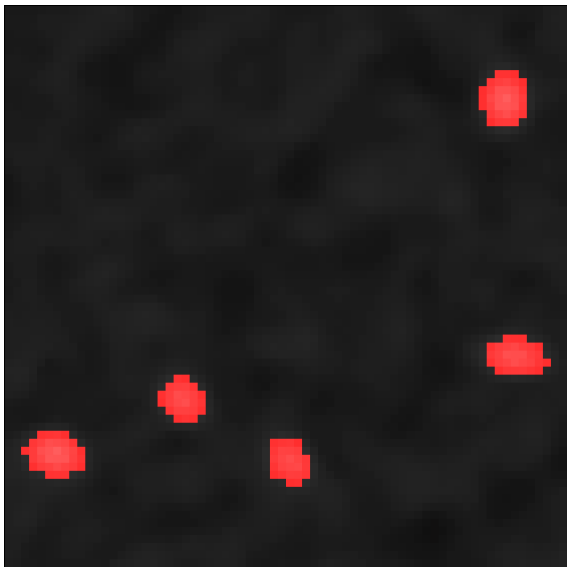

(Threshold 45-255)

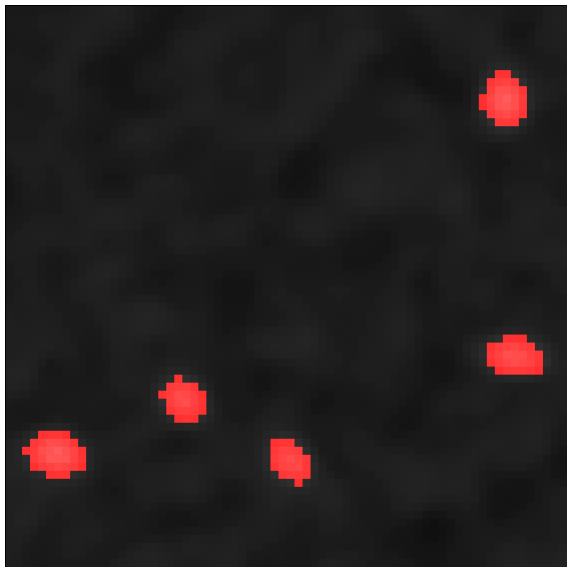

(Threshold 46-255)

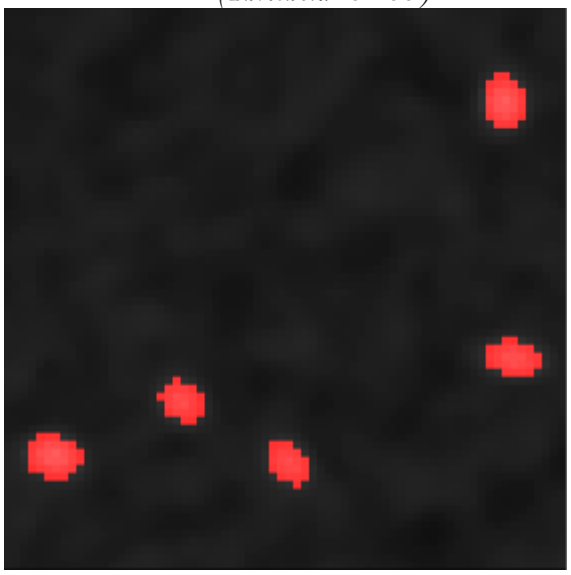

(Threshold 47-255)

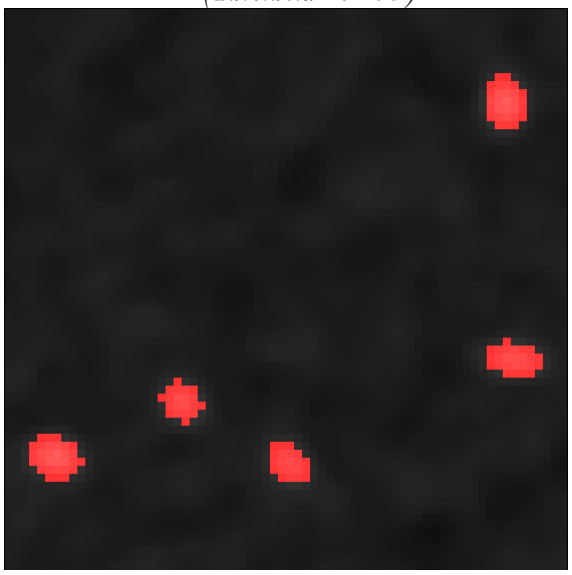

(Threshold 48-255)

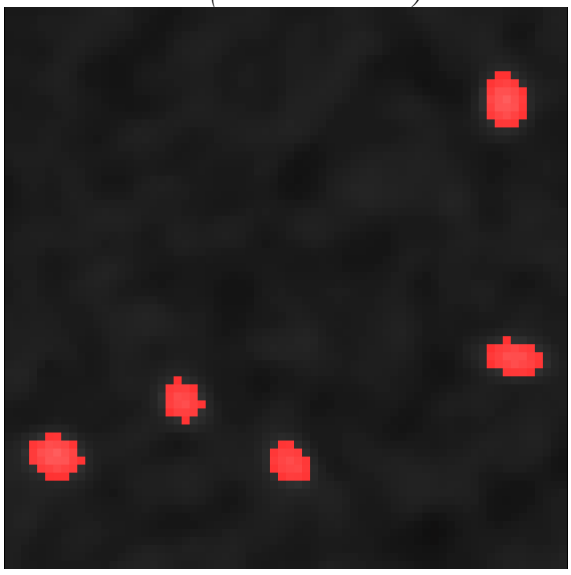

(Threshold 49-255)

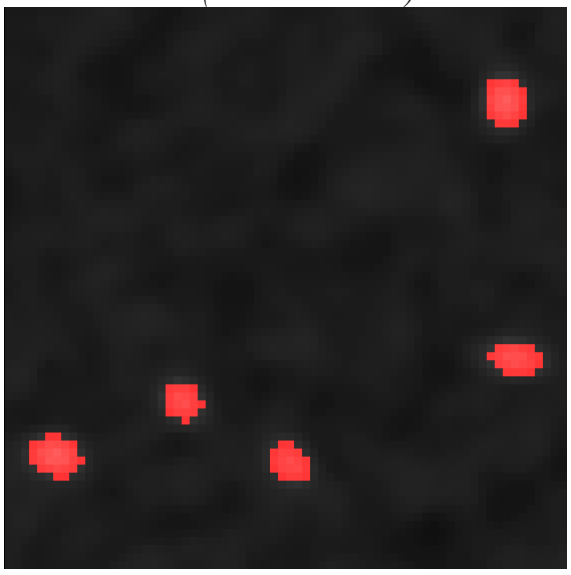

(Threshold 50-255)

Figure IV.10: Textile diameters obtained from CT-image at different threshold values and histogram of grey level image

Table IV.3: PES fiber diameters at different threshold values

Thresh Value	Fiber volume (pixels)	Fiber volume fraction (%)	Fiber diameter (pixel or µm)			
			D1 (pixel)	D2 (pixel)	D1 (µm)	D2 (µm)
45 - 255	152	3.1	6	8	36	48
46 - 255	141	2.88	6	7	36	42
47 - 255	132	2.69	6	7	36	42
48 - 255	**125**	**2.55**	**6**	**7**	**36**	**42**
49 - 255	122	2.49	5	7	30	42
50 - 255	115	2.35	5	7	30	42

b) Wood/PES fiber segmentation

Since there is no grey level contrast between wood and PES, the segmentation of the two different fiber populations is based on the diameters of PES fibers : the size of structuring element chosen for the segmentation operation is based on the maximum diameter of the PES fibers. This segmentation is a two-step procedure.

The first step, called "preliminary", consists of an opening of size equal to the maximum PES fiber diameter to segment PES fibers from wood fibers. The result of this opening is a wood network (wood image-1). A substraction of the wood image from the initial image results in the PES network (PES image 1) (Figure IV.11a). "Preliminary" comes from the fact that in order to prevent the most possible wood fibers entering the PES population, we used an adequate size of structuring element. However, during the consolidation, bondings are created with a larger size than the PES fibers so that it cannot be segmented with this chosen size (Figure IV.11). Plus the contour of fibers, especially of the wood fibers, is modified by the opening operation: the extraction took away a part of the wood surface into the PES image. We call them all false pieces.

The second step consists of repositioning these false pieces in their correct place. Since small wood fibers are excluded during the elaboration process while PES fibers are long and fused during the consolidation process, we may assume that the wood network exists by assembly of large wood pieces while the PES

network is a unique and connected object. Consequently, false pieces become non-connected objects of small sizes compared to either the whole wood or PES fiber network. Based on this principle, a multi-iteration size filtering of small objects in each population is performed in order to send these false pieces back to their positions (Figure IV.11b) until the volume of each population becomes idempotent (Figure IV.11c). The result of PES segmentation is illustrated in Figure IV.11. Figure IV.12 showing the 3D illustration of wood/PES network superposition where brown voxels are wood fibers.

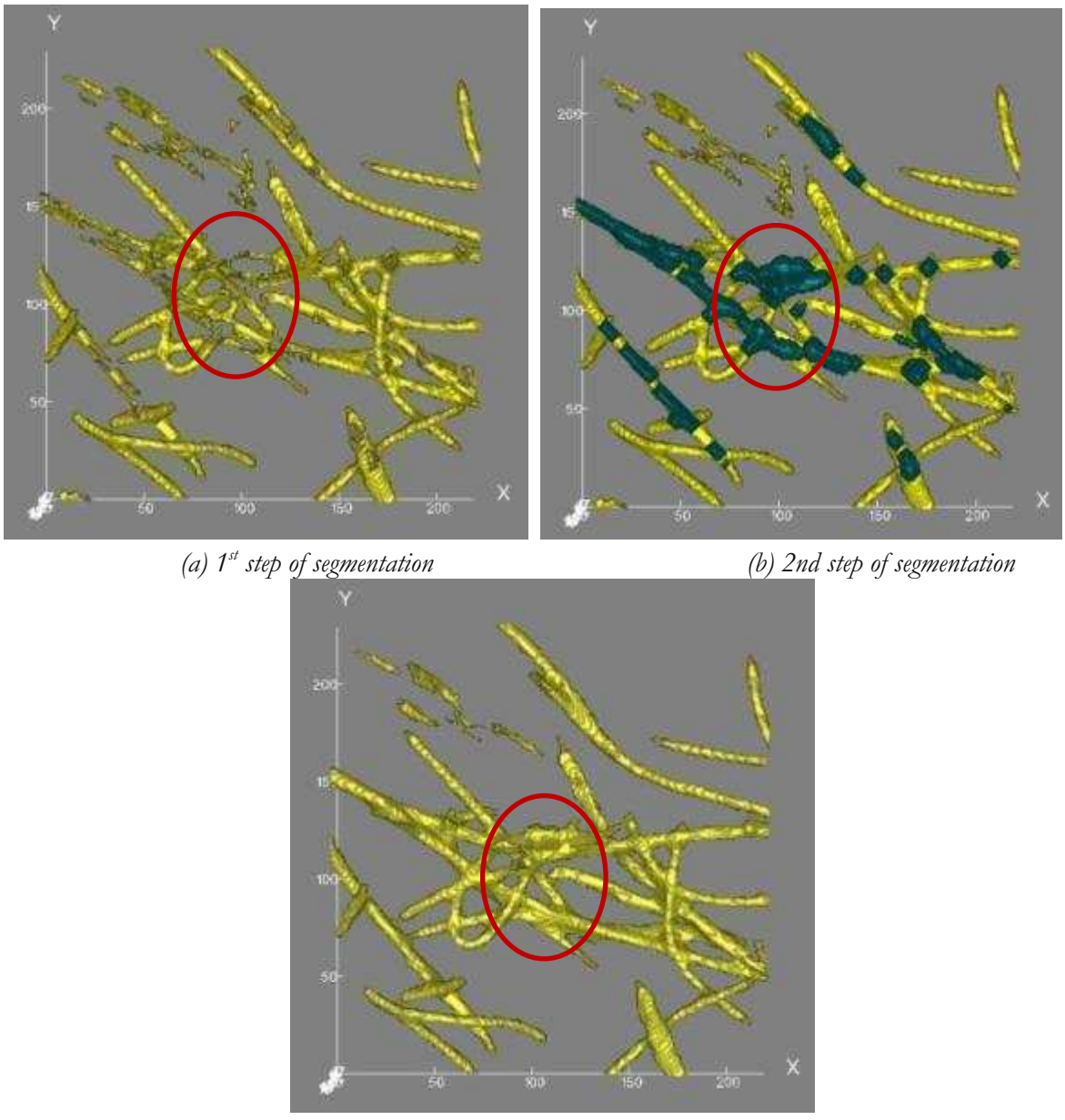

(a) 1st step of segmentation *(b) 2nd step of segmentation*

(c) Final pattern of PES fibers

Figure IV.11: 3D visualization of recovered textile liaisons after 2-step segmentation (Sub-volume of 220x230x20voxels)

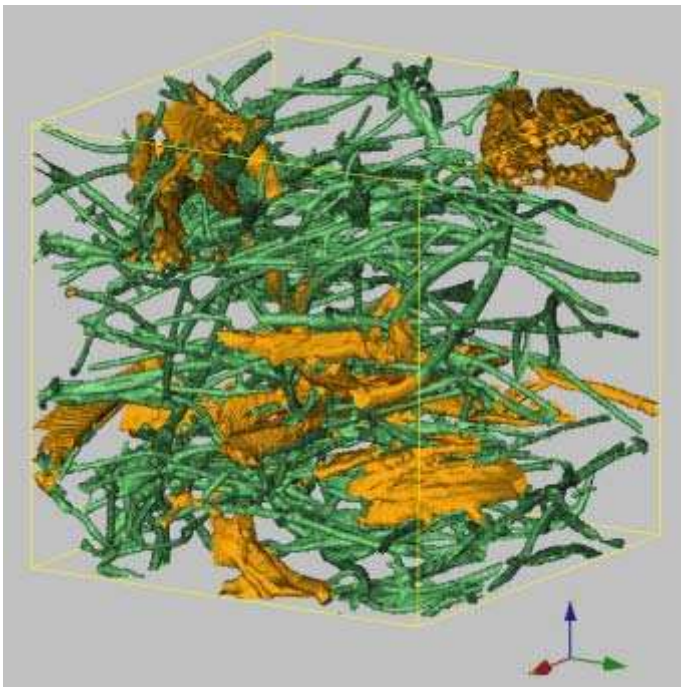

Figure IV.12: 3D visualization of Wood/ PES fiber segmentation

This segmentation allows us to observe the changes of each fiber population during compression as shown in Figure IV.13 and Figure IV.14: fibers have the tendency to vertically displace with small orientation changes, the transversal displacement seems to have to be ignored.

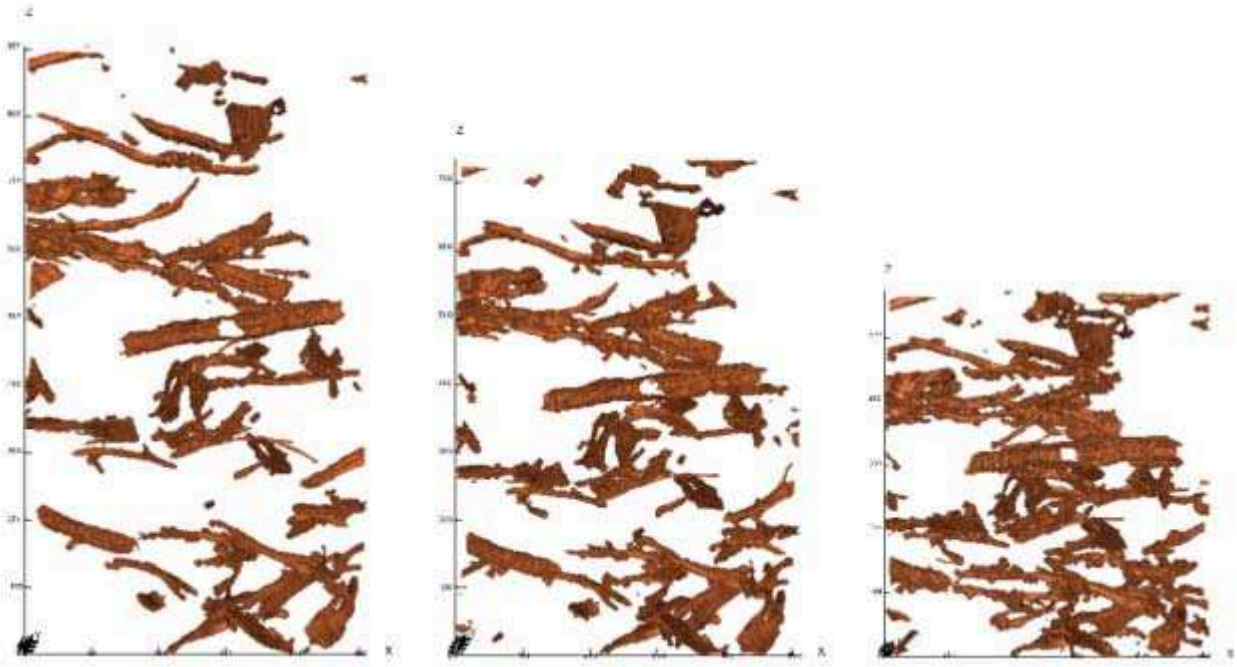

Figure IV.13: Wood fiber displacement (State 0%, 18.4% and 31.6%)

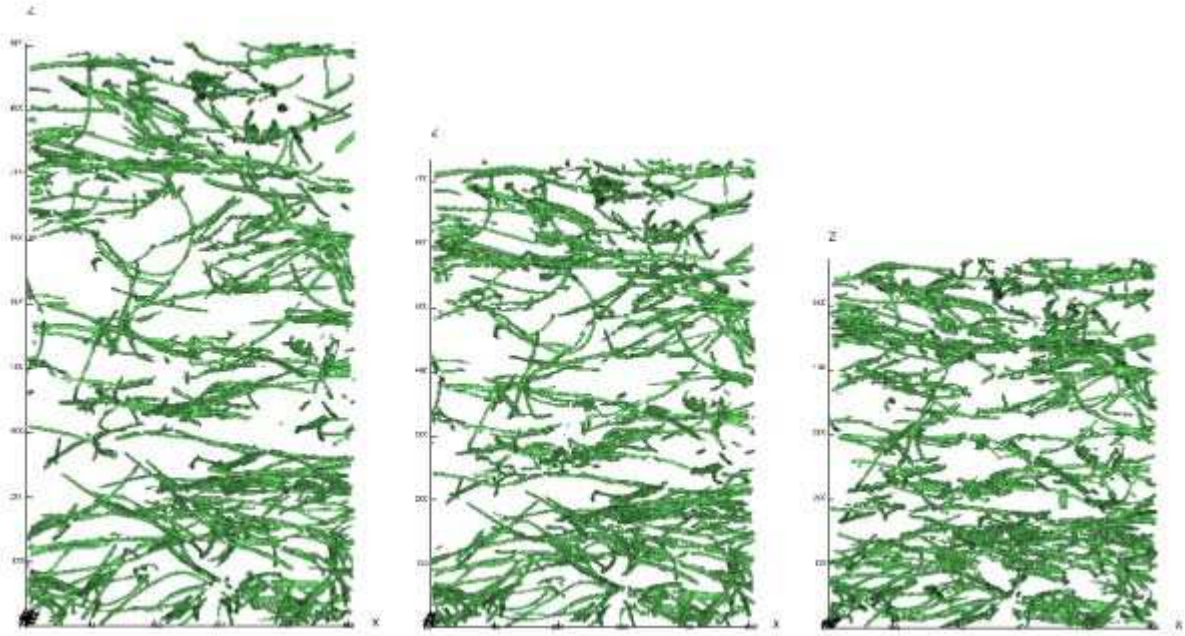

Figure IV.14: PES fiber displacement (State 0%, 18.4% and 31.6%)

At different compression states, the volume fraction of wood/PES fibers varies from 62-66% for wood fibers and 34-38% for PES fibers (Table IV.4), on average 63% wood and 37% PES. This ratio is quite close to analysis by a chemical technique but a little lower compared to 65% found in this study. This lower ratio may be due to no contrast difference between wood fibers and PES fibers, so that we cannot distinguish between these two fibers if they have the same diameters. A part of the wood fibers which is quite similar to PES fibers and connected to the PES assembly will be certainly segmented into the PES network. Consequently, the segmentation is not perfect: there are still some fibers which cannot be completely segmented (Figure IV.15) (blue voxels are wood fibers). The segmentation operation is still needed to be improved.

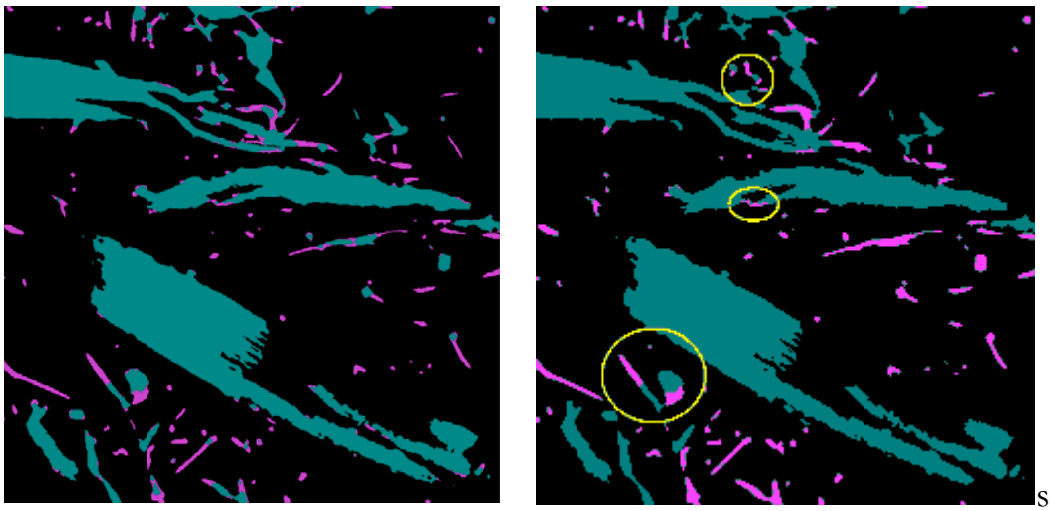

(c) *(d)*

Figure IV.15: 2D visualization of (a) 1st step Wood/PES segmentation (b) 2nd step Wood/PES segmentation

Table IV.4: Fiber volume fraction

Compression state (%) (Large deformation)	Size (voxels)	Fiber volume (voxels)	Wood fiber volume (voxels)	PES fiber volume (voxels)	Wood volume fraction (%)	PES volume fraction (%)
0	1024x1024x908	73415749	45441695	27974054	61.9	38.1
4.8	1024x1024x862	70303296	43351780	26951516	61.7	38.3
9.5	1024x1024x818	70120415	43367359	26753056	61.8	38.2
13.9	1024x1024x776	71333119	44890732	26442387	62.9	37.1
18	1024x1024x737	71818875	45355922	26462953	63.2	36.8
21.9	1024x1024x697	73841716	47711702	26130014	64.6	35.4
25.5	1024x1024x660	71671670	45760841	25910829	63.8	36.2
28.59	1024x1024x619	73433723	47658308	25775415	64.9	35.1
32	1024x1024x574	75023797	49638213	25385584	66.2	33.8

IV.3 Morphological measurements on the microstructure

In this section, we will present the principle of different morphological measurements on microstructure whose results will be presented in chapter VI.

IV.3.1 Size distribution using granulometry by opening

The size distribution of a set of fibers (or pores) is assessed by performing successive openings by an octahedron of growing size [80], [81]. It consists in measuring the volume fraction of the set which is smaller than the SE and gives global information on the diameter of the fibers and the pore sizes. The cumulated size distribution $G(X,\lambda)$ of a set X is defined by:

$$G(X,\lambda) = 1 - \frac{V(\gamma_{B_\lambda}(X))}{V(X)} \tag{4.18}$$

with B_λ the structuring element of size λ , $V(X)$ the measurement of the volume of the set X and γ_{B_λ} the opening by B_λ . The size distribution $g(\lambda)$ of set X can be obtained by the following expression:

$$g(\lambda) = G(X,\lambda) - G(X,\lambda-1) = \frac{V(\gamma_{B_{\lambda-1}}(X)) - V(\gamma_{B_\lambda}(X))}{V(X)} \tag{4.19}$$

Where $g(\lambda)$ also defines the weighted- volume of set X with diameter λ .

The mean diameter of a set X is then determined in function of the weighted-volume as

$$\overline{d} = 2a\sum_{\lambda=1}^{N} \lambda \times g(\lambda) \tag{4.20}$$

Hereby a=6µm is the resolution of microtomographic images and N is the maximum size of structuring element for the studied fiber population.

IV.3.2 Size distribution using local thickness method

Computation of local thickness is another method beside the granulometry by opening which allows us to determine the size distribution of the considered phase - the pore phase. While the granulometry by opening gives the global distribution of the pore sizes, the computation of the local thickness allows us to access the local distribution of the pore sizes in fibrous network space.

The theory of local thickness was first developed by Hildebrand and Rüergsegger [82] which was based on fitting maximal spheres to every point in the explored structure (Figure IV.16). Let's consider an arbitrary point p in set $\Omega \subset R^3$. The local thickness $\tau(p)$ is defined as the diameter of the largest sphere that containing p and totally included in Ω as

$$\tau(p) = 2 \times \max\{r / p \in sph(x,r) \subseteq \Omega, x \in \Omega\} \tag{4.21}$$

where $sph(x,r)$ is a sphere with center x and radius r.

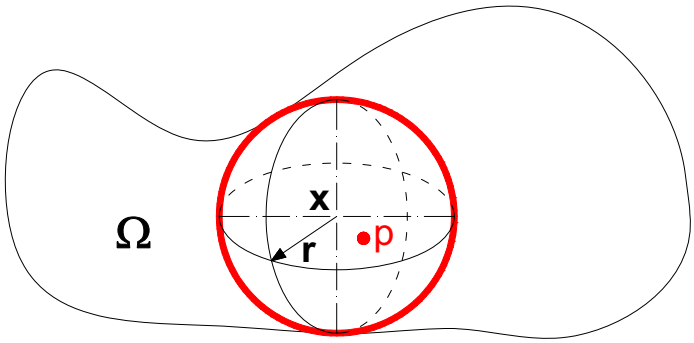

Figure IV.16: Local thickness by fitting maximal sphere to the structure [82]

The mean thickness of the structure is the arithmetic mean value of the local thicknesses taken over all points in the structure as

$$\bar{\tau} = \frac{1}{Vol(\Omega)} \iiint_{\Omega} \tau(d) d^3x \tag{4.22}$$

Where

$$Vol(\Omega) = \iiint_{\Omega} d^3x \tag{4.23}$$

The expression (4.24) is established for a continuous structure. However, since binary images are discretised, a distance map [39], [72] is used to determine local thickness. This procedure consists of two principal steps. Firstly, the distance map (D_{map}) is performed on every point p of the structure which assigns at this point the Euclidean distance of the nearest background point (other phase) from q. The sphere centered at p and having radius D_{map} is totally inside the considered structure as

$$D_{\max}(q) = \max\left(\{r > 0 / sph(q,r) \subseteq \Omega, q \in \Omega\}\right) \tag{4.24}$$

The local thickness can be determined through the distance map as

$$\tau(p) = 2 \times \max\left\{D_{map}(q), q \in X(p)\right\} \tag{4.25}$$

where $X(p)$ contains the center of all spheres with a radius equal to their corresponding distance and includes the point p as (Figure IV.17):

$$X(p) = \left\{x \in \Omega / \; p \in sph\left(x, D_{map}(X)\right)\right\} \tag{4.26}$$

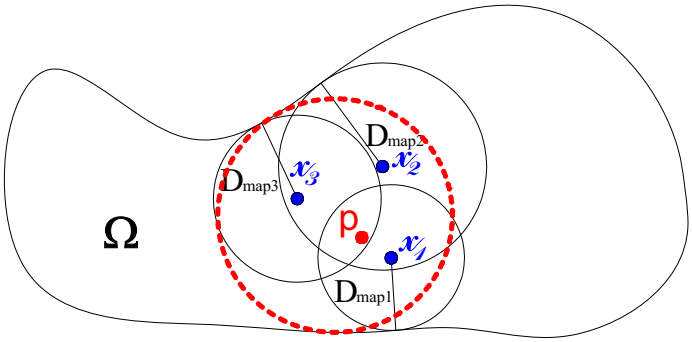

Figure IV.17: Local thickness by distance map

The second step consists of removing all redundant points q whose sphere $sph\left(q, D_{map}(q)\right)$ is included in other spheres of other points.

IV.3.3 Local orientation

The algorithm of the local orientation of each voxel in the image by erosion is proposed by J. Lux [61] for 3D characterization of morphology of wood-based fibrous materials. The local orientation $D_\lambda^\varepsilon(f)(p)$ of a point $p \in \Omega$ is the orientation α_i of the largest segment $L_{\lambda,\alpha}$ of length λ that is included in f and centered at p and defined as

$$D_\lambda^\varepsilon(f)(p) = \begin{cases} \alpha_i \text{ if } \varepsilon_{\lambda,\alpha_i}(f)(p) > \varepsilon_{\lambda,\alpha_j}(f)(p), \forall i \neq j \\ \varnothing \text{ otherwise} \end{cases} \quad (4.27)$$

where

p considered point for orientation determination

f image that contains point p

$\varepsilon_{\lambda,\alpha_i}(f)(p)$ grey level of the point p in eroded image of image f by segment $L_{\lambda,\alpha}$

Figure IV.18 presents the orientation of pixels of a 2D image where four orientations are tested.

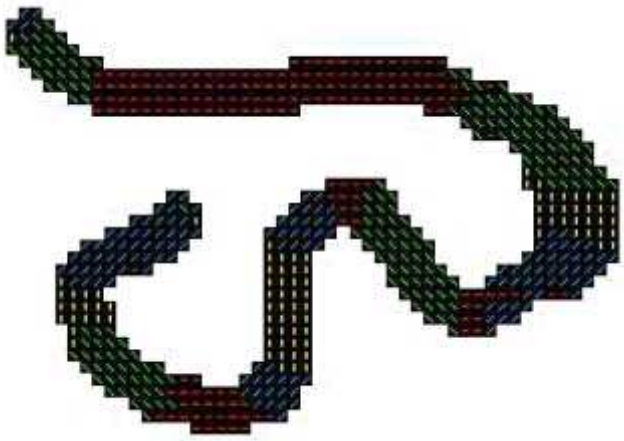

Figure IV.18: Local orientation field obtained by erosions [72]

Chapter V: Mechanical behavior at different scales

In this chapter, the mechanical responses under compressive solicitation at different scales are presented: the stress-strain relation at the macroscopic or the global scale, followed by the Young-modulus determination and the friction evaluation between the sample lateral and the confinement device; the 2D full strain field on the surface sample using DIC at the mesoscopic scale; and the 3D full strain field thanks to DVC at the microscopic scale.

The global response can be found as response of large sample (100x100x65mm) and small cylindrical sample (Ø9mm, H9mm) under classical compression tests as well as deduced from the relation of stress-imposed strain on whole sample thickness of the CT-test. Even though the size of the mesoscopic scale is about equal to the size of cylindrical samples but since at this scale, we begin to take into account the influence of the heterogeneity of the material (distribution of the fibrous/porous phase through the contrast difference of these phases on the sample surface). Therefore, the study by DIC on the sample surface at the chosen size of correlation domain is considered to be mesoscopic characterization.

As for the CT-test, an imposed strain step corresponding to 5% in small deformation (or engineering deformation) or to 4.9% in large deformation (or the Green-Lagrange deformation) case is carried out, which allows us to treat strain field in large deformation solution. In order to have the same base for comparison, experimental data at other scales (macroscopic and mesoscopic) are all converted into large deformation case, except for the experimental data of large sample in the following section V.1.1 since we would like to emphasize the relation between the maximum compression rate and the external porosity of the CT-test.

V.1 Global mechanical behavior

V.1.1 Classical test on large samples (I01 to I05)

a) Compression test until maximum consolidation (Sample I01)

Figure V.1 presents stress versus engineering strain curves of sample I01 in compression test until maximum consolidation where the stress increases slowly and quite linearly within 40% of strain level before quite suddenly increasing non-linearly and reaching the maximum strain level of 85% at 4200N of applied force. The maximum compression rate is almost equal to the total porosity of network (85% of engineering strain compared to 92% of external porosity). One may assume that because of the important volume of the pores, the applied force only

pushes these pores out of the material, which means that the size distribution of filled fibers is the same at the initial and the deformed states, showing no collapse phenomenon of fibers, especially wood fibers because of the existence of its lumens. The more pressure the fibers receive, the more the applied force increases. The transversal deformation is visibly observed even with the maximum compression state where the Poisson effect may be negligible.

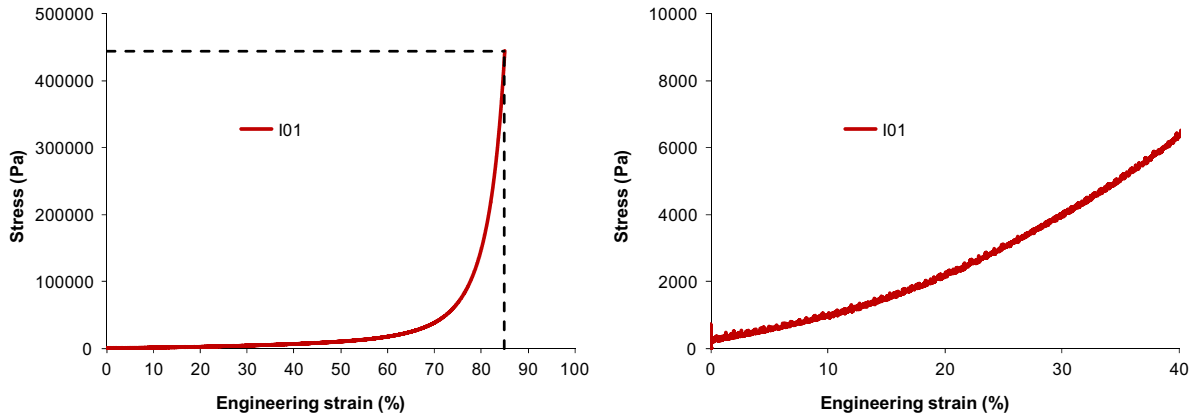

Figure V.1 : Stress-Strain curve of uniaxial compression test until maximum consolidation (sample I01, non-confined test)

In accordance to NF EN 826 [75], the Young's modulus is calculated in the elastic domain, using the stress-strain curve of small strain or engineering strain, whose maximum relative deformation is limited to 10% and minimum relative deformation (Figure V.2) corresponding to the inferior elastic limit as

$$E = \frac{\sigma_{10} - \sigma_e}{\varepsilon_{10} - \varepsilon_e} \tag{5.1}$$

where

σ_{10}, σ_e stress at 10% of relative deformation and at inferior limit of elastic zone

$\varepsilon_{10} > 0$ equal to 10% of relative deformation

$\varepsilon_e > 0$ equal to inferior limit deformation of elastic zone

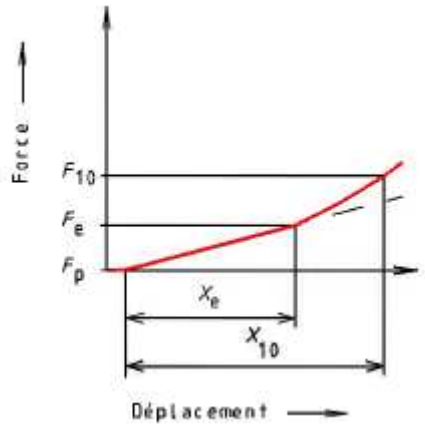

Figure V.2: Elastic zone for Young's modulus determination [75]

In Figure V.2, X_{10} is the small deformation of 10%, X_e is the deformation corresponding to the inferior limit of the elastic zone, F_{10} is the applied load corresponding to 10% of small deformation and F_e is the applied load corresponding to the inferior limit of elastic deformation X_e.

However, as the stress-strain curve is not smooth, we propose to determine the Young's modulus value by regression of the elastic zone between 5% and 10%. The Young's modulus for the large sample is finally found to be of 8400Pa in the case of the sample I01.

b) Cyclic tests (samples I04 and I05)

Cyclic tests are carried out on the confined sample (I04) and the non-confined sample (I05). Figure V.3 gathers all force versus Green Lagrange strain rate curves in cyclic uniaxial compression tests of I04. The residual strain and hysteresis were detected for all cycles, most likely due to the irrecoverable rearrangement, slippage at fiber contacts and the friction between fibers [19], [25], [30]. Under each compression state, although the curves change from loading, unloading and reloading, they become stable after the first loading curve which may be explained by the influence of the compression machine on the first loading and this influence is then self-adjusted for successive cycles. However, the hysteresis increases and depends on the maximum load reached (Figure V.3, Figure V.4) and it shows clearly that the macroscopic behavior depends on the evolution of the material morphology [30].

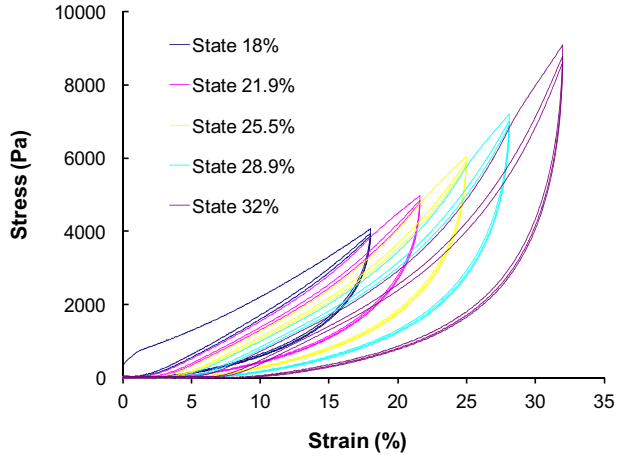

Figure V.3: Stress-strain curve of confined cyclic test (I04)

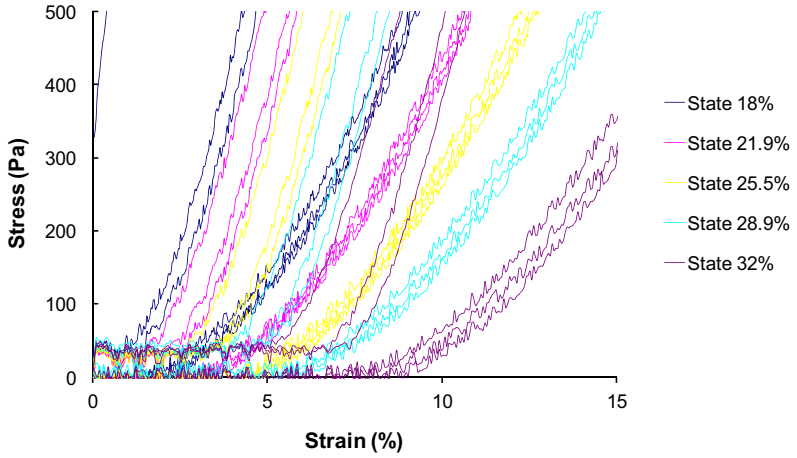

(a)

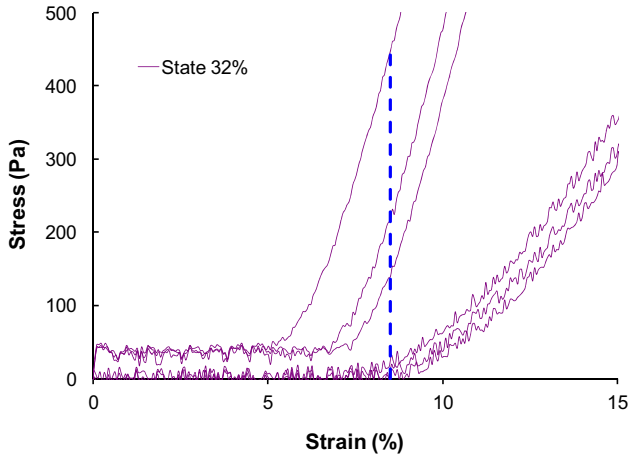

(b)

Figure V.4: Starting point of confined cyclic test (I04) without modification (a) for all cycles (b) for only three cycles of state 32%

However, we notice that the residual strain illustrated in Figure V.4 does not account for the fact that: when the movable plate releases the sample surface, the sample surface still moves but with a slower velocity compared to the velocity of the movable plate. As the displacement transducer cannot detect this displacement of the sample surface, the residual strain measured in Figure V.4 is not correct (i.e. left zone of dash blue line in Figure V.4b). The sample strain is only correct when it overcomes this residual deformation. We propose to move all loading-unloading curves so that the loading curves begin when the movable plate touches the sample surface. However, we must also redefine the initial thickness of the sample: whether we will still keep the initial thickness of the sample before testing or use the sample thickness when the movable plate touches the sample surface as the initial thickness. As we cannot decide, two methods of modification are proposed whose results are illustrated in Figure V.6 and Figure V.7:

- 1st modification method: Reserve the virgin material thickness as the initial thickness (L_0) for all loading or unloading cases. However, the displacement of the material is only counted when the movable device (Teflon surface) touches the sample surface (Figure V.5b).

- 2nd modification method: The material thickness after each unloading case becomes the initial thickness (L'_0) for the next loading or reloading. The displacement of the material, identically with the previous method, is only counted when the movable device (Teflon surface) touches the sample surface. However, the beginning moment of each reloading is chosen manually.

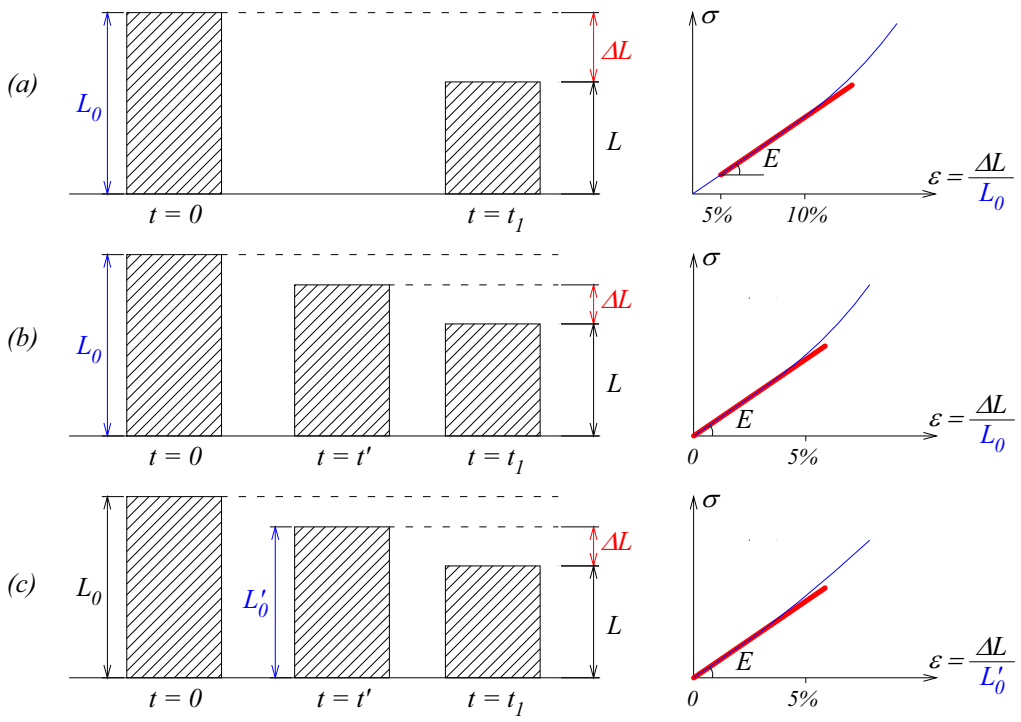

Figure V.5: Definition of initial thickness (a) before modification (b) 1st modification type (c) 2nd modification type

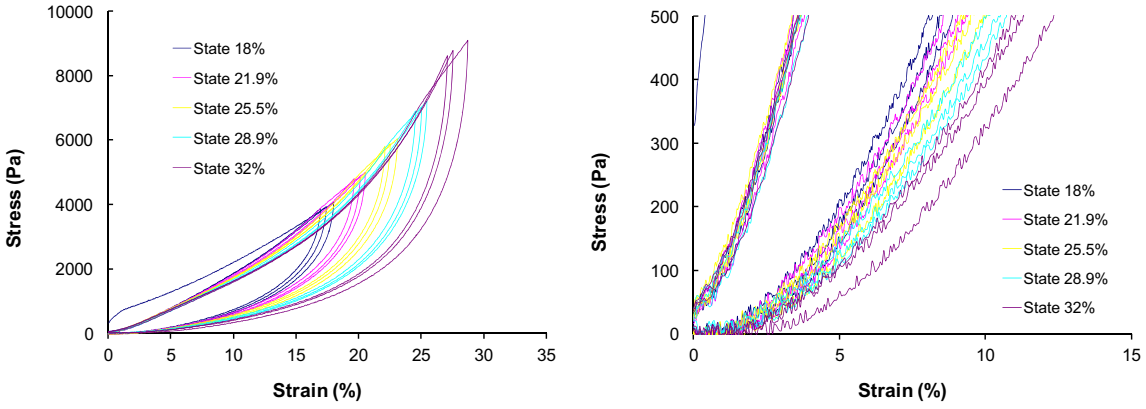

Figure V.6: Stress-strain curve of confined cyclic test (I04) with 1st modification method: L_0 is conserved as the reference initial thickness

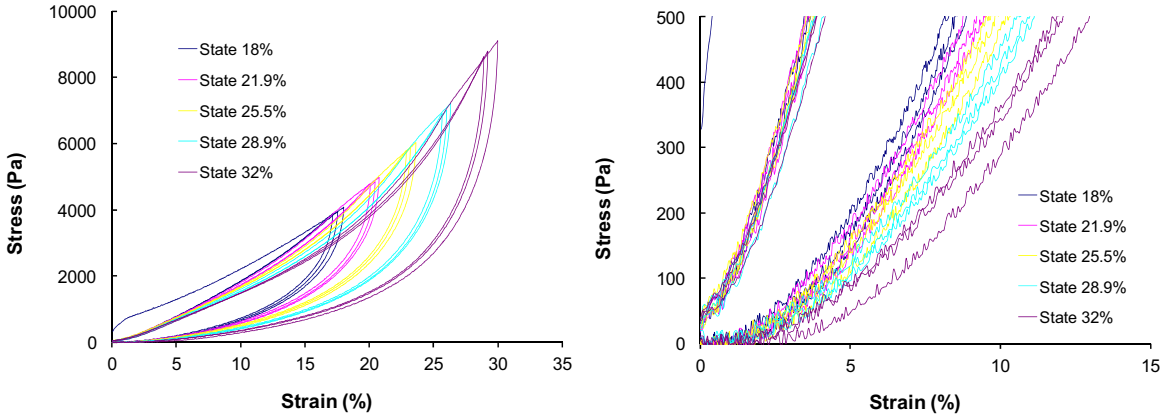

Figure V.7: Stress-strain curve of confined cyclic test (I04) with 2nd modification method: a new initial thickness L'_0 is defined at each compression state

The calculation of the Young's modulus in three cases (a) before modification (b) 1st modification method and (c) 2nd modification method of all loading curves of the sample I04 is summerized in Table V.1. There is no difference between the 1st modification method compared to before modification and the values obtained from the 2nd modification method are slightly smaller than those of the 1st modification method. The diminution rate of Young's modulus value between two consecutive cycles decreases as shown in Figure V.8 and Figure V.9. Moreover, considering two consecutive compression rates, Young's modulus value of the third cycle in the previous rate is found to be similar to that of the first cycle of the next rate, showing that for a given compression rate, the sample behavior will become convergent after certain cycles. Therefore, 3 cycles per compression rate is enough to investigate the behavior of the material under cyclic tests.

The same procedure is applied to sample I05 in unconfined test; values of Young's modulus for this sample are presented in Table V.2.

Table V.1: Young's modulus derived from confined cyclic test (sample I04)

Compression rate (%)	Young's modulus before modification (Pa)			Young's modulus obtained from 1st modification method (Pa)			Young's modulus obtained from 2rd modification method (Pa)		
	1st cycle	2nd cycle	3rd cycle	1st cycle	2nd cycle	3rd cycle	1st cycle	2nd cycle	3rd cycle
18	16800	20100	19600	16800	20100	19600	16800	20000	19400
21.9	19200	18600	18200	19200	18600	18200	19000	18300	17800
25.5	18000	17600	17400	18000	17600	17400	17500	17000	16700
28.9	17200	16800	16500	17200	16800	16500	16400	16100	15600
32	16400	16100	16000	16400	16100	16000	15500	15000	14700

Table V.2: Young's modulus derived from unconfined cyclic test (sample I04)

Compression rate (%)	Young's modulus before modification (Pa)			Young's modulus obtained from 1st modification method (Pa)			Young's modulus obtained from 2rd modification method (Pa)		
	1st cycle	2nd cycle	3rd cycle	1st cycle	2nd cycle	3rd cycle	1st cycle	2nd cycle	3rd cycle
18	23100	21100	20400	23100	21100	20400	23100	21100	20400
21.9	20200	18700	18100	20200	18700	18100	20200	18600	18100
25.5	17600	17200	16800	17600	17200	16800	17600	17000	16700
28.9	16600	15400	14900	16600	15400	14900	16400	15200	14700

The results in Table V.1 and Table V.2 are graphically illustrated in Figure V.8 and Figure V.9 which show the evolution of Young's modulus of the loading path of three cycles per compression state for the confined test (sample I04) and the non-confined test (I05). Except for the low value of the first cycle at 18% of compression state which is due to the prestressing effect, the same evolution may be observed in different compression states: the Young's modulus has the tendency to decrease at higher compression rates and at higher compression cycles.

Physically, it reflects that the rigidity of the whole sample falls off, but it also shows clearly that hysteresis is accumulated not only from one cycle to another but always exists even during the loading path. In other words, the deformation of the sample during the loading path is summed up by the pure deformation in a simple compression which has only one loading procedure with the residual deformation of the material in the unloading path. In this behavior, microstructure modifications play an important role: the more compressed the material is, the more contacts between fibers are established which will create more rigid microstructures that are harder to deform under the same applied load but the harder the recovery is. Moreover, these changes are accumulated from one cycle to the others. Consequently, we obtain a high deformation at the same applied load which gives the diminution of Young's modulus values.

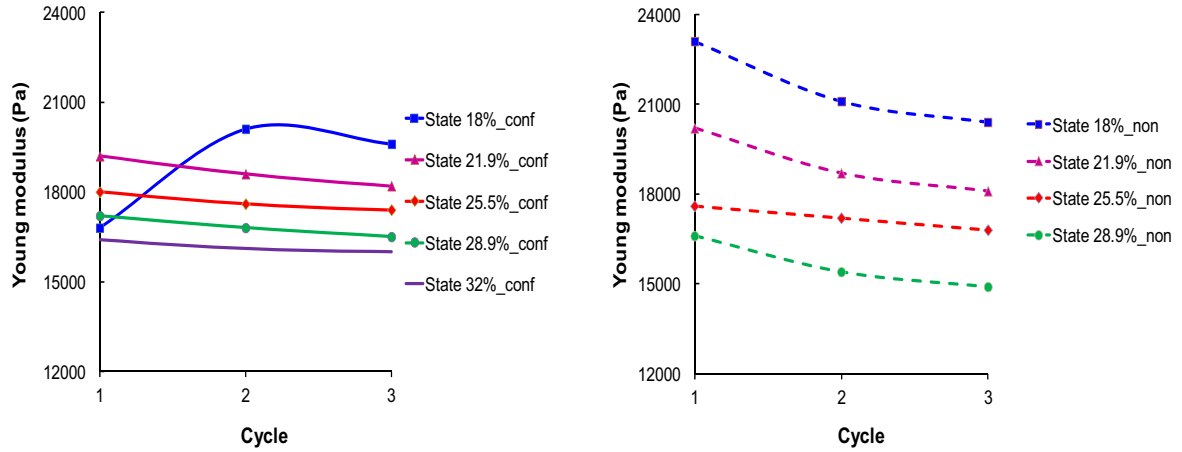

(a) *(b)*

Figure V.8: Evolution of Young's modulus during cyclic test using 1st modification method in (a) confined test (b) non-confined test

Same results are observed for the second modification method shown in Figure V.9.

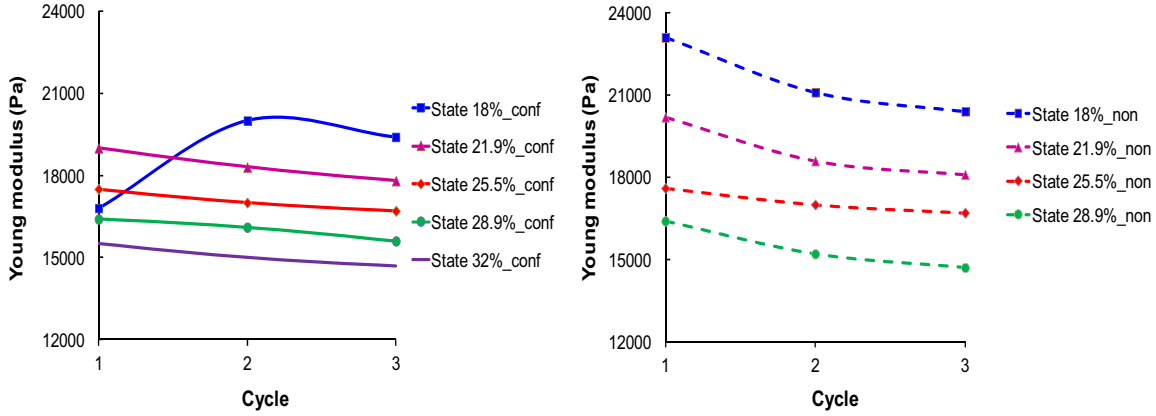

(a) *(b)*

Figure V.9: Evolution of Young's modulus during cyclic test using 2nd modification method in (a) confined test (b) non-confined test

Figure V.10 and Figure V.11 illustrate the comparison of Young's modulus evolution of the confined and the non-confined tests in two modification types. The diminution rate of Young's modulus in case of the non-confined test is quicker compared to that of the confined test which may be due to the friction effect between the lateral surfaces of the sample with the confinement device. However, we do not have a clear explanation for this phenomenon because we expected a contrary result.

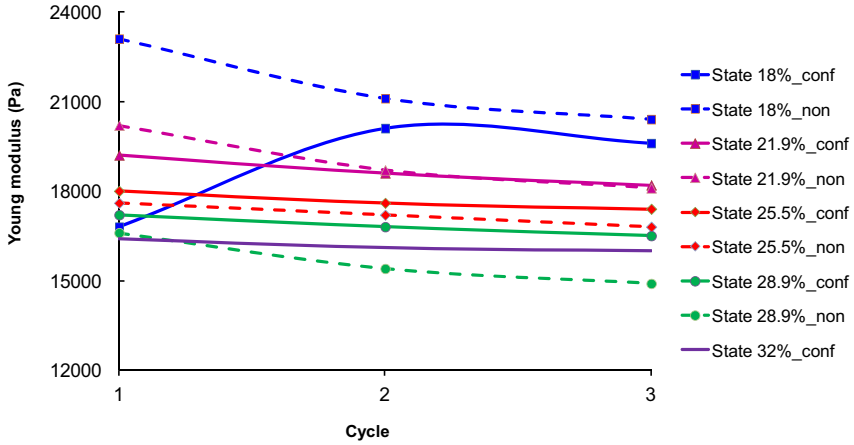

Figure V.10: Comparison of Young's modulus during cyclic test in 1st modification

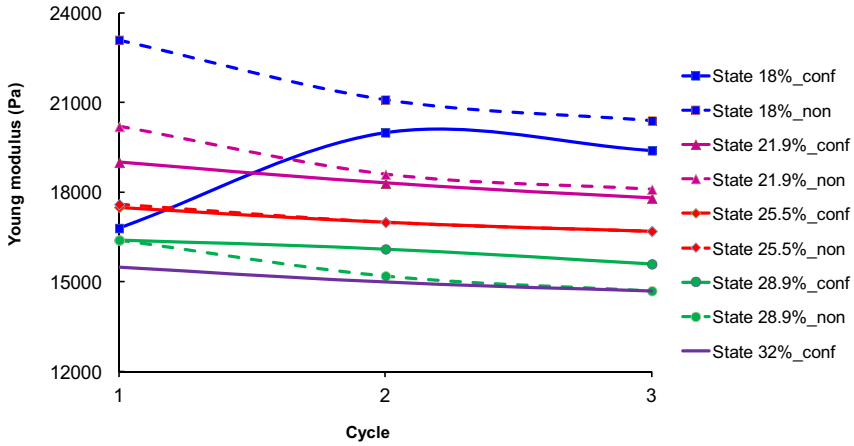

Figure V.11: Comparison of Young's modulus during cyclic test in 2nd modification

V.1.2 Compression test on small cylindrical samples (IC01 to IC12)

Figure V.12 collects stress versus Green Lagrange strain curves of compression tests on small cylindrical samples at different compression rates which are added by the one of test on the large sample I01. We can see that the shapes of all the curves are globally comparable and similar. The curve of the large sample is closer to those at 46% of compression rate (corresponding to 70% of engineering strain). A slight discrepancy is observed at small deformation and the discrepancy is clearer at higher strain between samples which may come from the intrinsic characteristics of material and slight sample differences during preparation (in height and density). The fiber loss at sample surface during the preparation of the specimen also influences the sample behavior. This again confirms that at small deformation, because of the high porosity, the changes in fibers configuration do not much affect the sample response, but it is not the case at higher strain.

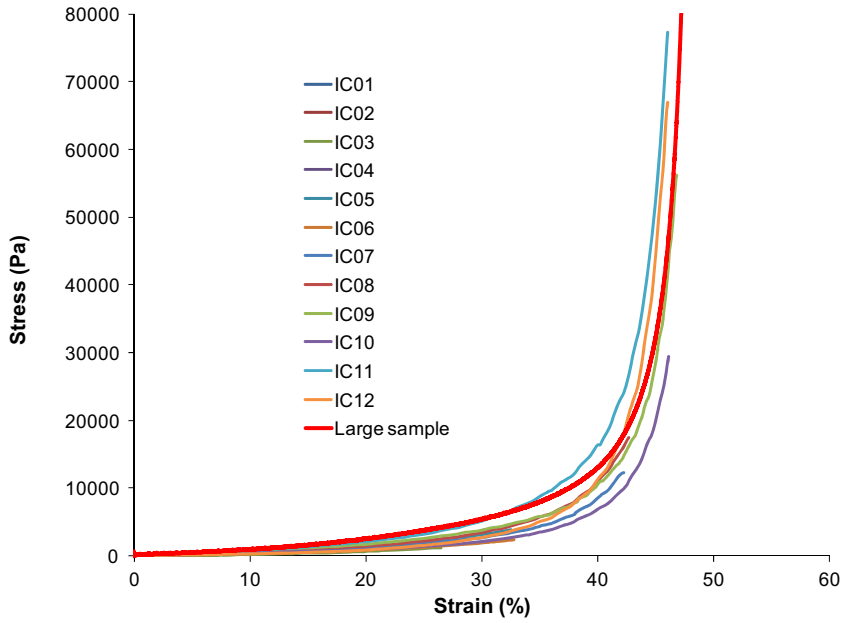

Figure V.12: Stress-Strain curves of small cylindrical sample compared to large sample I01

Young's modulus varies between 2600Pa and 7600Pa with a mean value of 4600Pa and standard deviation of 1500Pa which is smaller compared to 8400Pa of the large sample as observed in Figure V.1.

V.1.3 Global behavior deduced from imposed deformation in microtomography test

Table V.3 resumes eight compression states in the CT-test, followed by Figure V.13 presenting the global mechanical response deduced from imposed deformation in the CT-test which refers to stress versus Green Lagrange strain relation where the stress is determined from the load intensity on the sample surface and the imposed vertical strains are evaluated from values of displacement imposed by the actuator. The sample section is assumed to be constant because of the confinement device. The evolution of the stress according to the vertical strain is not linear: stress increases much more than imposed strain showing the rigidifying effect.

Table V.3: Ezz strain at different compression state

Compression state	Imposed Ezz strain (%)
0	0.0
1	4.9
2	9.2
3	13.7
4	17.7
5	21.6
6	25.0
7	28.5
8	31.6

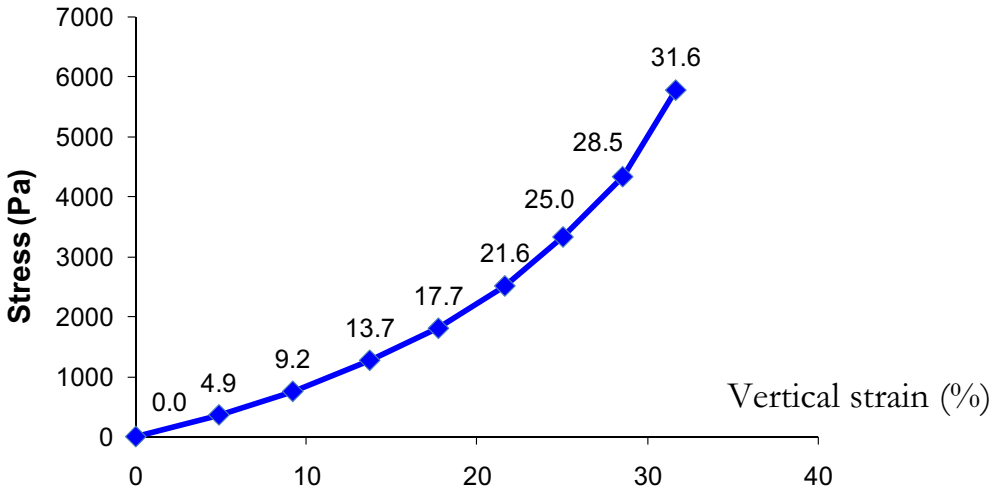

Figure V.13: Imposed vertical strain on sample of the CT-test

We can observe a perfect superposition of the behavior between the CT-test and the test on the large sample (Figure V.14). The Young's modulus derived from the CT-test is also 8400N. As mentioned before, the material behavior of small cylindrical samples may differ from one to other due to the intrinsic properties of the material and to the difficulties in sample preparation.

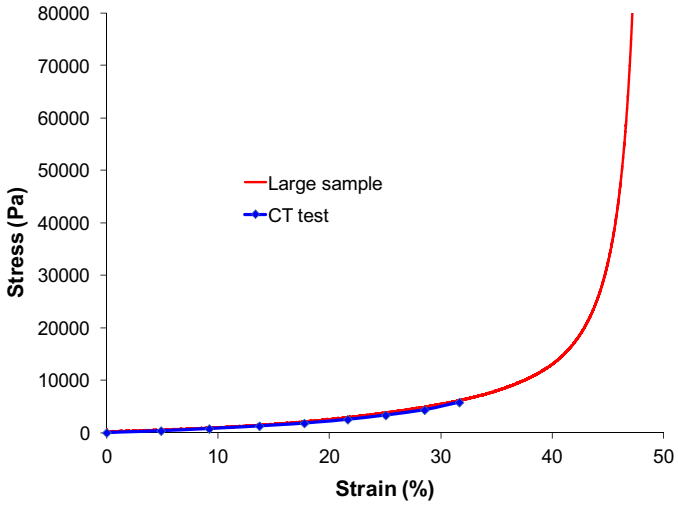

Figure V.14: Comparison between compression test on large sample and CT-test

A good superposition of two stress-strain curves shown in Figure V.14 demonstrates that the chosen sample size for the CT-test is equal or superior to the size of the mechanical representative elementary volume of the material.

V.1.4 Fitting to experimental mechanical laws without taking into account the microstructure

In order to identify experimental laws, we plot the stress-strain curve of the CT-test and the test on the large sample compared to different constitutive laws. According to Van Wyk's Eq. (1.17), the stress is related to the strain following an exponent law. We notice that curves in Figure V.15 fit well to Van Wyk's model at higher strain with a = 1500Pa and b = -3.

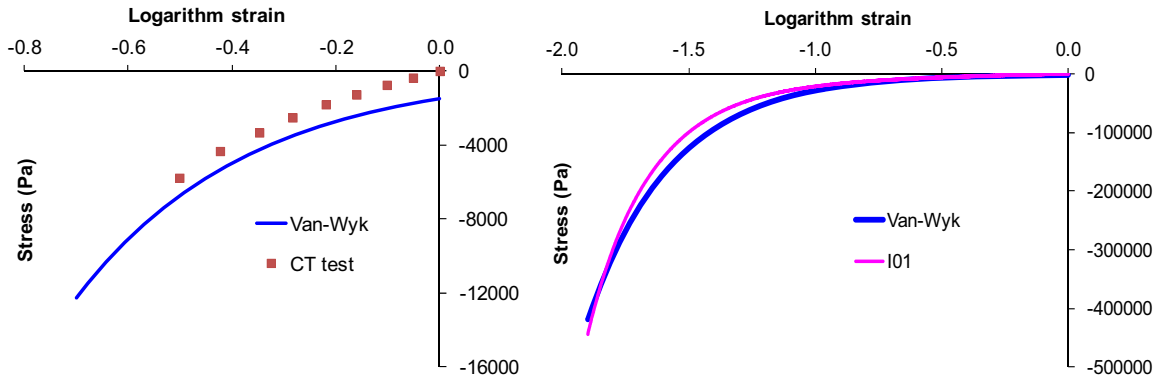

Figure V.15: Fit of global behavior to Van Wyk' model: case of the CT-test and test on large sample I01

According to Baudequin's experimental model in Eq. (1.22), the force is proportional to the strain difference $\left(\varepsilon^{*}-\varepsilon\right)^{-\frac{3}{2}}$ in the case of small strain or

$2.83\left(\left(1-e\right)^2-\left(1-e^*\right)\right)^{-1.5}$ in the case of Green-Lagrange strain. Using $e^* = 0.489$ which corresponds to the maximum strain of compression test on the large sample, and applying appropriate proportional coefficient (0.2 for the CT-test and 5 for large sample), the fitting results are shown in Figure V.16.

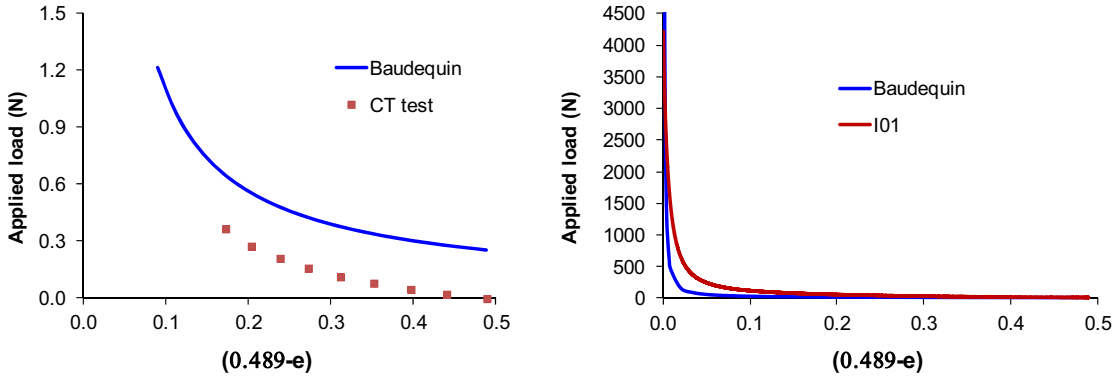

Figure V.16: Fit of global behavior to Baudequin model

Figure V.15 and Figure V.16 show that the behavior of the material fits Van-Wyk's model better than Baudequin's.

V.2 Mesoscopic response by 2D image correlation

V.2.1 Digital image correlation (sample P02)

a) Size choice of the correlation domain and of the correlation zone

The optimal size of the correlation domain and the correlation zone depends strongly not only on material surface pattern but also on the chosen resolution in the compression test. In order to investigate the influence of the size of correlation domain and correlation zone on DIC performance (Figure V.17), one zone of interest (ZOI) or correlation zone which is centered at one point in the center of the sample surface is chosen. This choice of ZOI is to avoid the edge effects. The studied ZOI is defined by the center point and four predetermined tops. During the DIC performance, the displacement of four tops allows us to obtain the deformation of the studied zone which is assumed to be homogeneous. The measurement precision of strain field obtained by DIC is proportional to the precision of displacement determination of four correlation domains and is inversely proportional to the size of ZOI. The larger the ZOI size, the more accurate the obtained local strain; however, local variations may be ignored since the strain is assumed to be homogeneous all over the ZOI. The objective of this study is not to find the precision of DIC measurement but to determine optimal

parameters of DIC in order to obtain a correct strain field on the studied material. Moreover, we would like to evaluate the performance of DIC on a heterogeneous and fibrous material. These objectives are carried out by determining the minimum ZOI size to avoid average effect and to determine the corresponding size of the correlation domain. The ZOI size, domain size, and computation base can be controlled by the operator before computation. The selection of the appropriate combination of the three parameters depends on the purpose of the study.

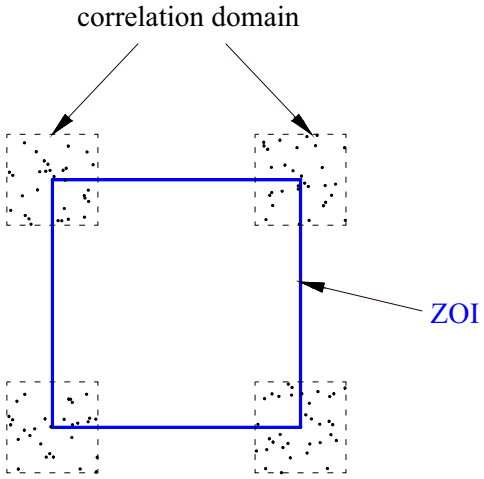

Figure V.17: DIC employed for one zone centered at the same point

In order to obtain the minimum ZOI size, the deformation of ZOI is studied in different types of correlation: (1) *domain 8/zone 8* corresponding to the chosen size of correlation domain of 8pixels and the size of correlation zone is 8pixels or the distance between centers of correlation domains is 8pixels, respectively (2) *domain 16/zone 16,* (3) *domain 32/zone 32,* (4) *domain 64/zone 64,* (5) *domain 32/zone 64,* (6) *domain 128/zone 128,* (7) *domain 64/zone 128,* (8) *domain 32/zone 128*. In the case of 2D strain field, four deformation types are investigated: DefXX (transversal deformation, which illustrates the influence of Poisson coefficient), DefYY (longitudinal deformation or deformation in loading direction), Def1 and Def2 (principal deformations and Def1> Def2). However, in order to validate the size of the correlation domain and of the correlation zone, it is enough to use DefYY and Def1. Figure V.18 presents DefYY and Def1 obtained with different correlation types at different imposed compression rates. It shows that the deformation of the studied zone becomes independent of the size of the correlation domain and the correlation zone when the correlation zone is larger than 64pixels or 4mm.

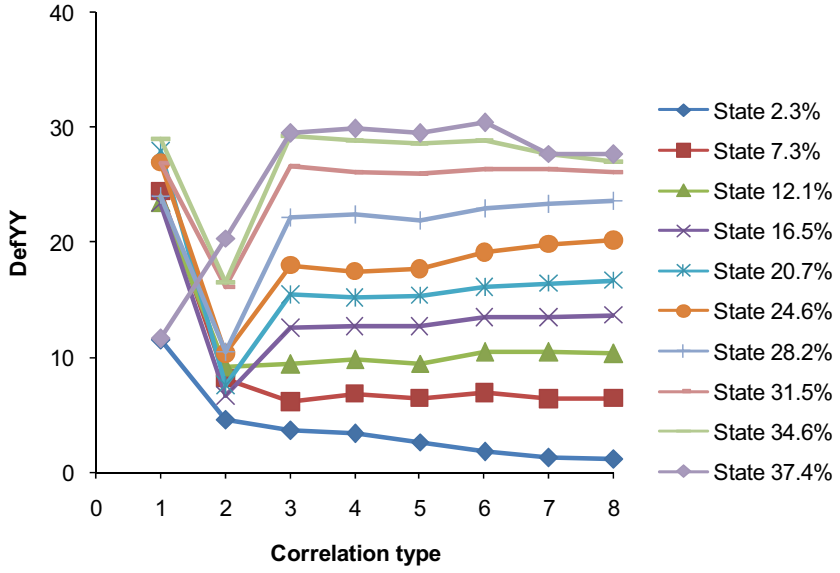

(a)

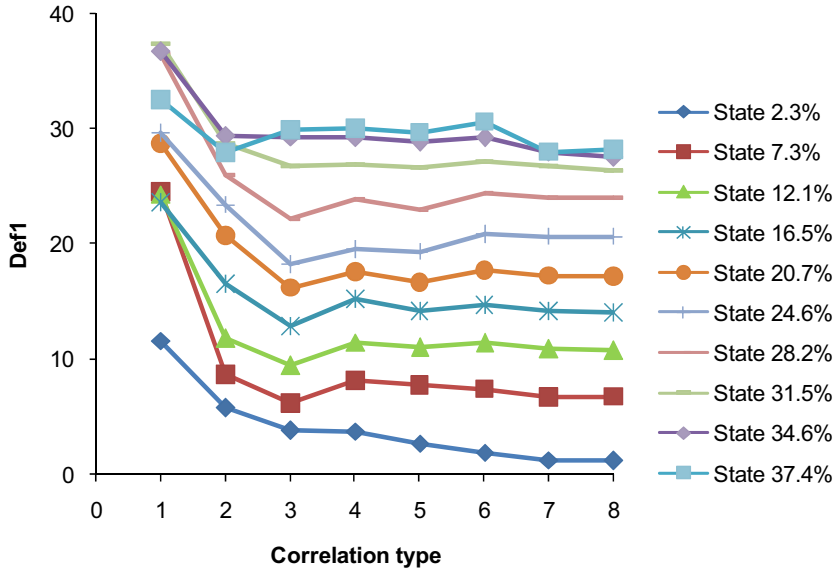

(b)

Figure V.18: Deformation (a) DefYY and (b) Def1 of correlation domain in different correlation types

The same base of correlation is used to find the optimal size of the correlation domain. One correlation zone of 64x64pixels is analysed with different correlation domain sizes : 16, 24, 32, 48, 64, 72 and 84. Two zones are chosen: one in the edge layer and the other in the center layer on sample surface. The evolution of the deformation of these two zones is presented in Figure V.19. Generally, there is no much difference in strain analysis of the treated zones if the zone size reaches 64pixels under different types of correlation domain. The results become convergent if the size of domain is greater or equal to 32pixels. However, the larger the domain size, the more we lose the compression states since the correlation

domain cannot be further detected (the behavior curve becomes shorter with large domain size as shown in Figure V.19). The optimal size of the correlation domain is found to be also 64pixels or 4mm.

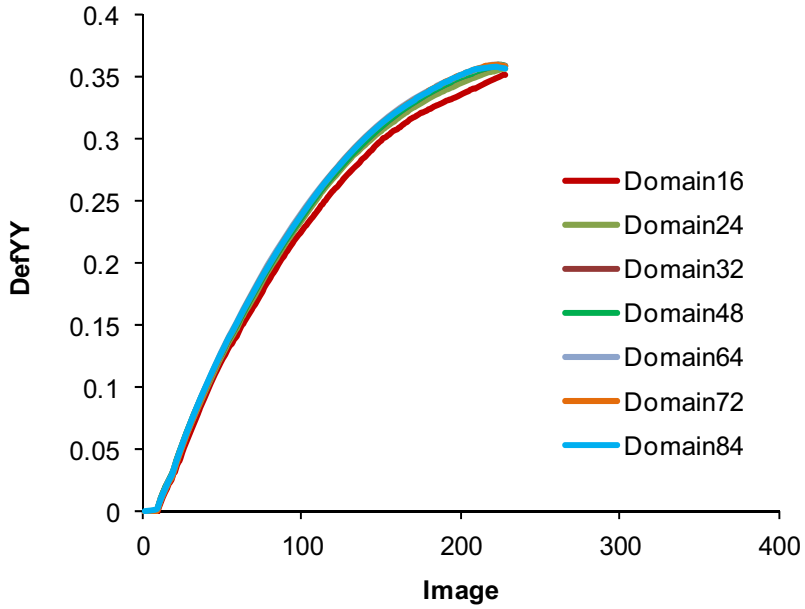

(a) Edge zone

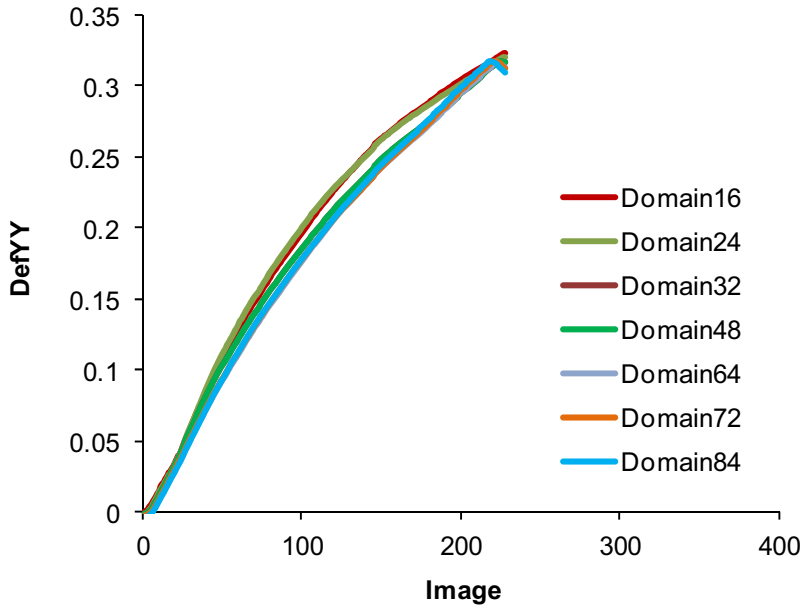

(b) Center zone

Figure V.19: Deformation DefYY and Def1 of correlation domain in different correlation domain size

b) DIC analysis

After determining the optimal size of ZOI and of the correlation domain, we study the 2D strain field by DIC on a grid of 247 zones. The size of the correlation zone is 64pixels and the size of correlation domain is also 64pixels as illustrated in Figure V.20. The maximum compression state is acquired at the 235th image of about 31%.

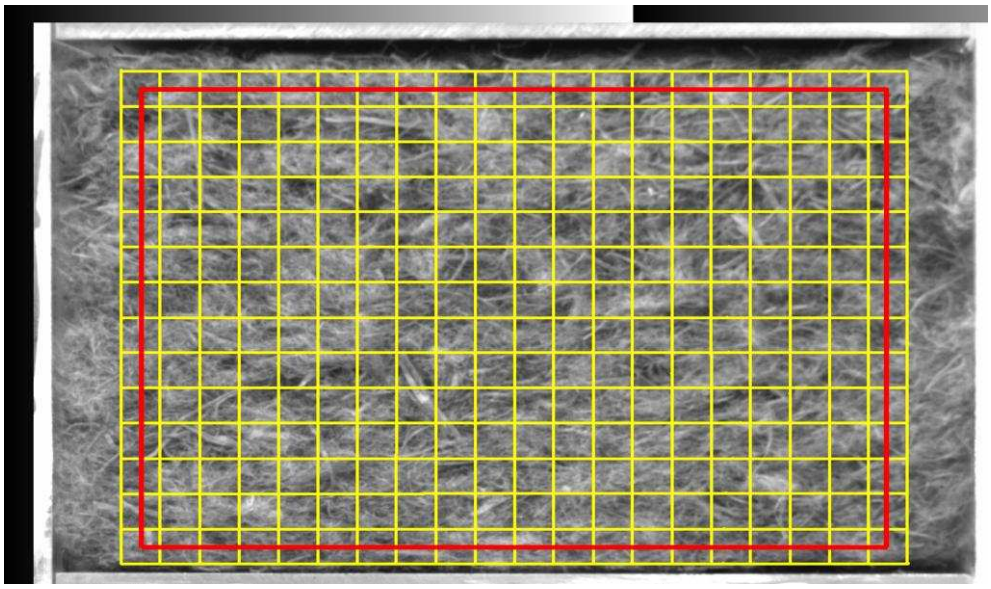

Figure V.20: Zone of interest

Figure V.21 shows the typical strain field on the sample surface at four compression states with mean strain and standard deviation as: 5.2%±3.6%, 14.4%±4.7%, 26.91%±4.8% and 30.1%±4.2%. The more compressed the sample, the smaller the difference between the local strains: for example, about 125% between the least deformed and the most deformed zone at 5%, and about 55% at maximum compression state. Local strain variations are observed, however, the evolution is not the same for all zones. It is distributed in several layers where the two layers at about 1/3 and 2/3 of the sample thickness are deformed more than the others and retain this tendency during the whole compression process (Figure V.21). This phenomenon of strain localization may be due to the multi-layer constitution of the material created during elaboration process. In other words, the studied size at the mesoscopic scale is not the size of 2D mechanical representative elementary volume. Moreover, we also observe, at high compression rates (Figure V.21d), some correlation zones are lost (top layer) or the correlation domain cannot be found in the next states. This is also the reason why the compression test under CCD cameras cannot be carried out at higher rate.

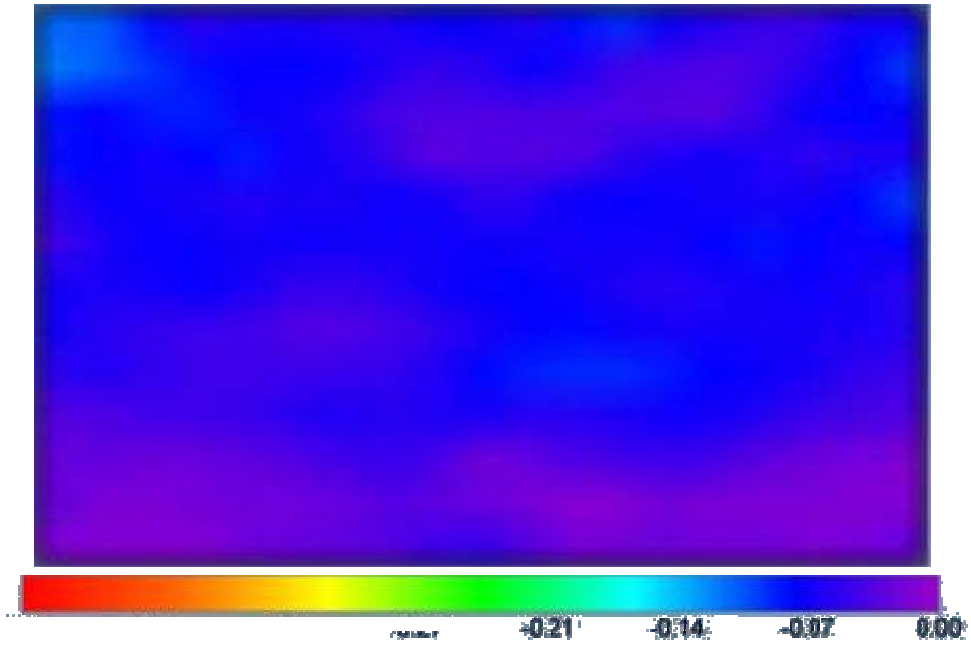

(a)

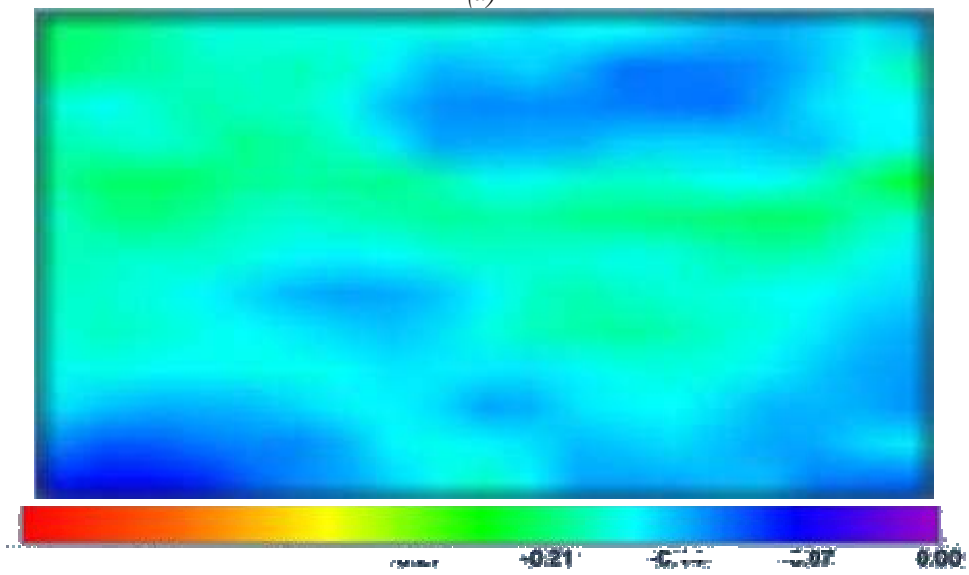

(b)

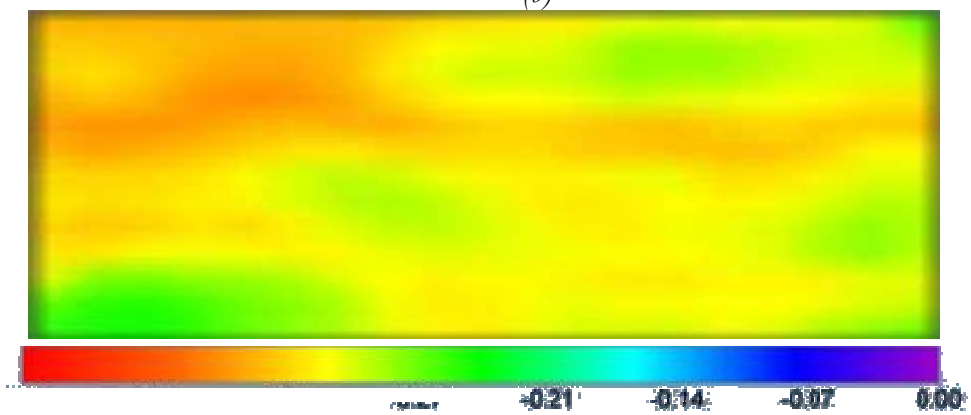

(c)

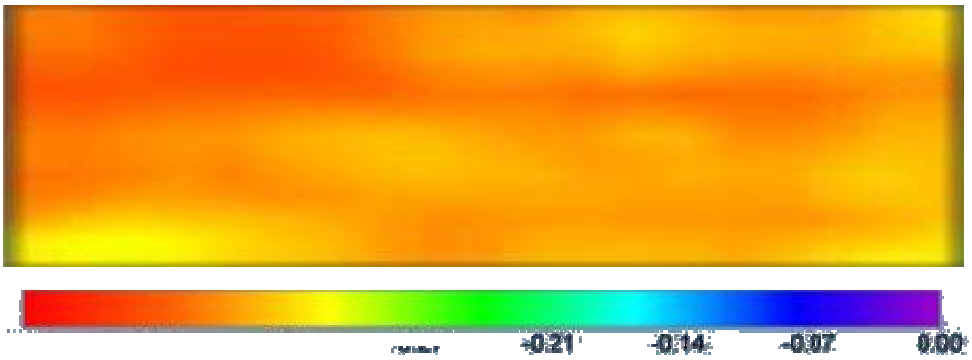

(d)

Figure V.21: Illustration of DIC: DefYY corresponding to mean compression state of (a) 5.3% (b) 14.6% (c) 27.1% (d) 30.3%

The measured strain fields are averaged for all correlation zones at all compression states and are compared to impose strain as illustrated in Figure V.22. The measured strains are smaller than the imposed strain, showing that the heterogeneity has a strong influence on DIC performance (Figure V.22). As shown in Figure V.22 and Figure V.23, DIC is well performed for loading procedure regarding wood-based fibrous material.

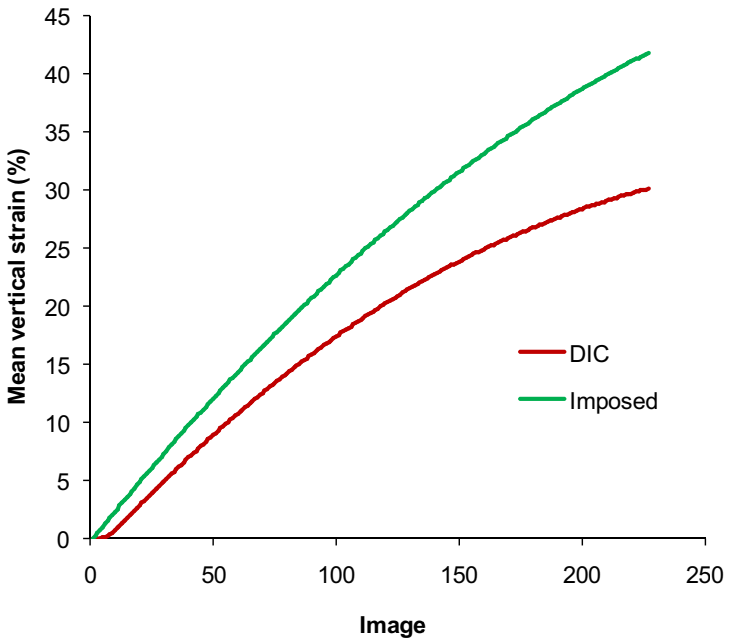

Figure V.22: Mean vertical strain at each compression loading step compared to imposed strain

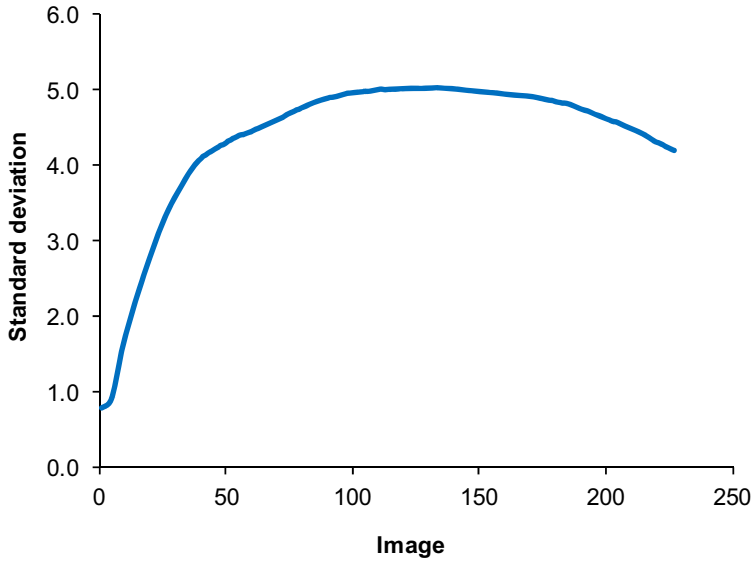

Figure V.23: Standard deviation of the vertical strain at each compression loading step

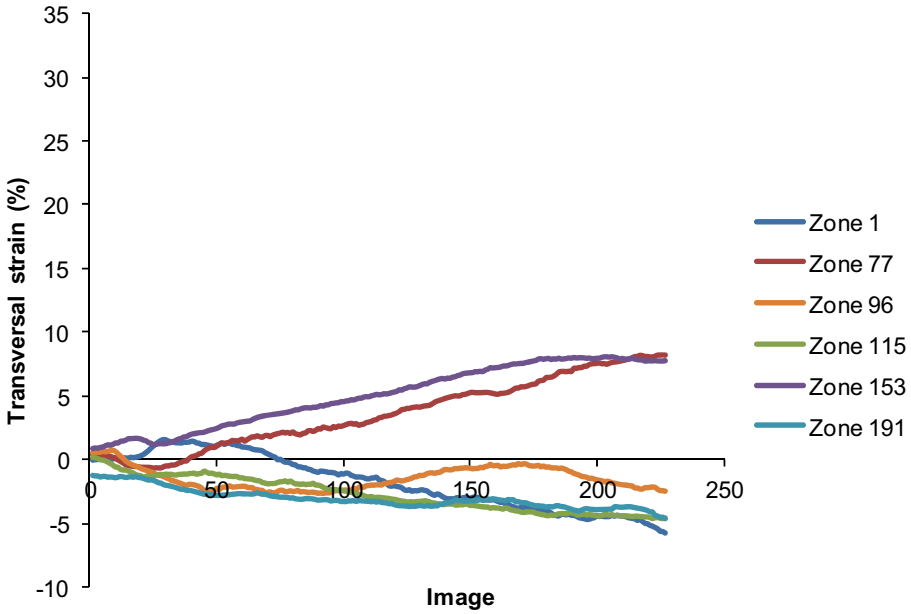

Figure V.24: Transversal strain of some edge zones

As illustrated in Figure V.24, the transversal deformation DefXX may be neglected compared to the vertical deformation DefYY, which shows that the Poisson coefficient is very small and negligible.

V.2.2 Validation of DIC by mark tracking method

The mark tracking method is another technique which also gives us the 2D strain field on the sample surface. In order to perform the mark tracking method, a distribution of artificial marks on the sample surface is required. These marks must have a clear grey level compared to that of the sample surface. The technique consists in finding the positions of the center of marks (Figure V.25a) and in calculating displacement by differences of positions between the initial and the deformed states. The tracking of four marks gives us the plane deformation tensor of one zone which is assumed to have homogeneous deformation. The tracking of more than 4 marks will give us full 2D strain field of the sample surface. With this principle, the advantage of the mark tracking method is that the strain analysis depends less on the surface pattern than DIC does: as long as the marks are visible, the technique will always give correct results. Thereby, the mark tracking method is employed to validate DIC. As the transversal strain can be negligible, the strain DefYY approximates the strain Def1. Consequently, the validation will be carried out by comparing the vertical strain of pairs of corresponding zones of the same size on the sample surface, one zone of the pair is treated with DIC and the corresponding one is analyzed with the mark tracking method. These zones are chosen from the middle layer in order to eliminate all edge effects.

a) Analysis of results of the Mark tracking method

The mark tracking method is carried out using Deftac software [78] and DIC on the same sample P02 but on the opposite facet. A system of 54 marks whose distance is about 10cm, corresponding to about 150pixels is created which gives us a system of fourty zones of interest (ZOI). The deformation of each ZOI is assumed to be homogeneous.

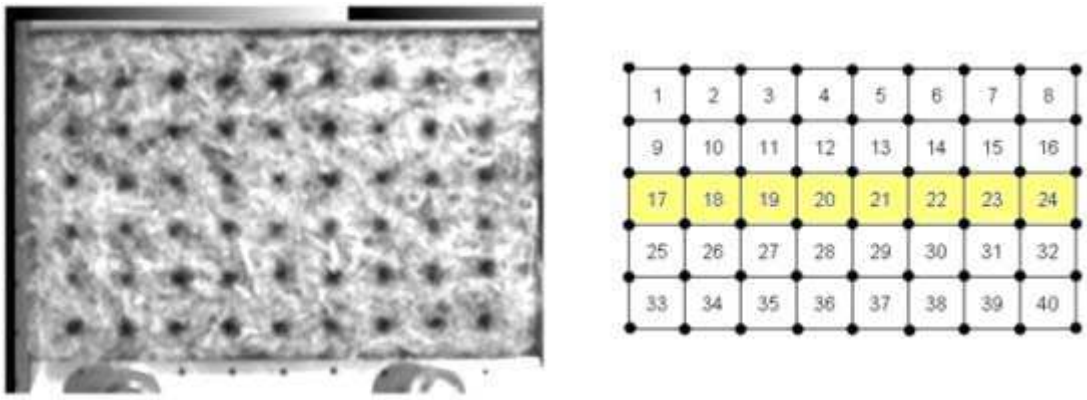

(a) *(b)*

Figure V.25: (a) Real position and (b) idealized position of marks on sample surface

The evolution of vertical strain in relation to the applied force is investigated for the center layer (from zone 17 to zone 24) as shown in Figure V.26.

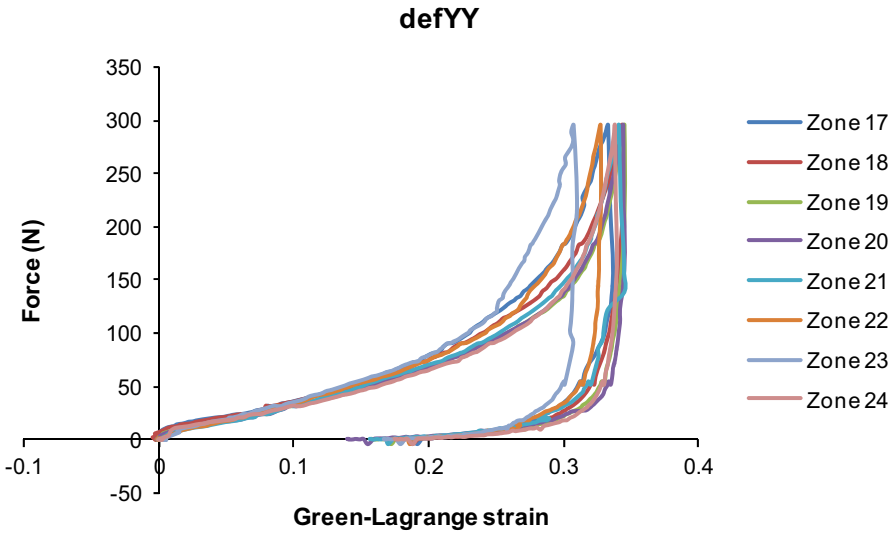

Figure V.26: Force-Vertical strain relation obtained by Mark tracking method for center layer zones (c) bottom layer zones (d) edge zones (e) vertical center zones

However, the mark size and the distance between marks are limited by the sample properties. We would like to further compress the sample, but we had to stop at about 32% of the compression rate (about 50% of small deformation) because at this rate, the marks are superposed, the mark tracking method cannot distinguish between marks and the results, therefore, are not correct. But at unloading procedure, the technique is able to be continued.

In order to validate DIC, we create DIC zones comparable to the marks at the center layer on the sample surface (Figure V.27), which gives us in total eight correlated zones in order to prevent the boundary effect as far as possible (counted from left to right). The distance between correlation domains is 150pixels, corresponding to 10mm in two directions. The size of correlation domains is chosen to be 64pixels.

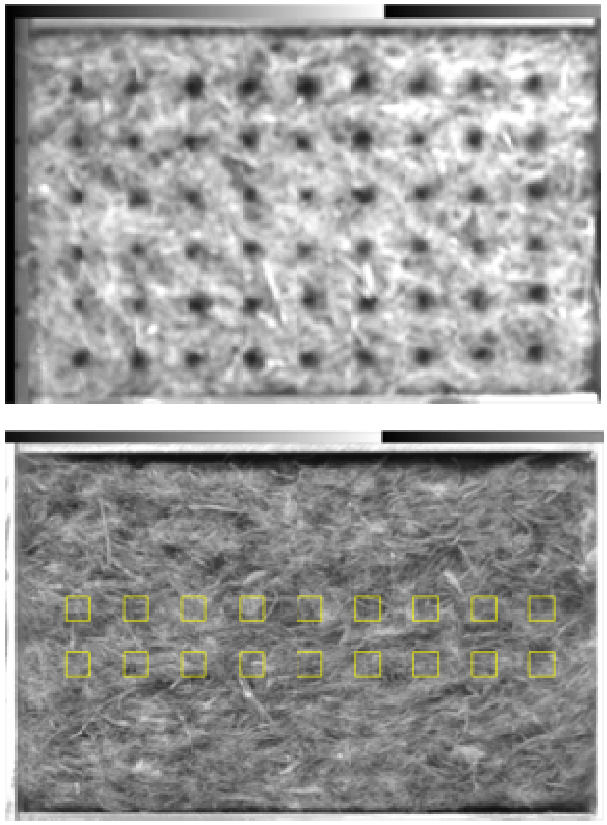

Figure V.27: Base of comparison for Mark tracking method (upper image) and DIC (lower image)

As illustrated in

Figure V.28, these two methods have a good superposition until the maximum compression rate in loading procedure. The center zones give a better agreement.

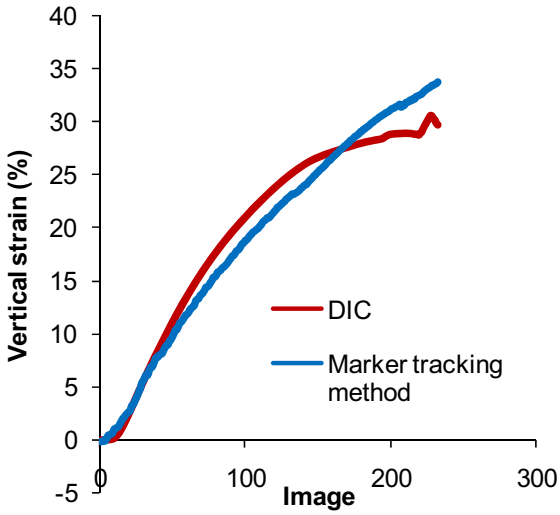

(a) 1st zone

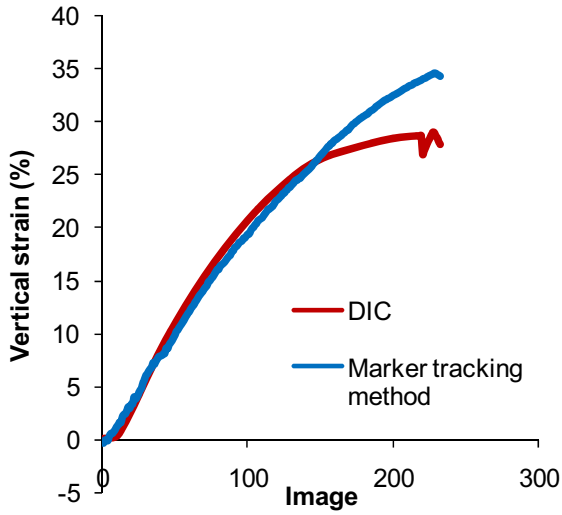

(b) 2nd zone

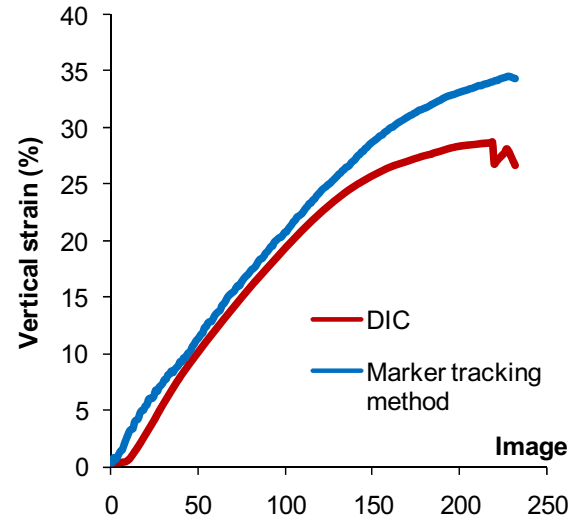

(c) 3rd zone

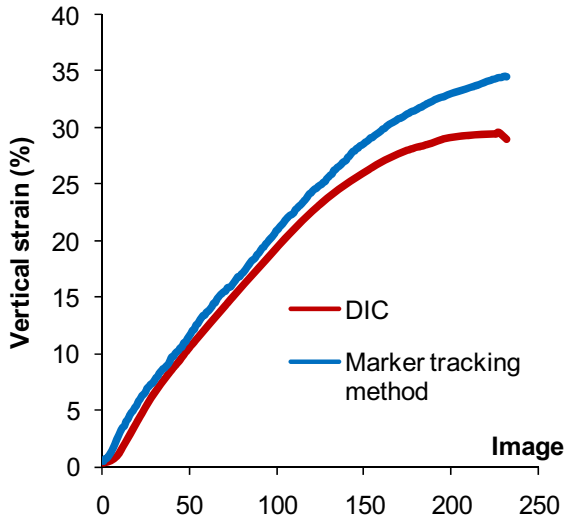

(d) 4th zone

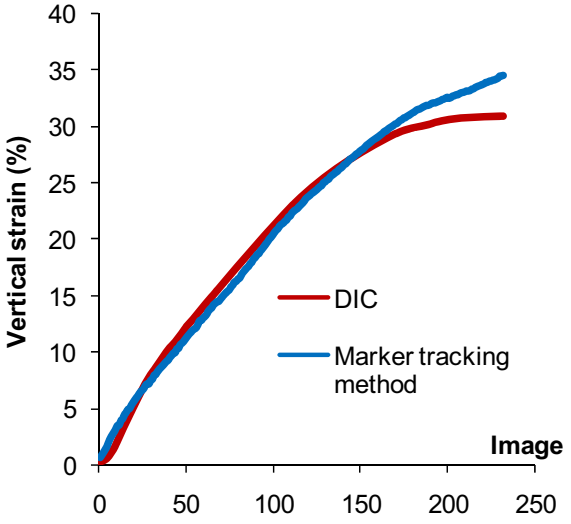

(e) 5th zone

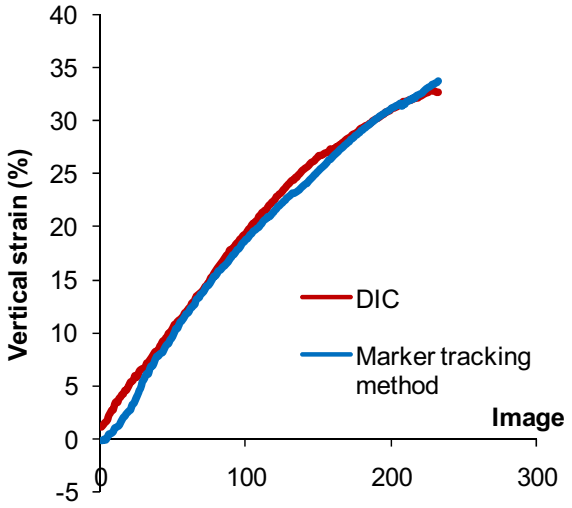

(f) 6th zone

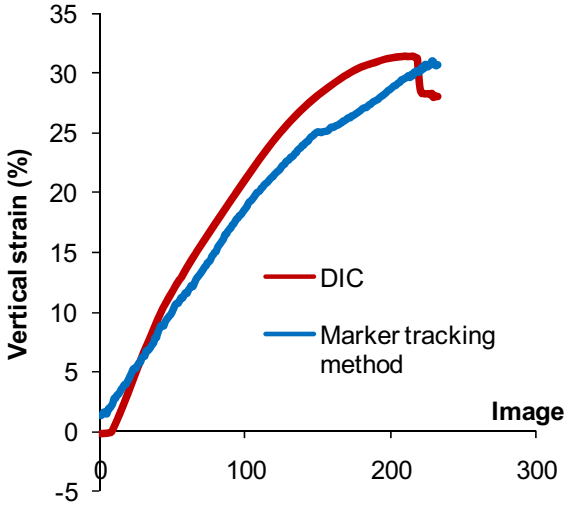

(g) 7th zone

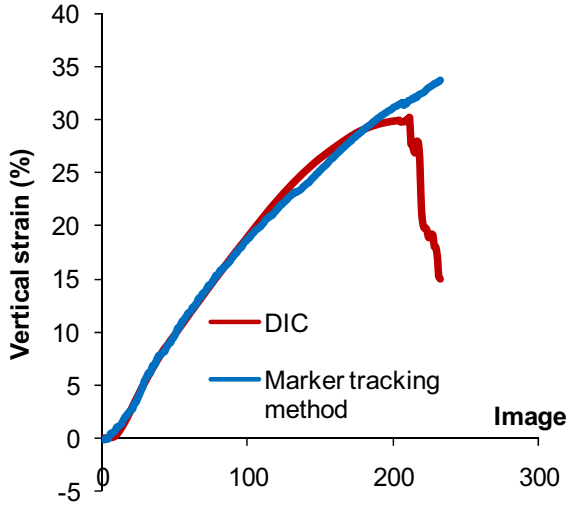

(h) 8th zone

Figure V.28: Comparison between DIC and Mark tracking method

Both correlation techniques, the mark tracking method and DIC, produce good and comparable results for the loading procedure. However, the results only reflect the strain behavior of the sample surface which is not sufficient for such a heterogeneous and complex 3D structure as in wood-based fibrous material. A 3D study of the strain behavior is expected. Extended from the 2D technique, the 3D mark tracking method and DVC are developed. However, the 3D mark tracking method requires regular marks tridimentionally distributed inside the material which is difficult in all cases to be done without modifying the material, and is naturally not adapted and unexpected for this kind of the material: a modification of the microstructure will lead to totally new behavior. The study of the 2D strain field by DIC is then a preliminary and validation step for the 3D strain field study by DVC presented in next paragraph.

V.3 Local 3D study by microtomography and DVC

The cylinder sample is compressed from 0 to 32% with 8 loading steps (from 4.9% to 31.6%). As the resolution of microtomographic images and the porosity of the material are high, the size of the correlation domain *D* is chosen to be equal to 90×90×90voxels (about 0.54x0.54x0.54mm) in order to have a sufficient volume of fibers into *D*. To decrease the runtime of DVC process as well as computer memory, the resolution of volume images is divided by three (from 6µm/voxel to 18µm/voxel): the grey level of each voxel of a small-resolution image corresponds to the average of grey levels of 27 neighbouring voxels in the high-resolution image (Figure V.29b). Then the displacement field is obtained on a grid of 4950 points whose distance-to-distance is 20 voxels at the small resolution (Figure V.29). The absolute local strains in relation to the initial state are calculated with a gauge length equal to 60 voxels. The average strains can be obtained with a scheme of non-centered finite differences by taking a gauge length corresponding to dimensions of the full zone of interest. The decrease of the analysed image resolution does not affect DVC results compared to its initial resolution as the changes of grey level dynamic of microtomographic images can be ignored. The notion of compression state is defined based on mean E_{zz} strain (Table V.4) calculated by DVC obtained by performing DVC with a system of 27 points on the whole sample in which the correlation domain size is 90 voxels and the distance between grid points is 420 voxels at the initial state (Table V.4).

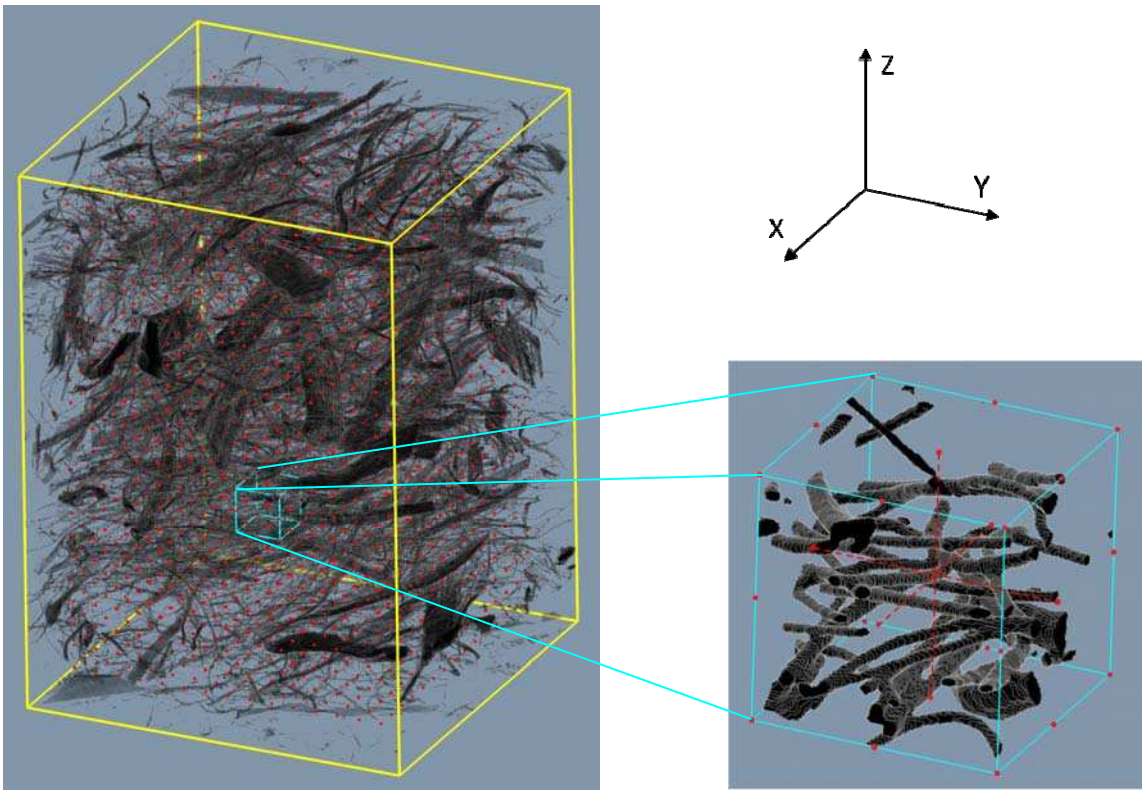

Figure V.29: (a) Grid of measurement points in the sample volume, (b) A local sub-volume V^i used to calculate strains

Figure V.30 shows the comparison between imposed and mean E_{zz} strains on the zone of interest for DVC, smaller than the full volume of the sample. At each loading step, the same values are found as shown by the equation of the linear-regression curve (*mean* E_{zz} *= 1.01 imposed* E_{zz}), which proves that the analysed sub-volume is mechanically representative to the full sample, the same result is obtained in Figure V.14 when compared to compression test on the large sample.

Table V.4: Mean Ezz strain calculated by DVC at different compression states

Compression state	Mean correlated Ezz strain (%)
0	0.0
1	4.9
2	9.3
3	13.9
4	18.4
5	22.5
6	26.1
7	28.1
8	31.6

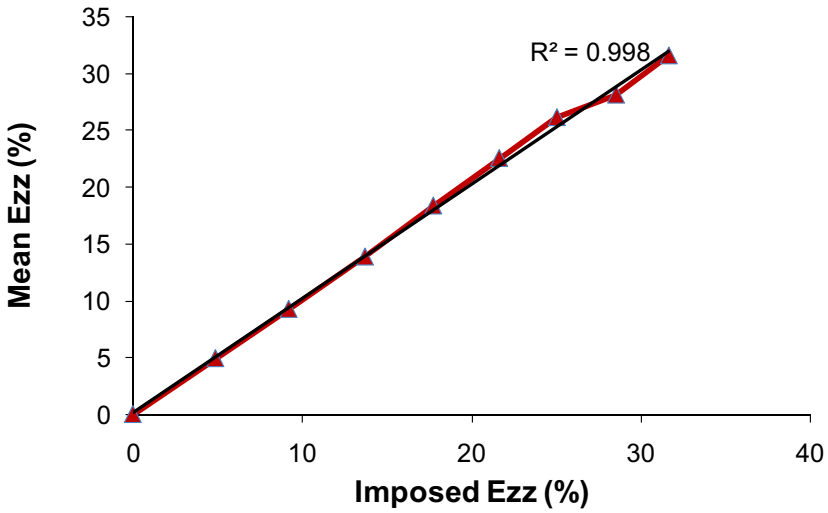

Figure V.30: Comparison between mean strains Ezz calculated by CorrelVol and imposed strains

The transversal (*Exx, Eyy*) and shear deformations are negligible compared to longitudinal *Ezz* strains (less than 0.1 of *Ezz*) as shown in Figure V.31. Indeed, considering the final compression state, the mean *Ezz* strain is found to be around 31.6% while the mean strains are 0.81% and 0.25% in *x* and *y* directions, respectively, and the local *Ezz* strains vary between 7% and 48%. That's why we are only interested in *Ezz* strain.

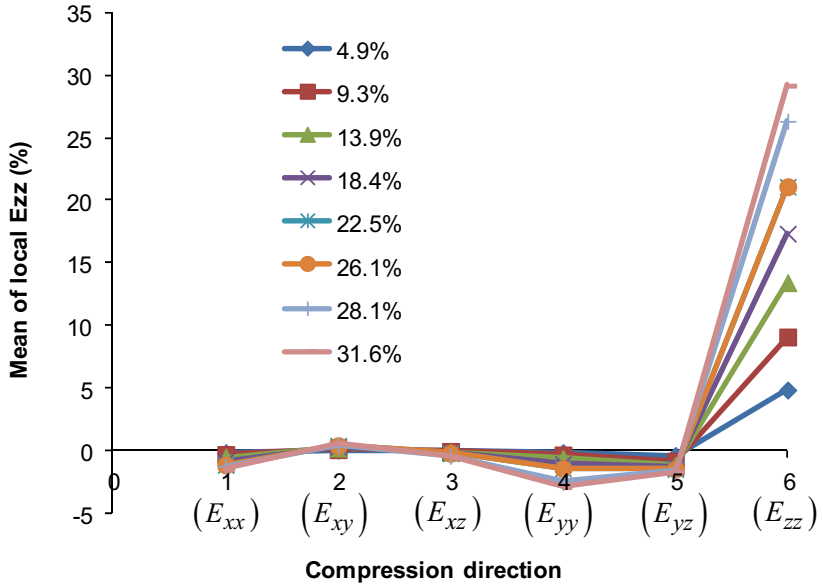

Figure V.31: Mean value of local strain in different directions

Figure V.32 presents the Ezz strain field obtained by DVC in the loading direction at different compression states (Ezz). Indeed, material shows a local strain field Ezz which is strongly heterogeneous: strains are higher in some areas and smaller than the average of Ezz strain in other zones. This strong heterogeneity is due to the complex microstructure.

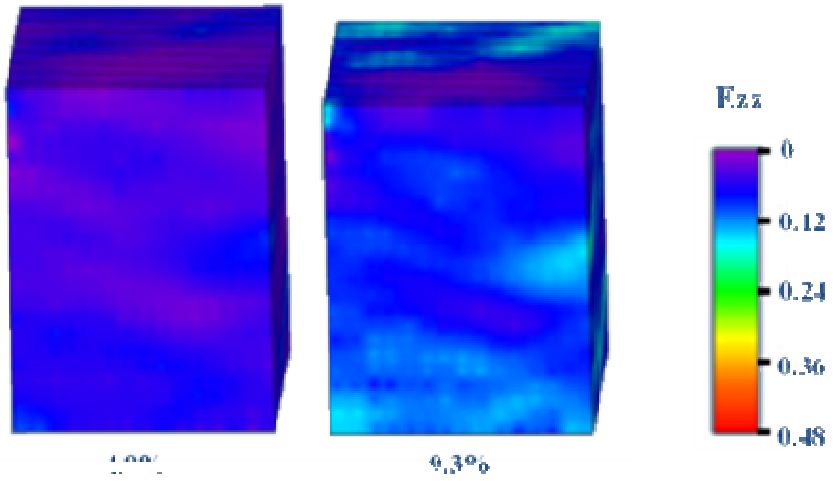

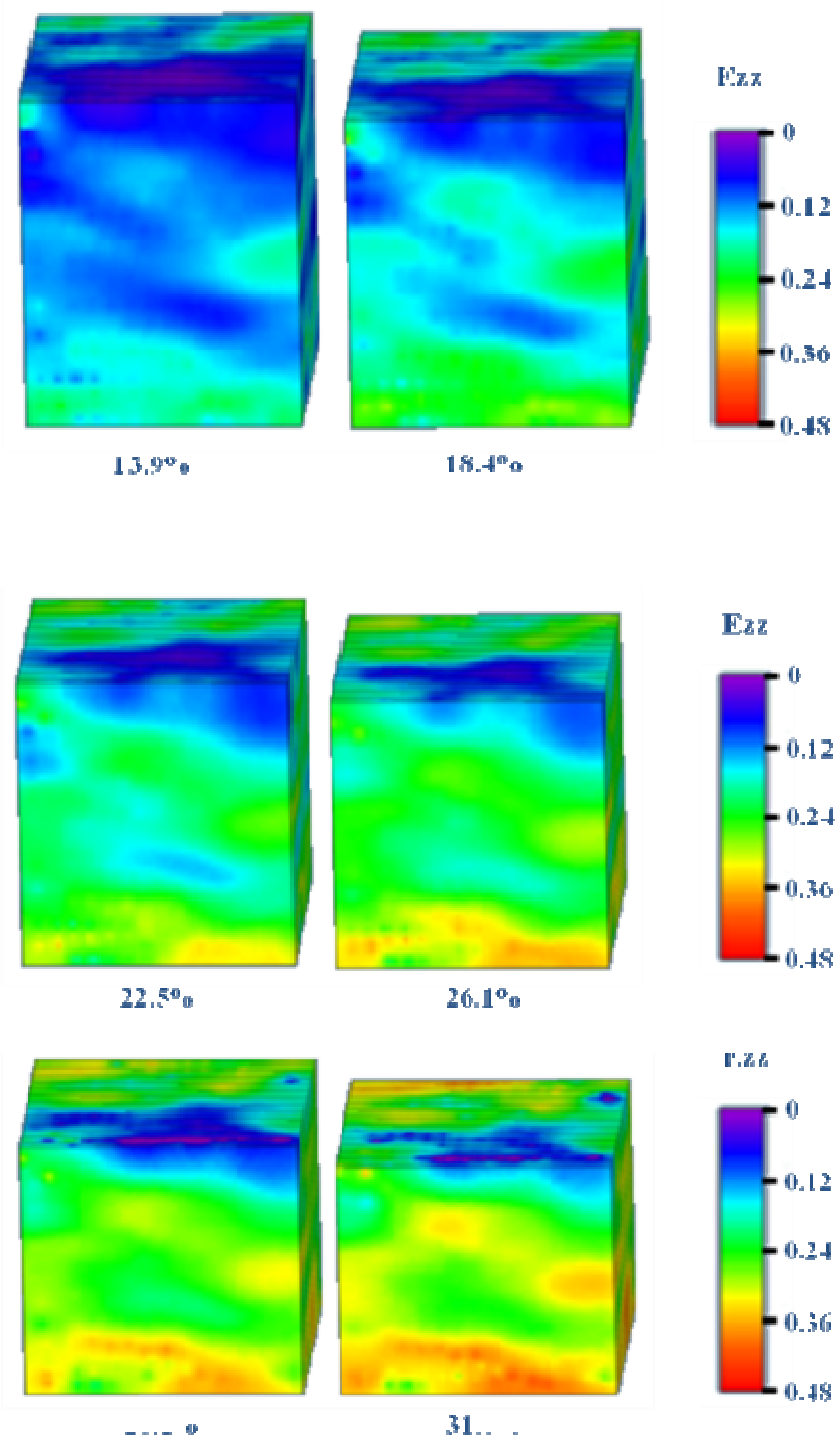

Figure V.32: Ezz strain field at different compression states

The most deformed areas stay almost the same during the loading: at each strain step, the same zones are activated to contribute to strain as shown in Figure V.33. Indeed, this figure gives the field of *Ezz* strain increments at each step in the same slice of the volume. The areas where increments are higher correspond to same parts of the microstructure whatever the mean level of strain. Nevertheless, we can note the beginning of a reorganization of strain at the state 31.6% because

some new areas of strain localization appear describing a new behavior which may be related to the microstructure. This subject is put into future researches when higher levels ofimposed strain will be studied.

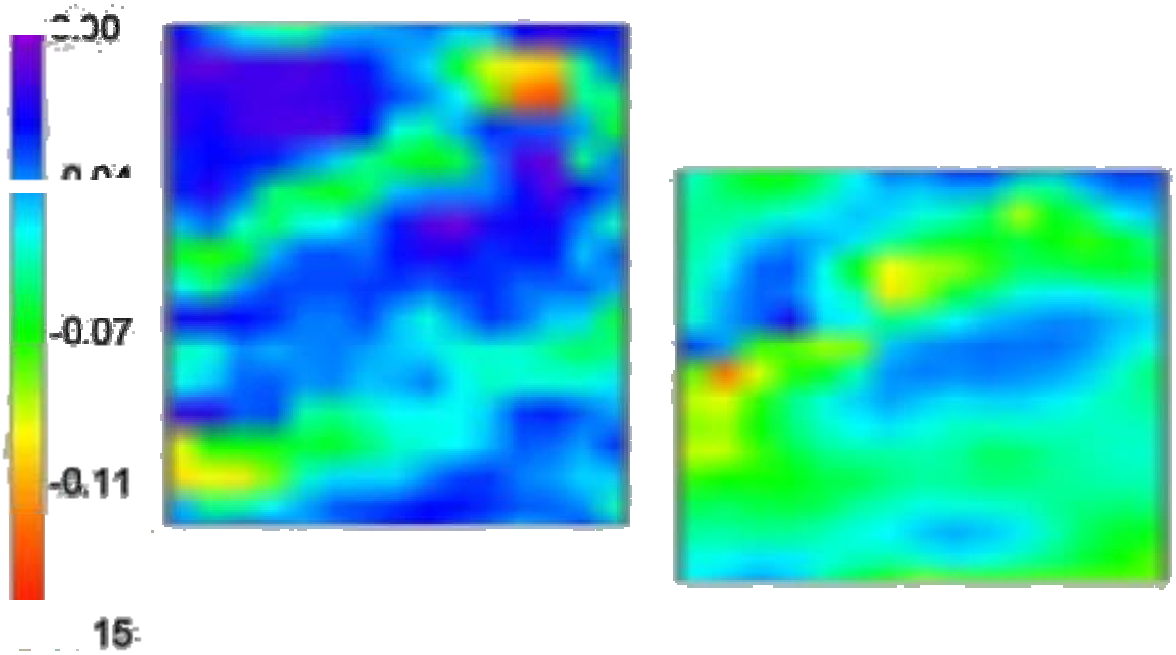

(a) State 4.9% (b) State 18.4%

(c) State 31.6%

Figure V.33: Field of incremental Ezz strains at different load states for slice 320

In an attempt to investigate the heterogeneity level of local strains and the evolution of this heterogeneity level in function of the applied load, we are interested now in the ratio of each local strain to mean *Ezz* strain. Figure V.36 shows *Ezz* strains normalized by mean *Ezz* strain at each loading state. The more compressed the material, the closer to 1 the ratio between *Ezz* strains and mean *Ezz* strain. We can observe that the strain field becomes uniform and the mechanical behavior of the material has the tendency to be similar to that of a homogeneous material. This evolution of strain heterogeneity is confirmed by a

statistical analysis in the full volume of interest (Figure V.31). The calculus of standard deviation $\sigma_{Ezznorm}$ of normalized Ezz quantifies global strain heterogeneity.

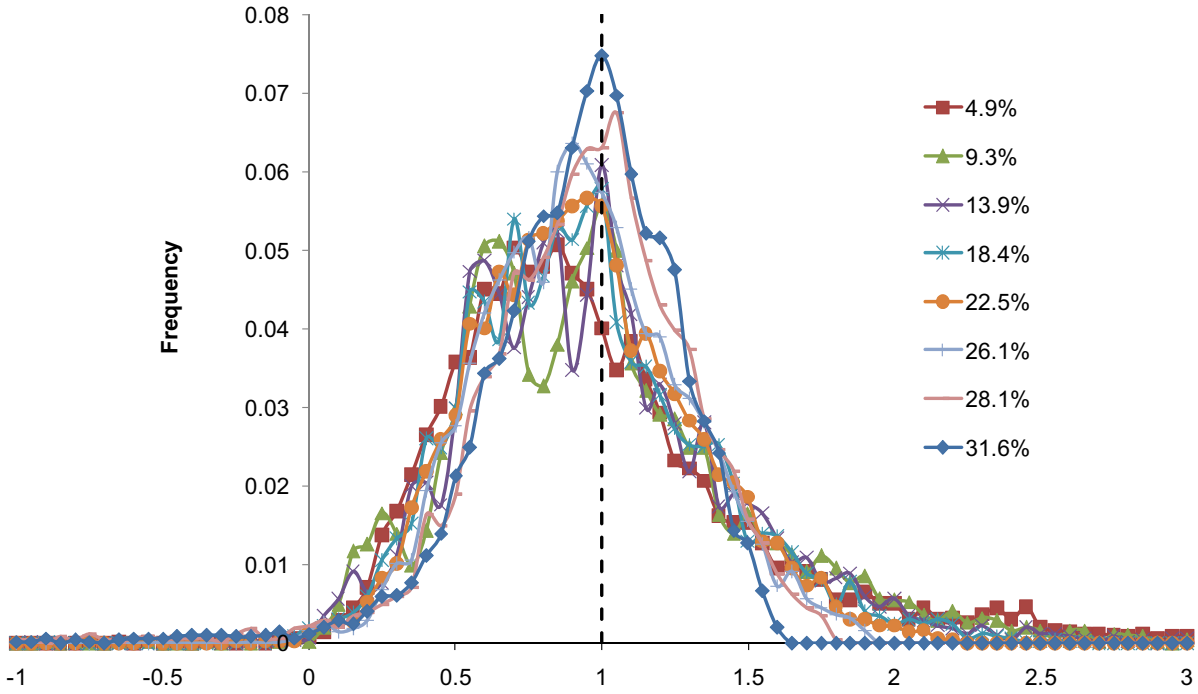

Figure V.34: Histogram of normalized Ezz strain field at different states

The decrease of heterogeneity level or of $\sigma_{Ezznorm}$ during compression is illustrated in Figure V.35 which is then graphically presented in Figure V.36.

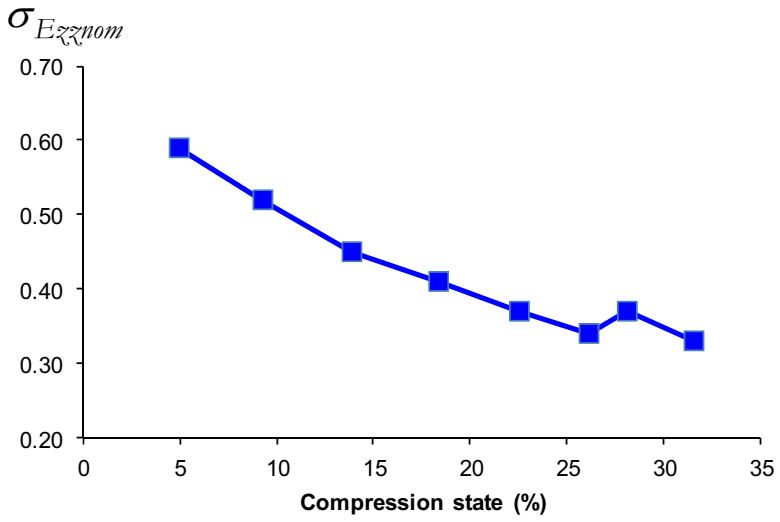

Figure V.35: Value of $\sigma_{Ezznorm}$ at different compression states

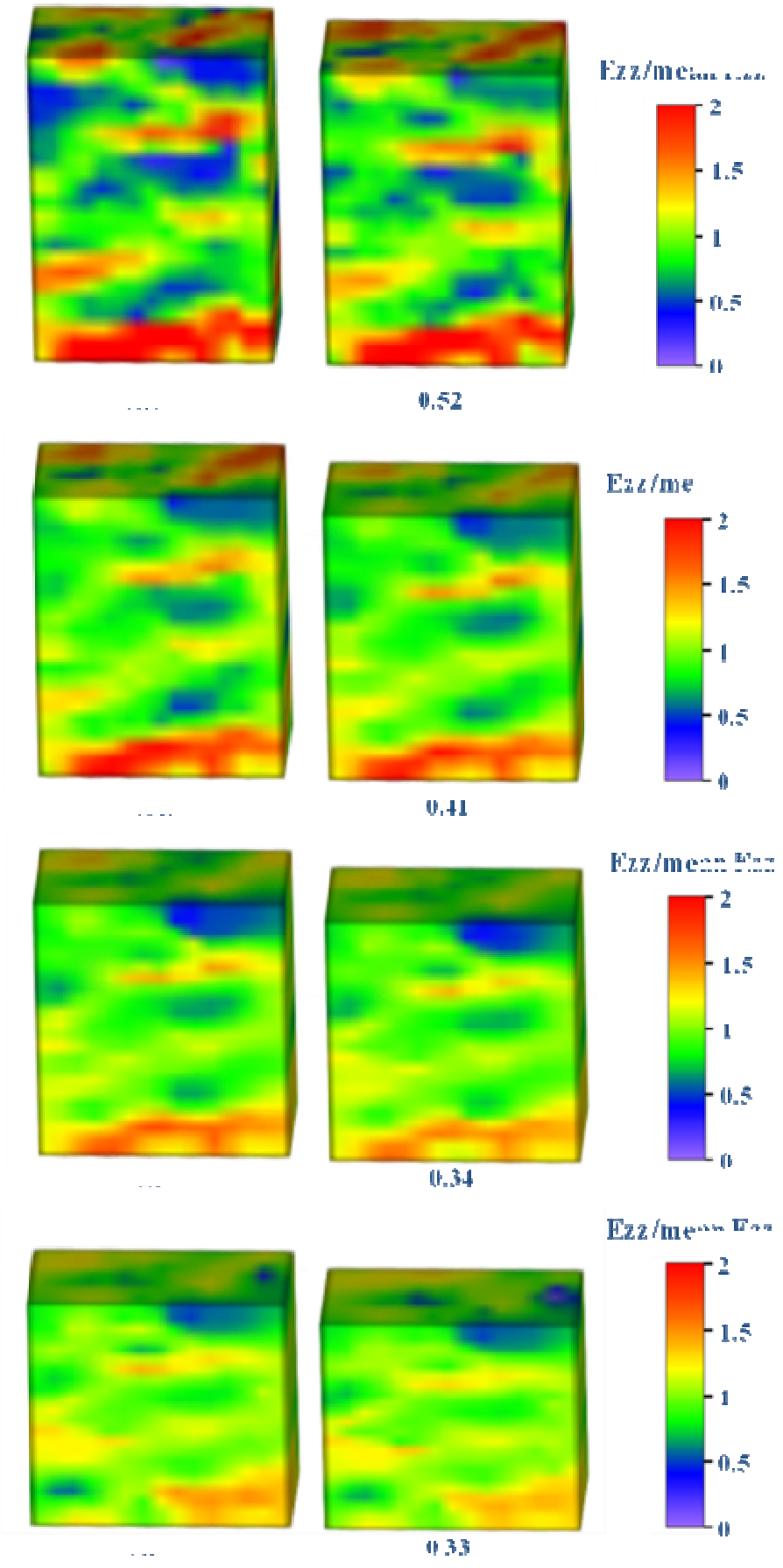

Figure V.36: Standard deviation of normalized Ezz strain field at different states

V.4 Conclusion of chapter V

Chapter V is dedicated to describe the mechanical behavior of the material at different scales: the global behavior at the macroscopic scale, 2D strain field on the sample surface using DIC at the mesoscopic scale and 3D full strain field inside the material at the microscopic scale thanks to DVC. 2D study is the validation step for 3D strain analysis. At the macroscopic scale, the material shows non-linear behavior with hysteresis and residual deformation as well as rigidifying effect. The global behavior of the material is in best agreement with Van Wyk's experimental model. At the mesoscopic and the microscopic scales, the material exhibits a very strong heterogeneous local strain due to its microstructural properties. The Young's modulus is found to be about 8400Pa and the Poisson effect could be negligible. The chosen size of the small cylindrical sample in the CT-test is larger than the size of mechanical REV.

In this chapter, the precision of the DVC performance on the studied material is not fully treated, depends on three major factors: test process (test set-up, strain imposing, image acquisition etc.), quality of reconstructed microtomographic images (the existence of noise, ring artefacts and quality of image contrast) and performance of DVC on fibrous material which is strongly influenced by the great existence of pores. A preliminary evaluation of DVC performance is done by performing DVC with different sizes of correlation domain and evaluating the correlation coefficient. The size of the correlation domain, which is most adapted for this material, is obtained. The precision of the DVC technique is obtained by performing DVC on the CT-images which are imposed a certain displacement (no imposed strain). However, this test could not be carried out later at the I2M laboratory due to some technical problems occured with the CT-machine. The additional CT-test at ESRF, Grenoble is then carried out for this purpose, however, it is not fully exploited. Consequently, the study of the DVC precision on wood-based fibrous material is still studied and put into short-term perspective.

Nevertheless, the potential of using DVC for fibrous samples to obtain 3D strain field is demonstrated. The advantage of DVC compared to DIC is that it is more realistic since the deformation mechanisms strongly depending on local microstructure when the sample is deformed, are highly three-dimensional: change of the sample configuration, the increasing of fiber contacts, the evolution of pores, etc.

The results from this chapter show the same trend of the material at the macroscopic and the microscopic scales where the transversal strain can be negligible and the material becomes more and more homogeneous during the compression. However, at the mesoscopic scale, it seems that the strain field is not precisely determined as it does not depend solely on the heterogeneity of the sample surface.

The effort to study the microscopic behavior is now achievable with the contribution of the microstructure, obtained through mathematical morphology, which allows us to confront the relationship mechanical behavior-microstructure in the next chapter.

Chapter VI: Correlation between mechanical behavior and microstructure

From the results of strain analysis in the previous chapter, we see that it is not evident to consider the 2D strain field analysis in relation to microstructure because the strain field at this scale does not solely depend on the visible microstructure on the sample surface. As the material is strongly 3D heterogeneous, a 3D analysis for both local strains and microstructure is desired. In this chapter, we will present the confrontation between the mechanical behavior and the microstructure at the macroscopic and the microscopic scales. Three microstructure parameters are considered: volume fraction, size of pores and fibers and local orientation of fibers. Three networks are taken into account: the wood network, the PES network and the network of all fibers. We will show that the volume fraction plays the most important role in the material behavior. The last section of this chapter will be destined to describe the numerical simulation using the finite element method which is implemented into Cast3M. Two elastic constants, the Young's modulus and the Poisson coefficient, that are attributed to each element at the microscopic scale, are deduced from global behavior. In this simulation, by minimizing the displacement difference between the simulation and experimental data (obtained from DVC) under different relations, we will obtain the best expression of Young's modulus at the macroscopic and the microscopic scales.

VI.1 Relation between global strain and microstructure

VI.1.1 Relation between pores and compressive behavior

a) Evolution of pore size during compression using granulometry by opening method

The granulometry of pore size at three compression states is presented in Figure VI.1. Using granulometry by opening, the mean pore size is found to be around 0.5mm at the initial state and decreases, not only mean value but also standard deviation (Figure VI.1), during compression which shows that the pore size tends to become uniform.

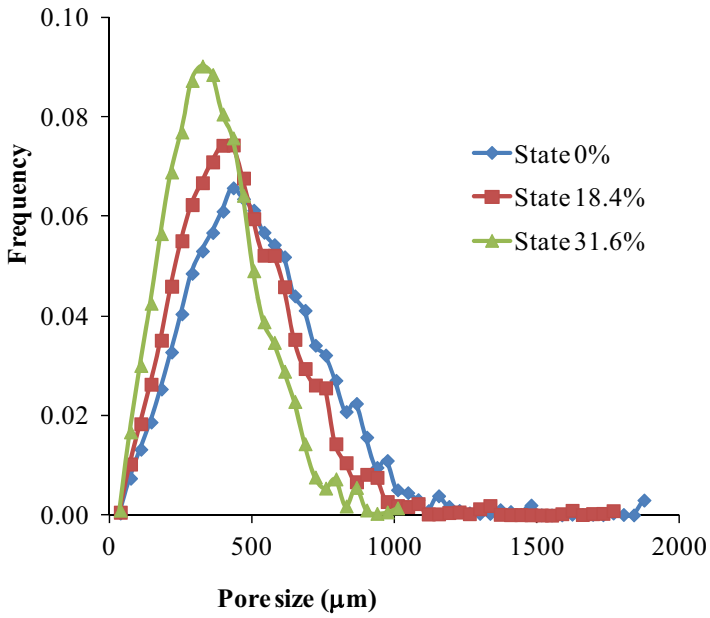

Figure VI.1: Size distribution of pores at three compression states: 0%, 18.4% and 31.6%

The quantitative results of Figure VI.1 are summarized in Table VI.1 which is added by results of other compression states and illustrated in Figure VI.2.

Table VI.1: Mean value and standard deviation of pores obtained from granulometries by opening method

Compression rate	Input
0%	518 ± 239µm
4.9%	508 ± 238 µm
9.3%	490 ± 226 µm
13.9%	471 ± 218 µm
18.4%	454 ± 213 µm
22.5%	432 ± 202 µm
26.1%	416 ± 191 µm
28.1%	393 ± 178 µm
31.6%	369 ± 163 µm

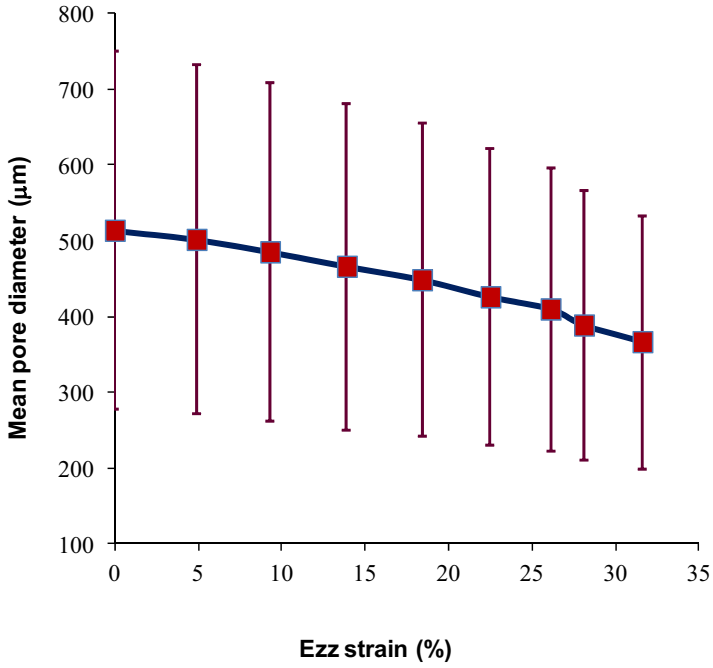

Figure VI.2: Mean value and standard deviation of pore sizes at different compression states

b) Spatial distribution of pores during compression using local thickness method

Table VI.2 gives the mean values and standard deviations of pore sizes at three compression steps: 0%, 18.4% and 31.6% which are then presented in Figure VI.4 in comparison with values obtained by the opening method. We observe the same evolution of pore size compared to the one of the granulometry by opening method (Figure VI.4), but obtained values between two methods are different: pore sizes found by the local thickness method (LTK) are smaller compared to the one of the granulometry by opening method (OP) (Figure VI.3, Figure VI.4). The same results are observed by Elmoutaouakkil [83] when studying the structure of solid foams. The difference between two methods may be due to the two following reasons.

Firstly, due to the method to determine diameters: OP gets pore size by displacing a sphere or an octahedron (structuring element) all over the pore voxels and LTK determines pore size by fitting the largest sphere into the pores. LTK may have more difficulties when fitting this sphere into a discretized structure.

Secondly, due to the determination ways of the volume (or frequency) of each pore size: while local thickness gives the proper volume of each size *i*, opening accumulates the entire volume of pore size α $(i-1<\alpha\leq i)$ and considers the total volume is that of pore size *i*. We can easily recognize that granulometry by opening

is quite similar to the principle of the sieving process with sieves of different hole sizes, where the size of a grain is determined by the minimum size of the hole that sieves the grain.

Table VI.2: Mean value and standard deviation of pores obtained from local thickness method

Compression state	Pore size
Initial state	365 ± 180µm
18.4%	315 ± 160µm
31.6%	259 ± 125µm

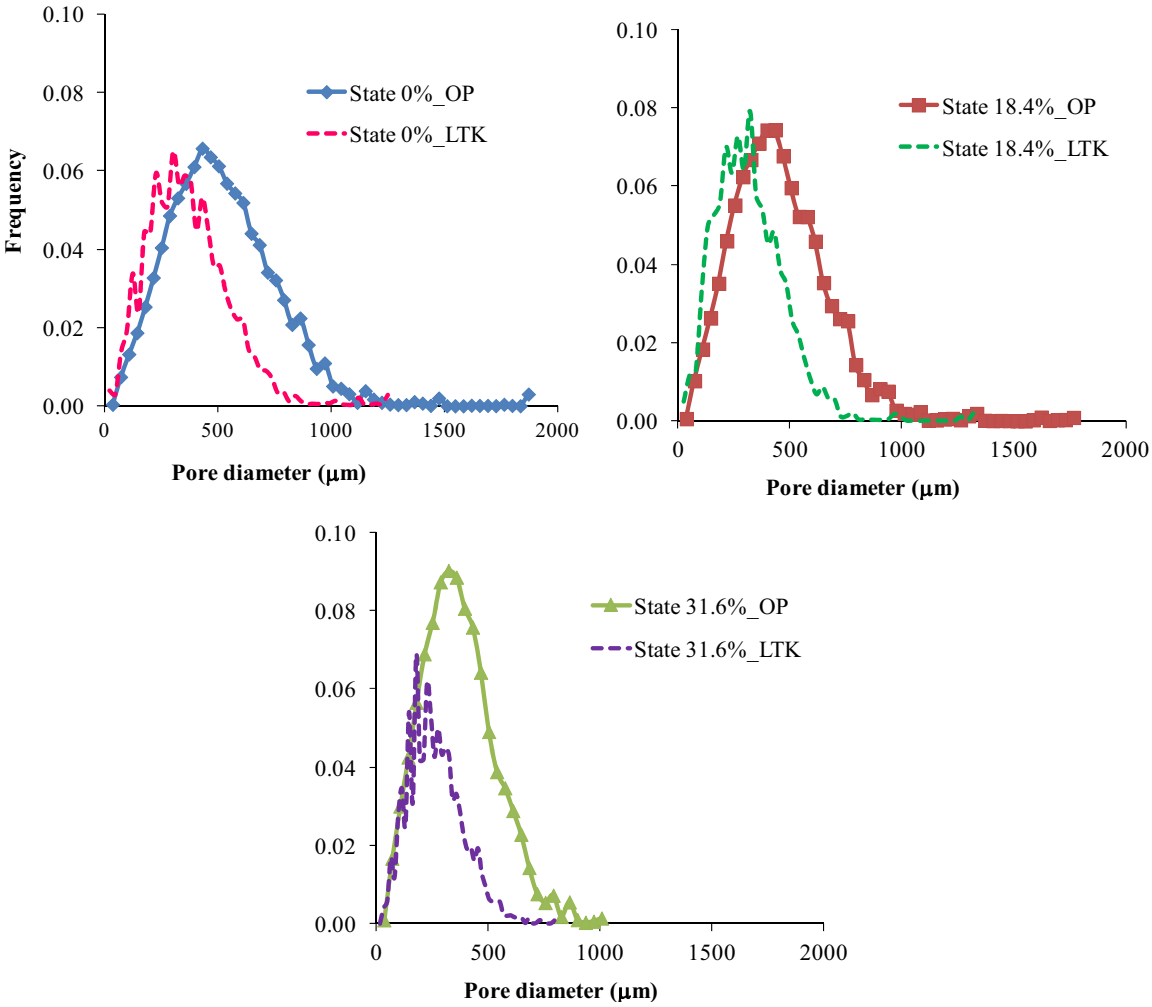

Figure VI.3: Comparison of distribution of pore sizes obtained by Granulometry by opening (OP) and by Local thickness theory (LTK) at different compression states

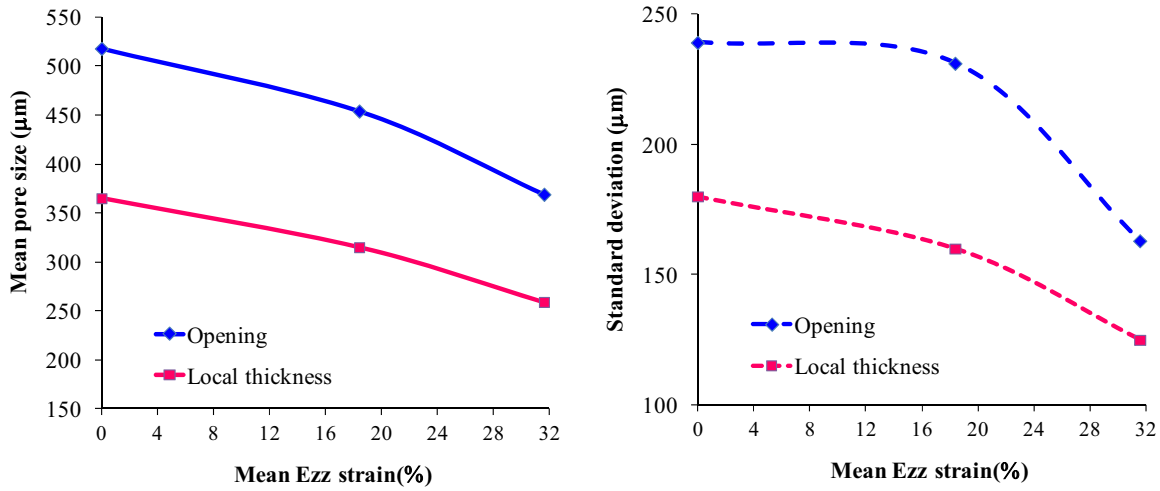

Figure VI.4: Comparison of distribution of pore sizes obtained by Granulometry by opening (OP) and by Local thickness theory (LTK) at different compression states.

These two methods are complementary: while OP gives the global distribution of pore sizes, LKT complements it by giving us the local distribution of pores in the network space. However, quantitatively, we expect to obtain equivalent and comparable pore size distribution from the two both methods as the principle of LKT method is not much different from OP method. A study on the application of OP and LKT on wood-based fibrous material is still to be developed in future researches. Figure VI.5 presents a perspective view, starting with the top layer of the sample, showing the spatial distribution of pores with its corresponding size at three compression states 0%, 18.4% and 31.6% (However, the same color does not give the same size in different images). We can clearly observe that the pore sizes decrease and become more and more uniformly distributed.

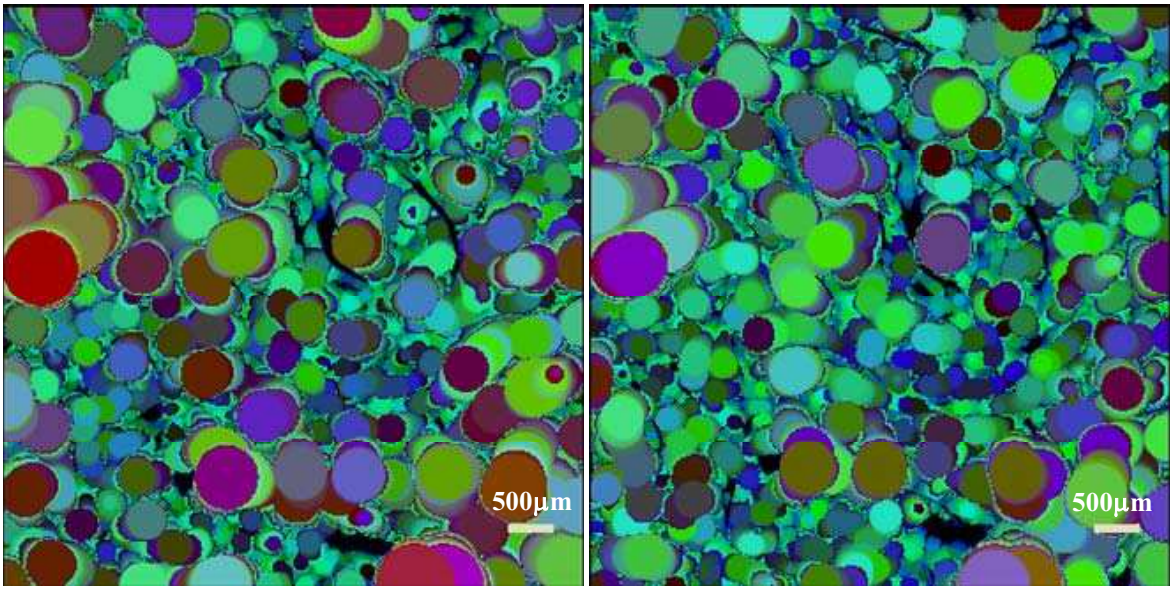

(a) *(b)*

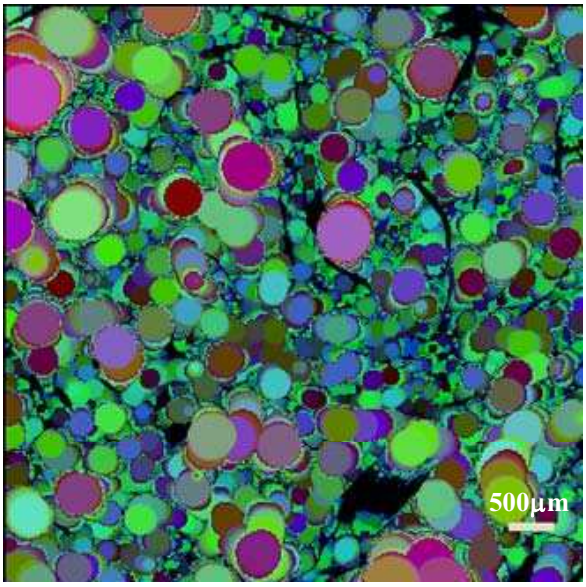

(c)

Figure VI.5: Pore size repartition using LTK at 3 compression states (a) Initial state (b) State 18.4% (c) State 31.6%

c) Relation between the pore volume fraction and the compressive behavior

Since the deformation happens by excluding the pores out of the sample and the lateral strain being negligible, the Green-Lagrange global strain in loading direction can be expressed through the volume of the sample as

$$e_{zz} = \frac{1}{2}\left[\left(\frac{h}{h_0}\right)^2 - 1\right] = \frac{1}{2}\left[\left(\frac{V}{V_0}\right)^2 - 1\right] \tag{6.1}$$

where V_0, V are sample volume at initial and deformed state.

By definition, the porosity of the sample is

$$p = \frac{V_p}{V} \tag{6.2}$$

at the initial state: $$p_0 = \frac{V_{p0}}{V_0} = 1 - \frac{V_{f0}}{V_0} \tag{6.3}$$

at deformed state: $$p_0 = \frac{V_p}{V} = 1 - \frac{V_f}{V} \tag{6.4}$$

Since the volume of fibers does not change during compression,

$$V_f = V_{f0} \tag{6.5}$$

we have

$$\begin{aligned}(1-p_0)V_0 &= (1-p)V \\ p &= 1-(1-p_0)\frac{V_0}{V}\end{aligned} \tag{6.6}$$

The Eq. (6.1) is deduced from Eq. (6.6) for the relation between global longitudinal strains and the porosity as

$$p = 1-\frac{1-p_0}{\sqrt{2e_{zz}+1}} \tag{6.7}$$

Using positive value of strain, Eq. (6.7) becomes

$$p = 1-\frac{1-p_0}{\sqrt{1-2e_{zz}}} \tag{6.8}$$

Figure VI.6 illustrates experimental data fitted to Eq. (6.8).

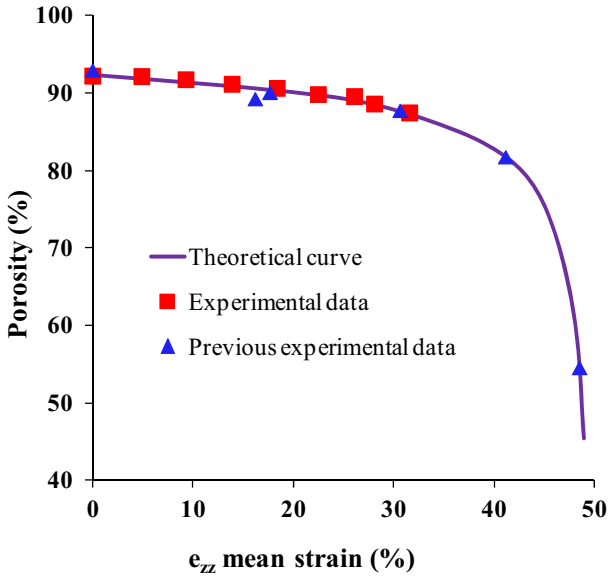

Figure VI.6: Theoretical and experimental curve E_{zz} mean strain vs. porosity [72], [80]

This result confirms once again that the transversal strain is negligible and there is no change of the sample section as expressed in Eq. (6.1). From this curve, we deduce that at 48.9% of compression strain (corresponding to 85% of small strain case), the pore volume fraction is 48.6% and the maximal fiber volume fraction is found about 51.4%.

VI.1.2 Relation between fibers and compressive behavior

a) Evolution of fiber diameters during compression using the granulometry by opening method

As we are able to segment wood fibers from PES fibers (section IV.2.3), we can now investigate the distribution and the evolution of fiber size during compression, the results are illustrated in Figure VI.7.

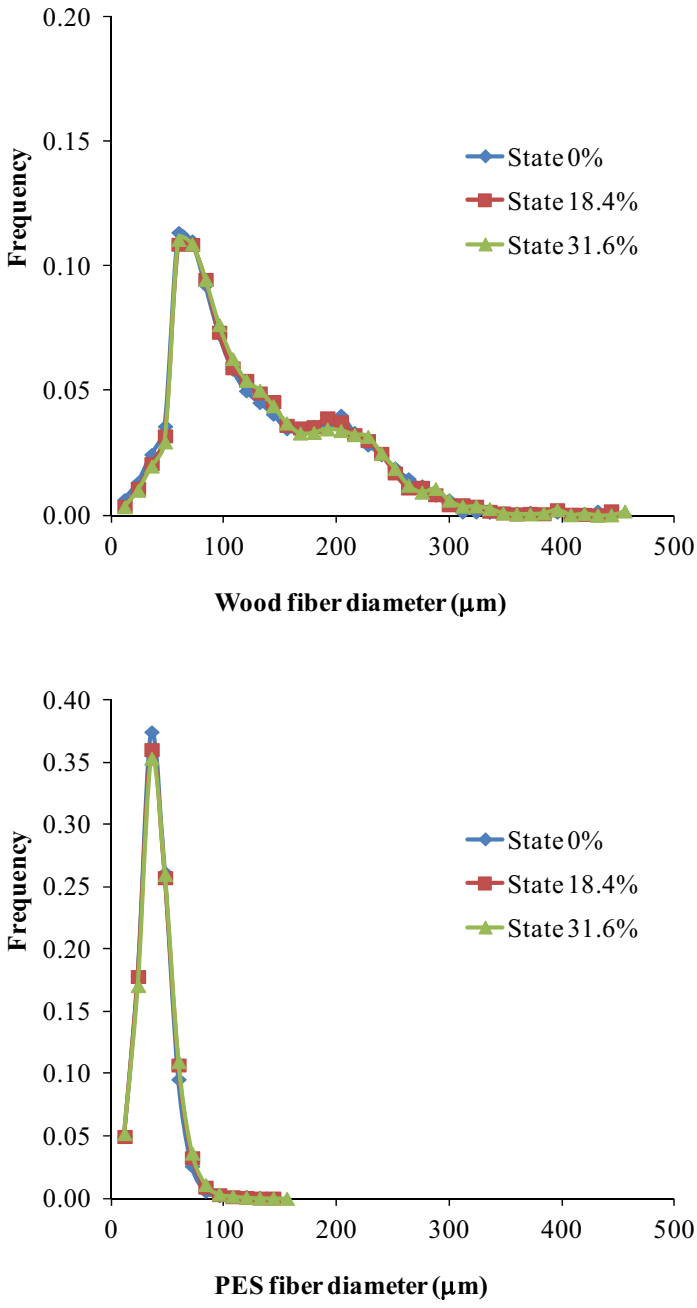

Figure VI.7: Granulometry of separated fiber network: wood network and PES network

The mean diameter of wood fibers and PES fibers are 137 and 40µm with respective standard derivation ±73.5 and ±14.6µm, which confirms the estimated diameter of PES fibers in paragraph IV.2.3 and agrees with results obtained in previous study [60]. Until the studied compression rate, we obtain the same granulometry of wood/PES fiber at all states (Figure VI.7), which shows that fibers do not collapse during the compression, so that only pores are excluded. The global deformation of the sample depends then essentially on the evolution of the pores and on the rearrangement of fibers.

b) Effect of fiber volume fraction on compressive behavior

Considering Van Wyk's model where the relation between applied pressure p and fiber volume fraction is expressed in Eq. (1.20) as $p = KE\left(f_v^3 - f_{v0}^3\right)$, KE is a constant depending on fiber properties other than fiber volume fraction. Fitting stress-strain relation of the material to Eq. (1.20) gives $KE = 4.4MPa$ (Table VI.3, Figure VI.8).

Table VI.3: Fiber volume fraction at different compression states obtained by DVC

Compression rate (%)	0	4.9	9.3	13.9	18.4	22.5	26.1	28.1	31.6
Stress (Pa)	0	362	755	1273	1808	2515	3332	4338	5785
Fiber volume fraction	0.077	0.078	0.082	0.088	0.093	0.101	0.104	0.113	0.125
$f_v^3 - f_{v0}^3$	0	0.00001	0.00009	0.00022	0.00034	0.00057	0.00065	0.00099	0.00148

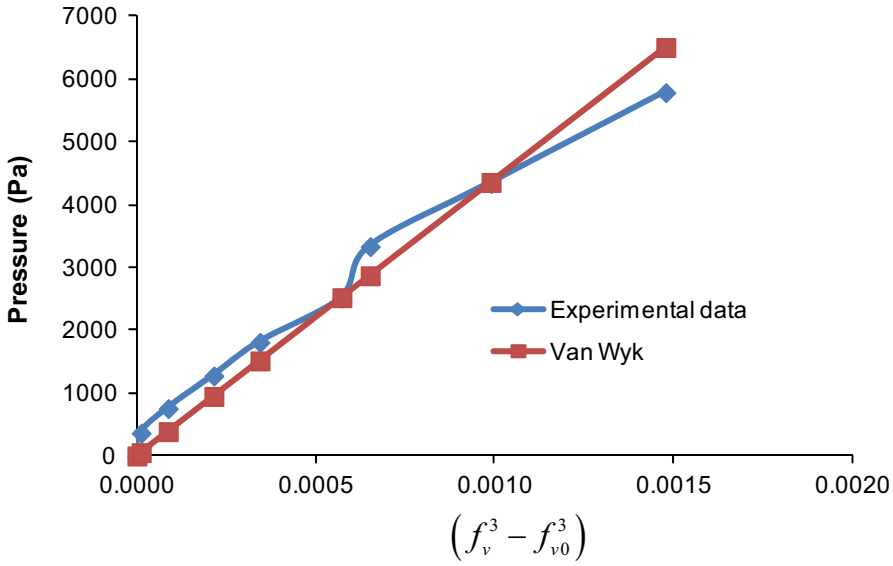

Figure VI.8: Fit of experimental data to Van Wyk's model

Considering Neckar's model: if we assume that the non-compressed volume deduced from compression test until maximum consolidation on the large sample corresponding to the excluded volume V_{ex} as in Eq. (1.15) with $V_{ex}=0.15V_0$ we find $KE = 2500Pa$ (Table VI.4, Figure VI.9).

Table VI.4:

Compression rate (%)	Stress (Pa)	$(V - V_{ex})$	$\left(\frac{V^3}{(V - V_{ex})^3} - \frac{V^3}{(V_0 - V_{ex})^3}\right)$
0	0	809290957	0.00
4.9	362	761056461	0.28
9.3	755	714919117	0.54
13.9	1273	670878925	0.77
18.4	1808	629984461	0.98
22.5	2515	588041421	1.18
26.1	3332	549244109	1.38
28.1	4338	506252493	1.59
31.6	5785	459066573	1.84

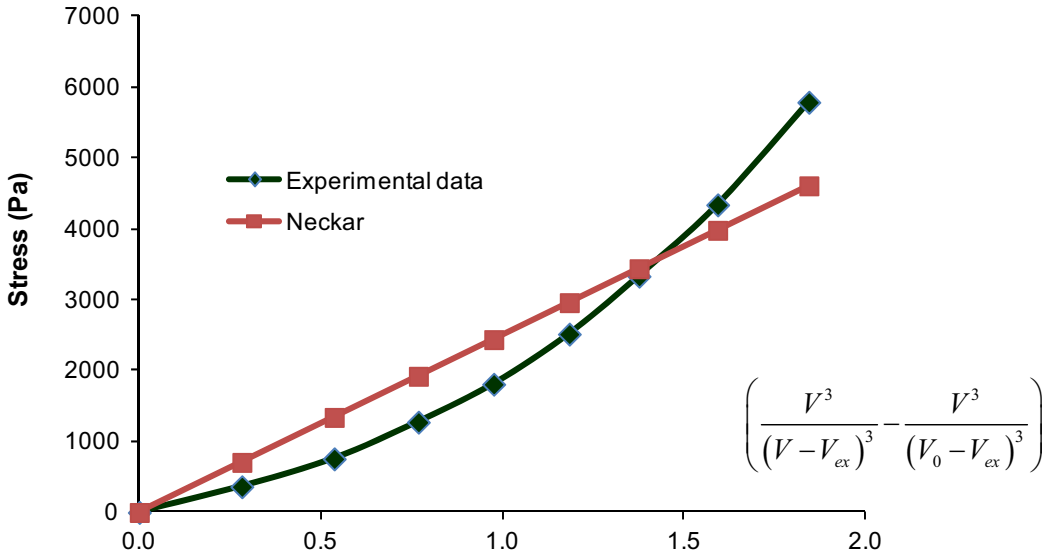

Figure VI.9: Fit of experimental data to Neckar's model

We may get a better correlation between experimental data and Neckar's model by modifying the power parameter into Neckar's model which is illustrated in Figure VI.10 so that:

$$p = KEV^{4.5}\left(\frac{1}{(V-V_{ex})^3}-\frac{1}{(V_0-V_{ex})^3}\right)^{1.5} \qquad (6.9)$$

We obtain in this case $KE = 2200Pa$.

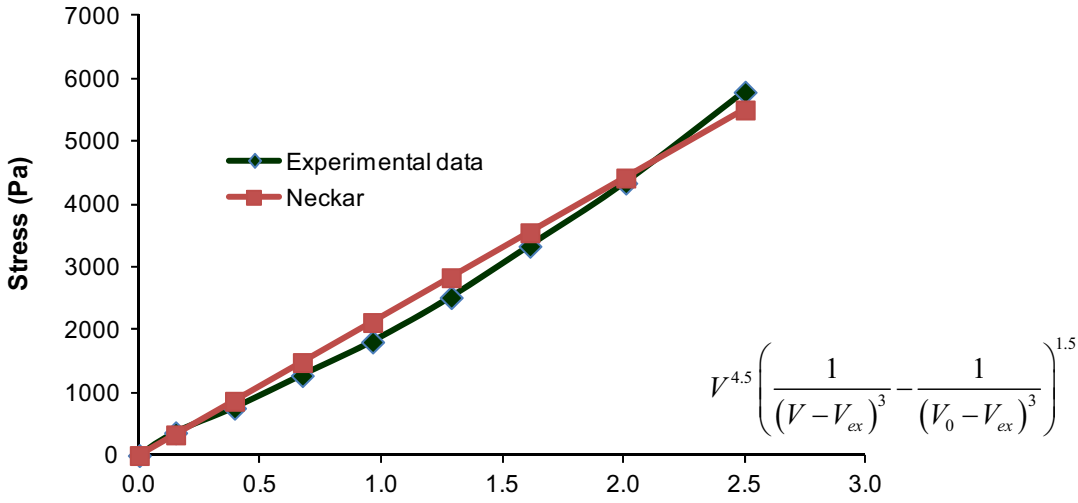

Figure VI.10: Fit of experimental data to modified Neckar's model

For all considered models, experimental data seem to best fit to Van Wyk's theory. As for Neckar's model, we may not estimate correctly V_{ex}. However, this

result demonstrates that the fiber volume fraction or porosity play a major role on the compressive behavior of the material.

c) Evolution of fiber orientation during compression

In order to investigate the evolution of fiber orientation, let's use a coordinate system in which the fiber orientation is defined by (φ,θ) as shown in Figure VI.11.

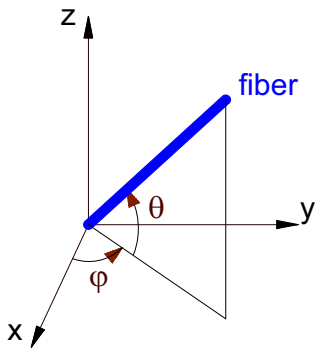

Figure VI.11: Notion of spherical coordinates

Figure VI.12 shows the distribution of local orientations measured at each voxel of the fiber network following thirteen predetermined orientations. As the fibers are not straight, fibers are considered to contain several straight segments of different orientations. We study in total thirteen orientations which are: (0,0), $\left(0,\frac{\pi}{4}\right),\left(0,\frac{\pi}{2}\right),\left(0,\frac{3\pi}{4}\right),\left(\frac{\pi}{4},0\right),\left(\frac{\pi}{4},\frac{\pi}{4}\right),\left(\frac{\pi}{4},\frac{3\pi}{4}\right),\left(\frac{\pi}{2},0\right),\left(\frac{\pi}{2},\frac{\pi}{4}\right),\left(\frac{\pi}{2},\frac{3\pi}{4}\right),\left(\frac{3\pi}{4},0\right),$ $\left(\frac{3\pi}{4},\frac{\pi}{4}\right),\left(\frac{3\pi}{4},\frac{3\pi}{4}\right)$. The fiber segments, whose own orientation is different from the thirteen pre-determined ones, will be given a new orientation that is the closest to the fiber own orientation. For the entire studied network, there are four orientations: (0,0), $\left(\frac{\pi}{4},0\right)$, $\left(\frac{\pi}{2},0\right)$, $\left(\frac{3\pi}{4},0\right)$ in plan perpendicular to the loading direction which occupy more than 70% of all networks with equivalent frequencies and have the tendency to increase during compression. This fact shows that the material is transversally isotropic. Almost all other orientations have the tendency to decrease when the material is more compressed.

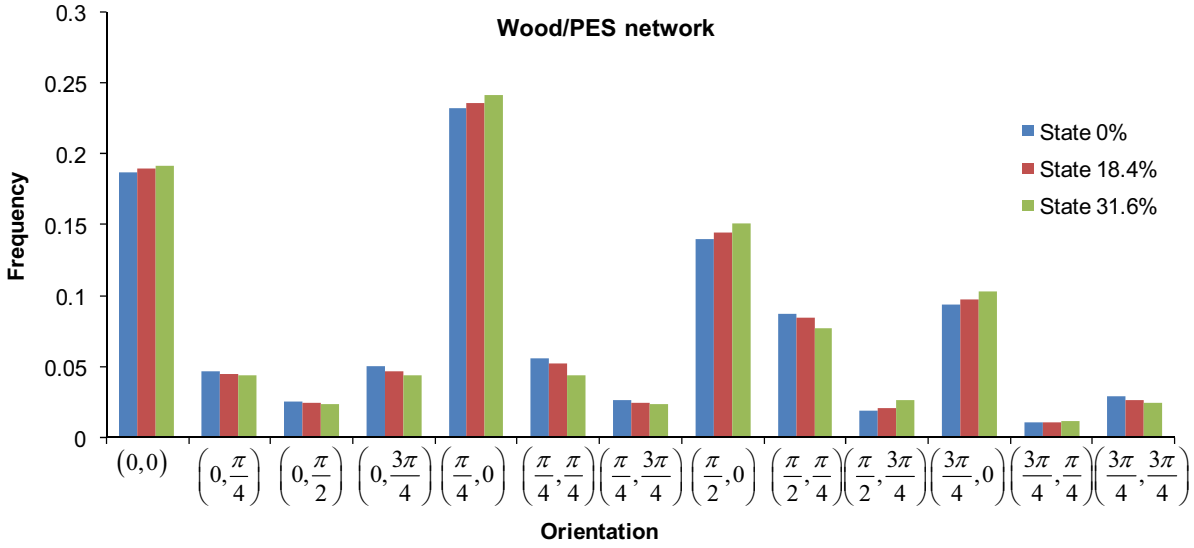

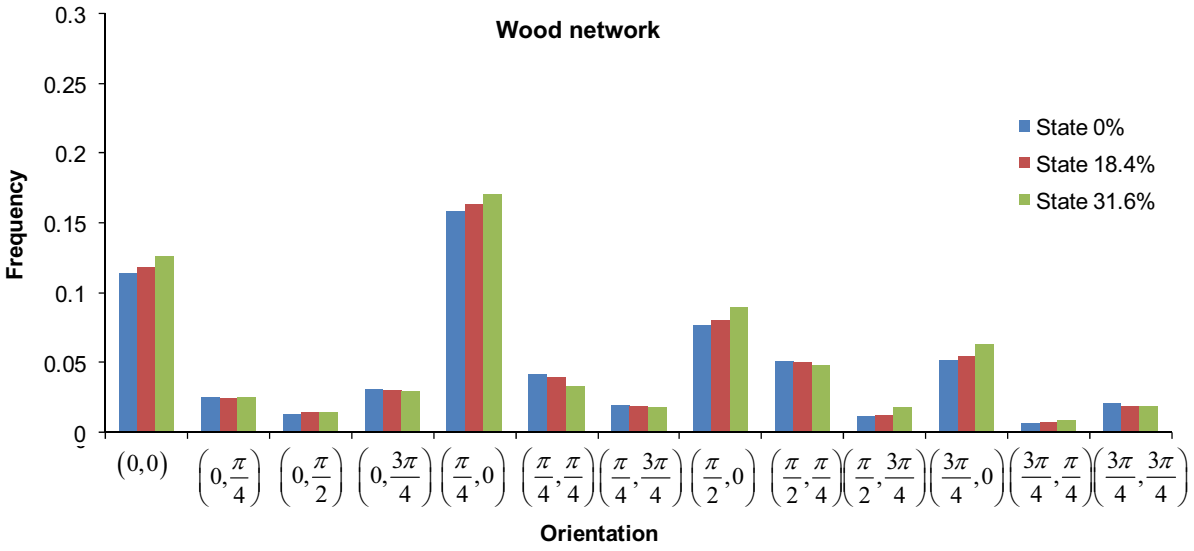

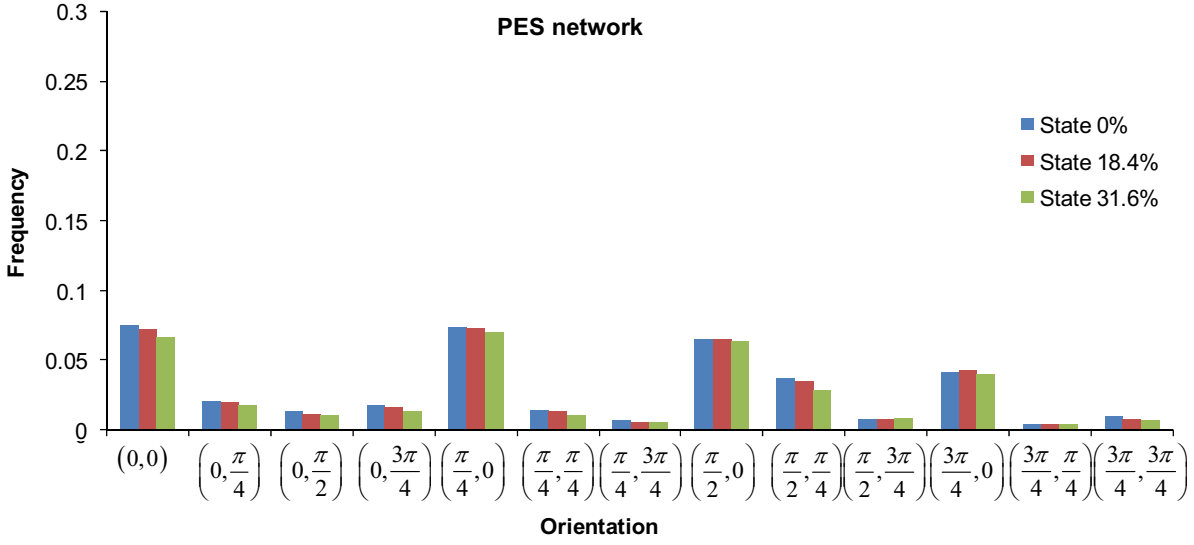

Figure VI.12: Evolution of local orientation in wood/PES network, wood network and PES network

3D renderings of the five privileged orientations are presented at the initial state for the whole fiber system: four orientations in plan as shown in Figure VI.13 (Since the wood network or the PES network gives the same tendency). We observe that the distribution of fibers in one privileged orientation family is really uniform and homogeneous in the whole sample volume. Moreover, it is essentially distributed in the transversal section, the fiber configuration is rather orthogonal, perpendicular to the loading direction and favourable under compressive solicitations.

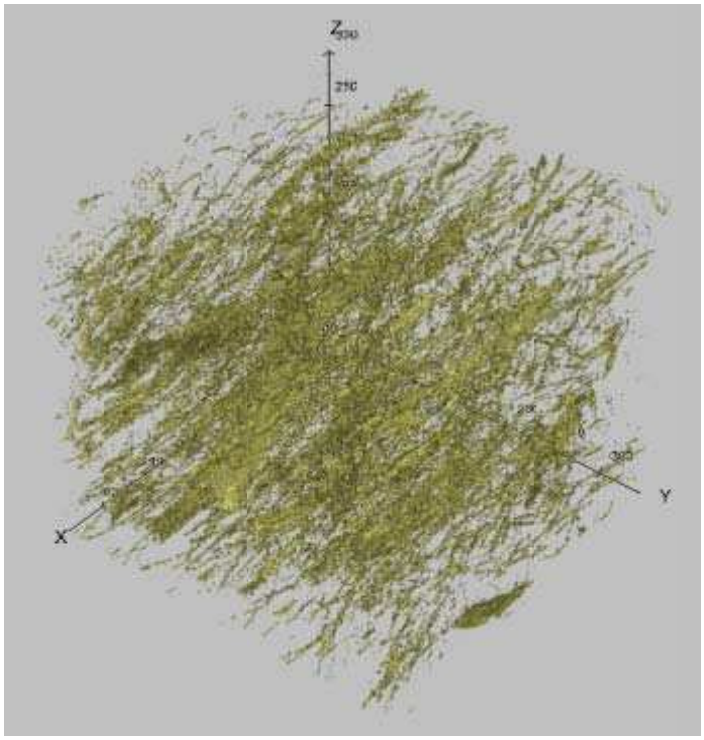

(a)

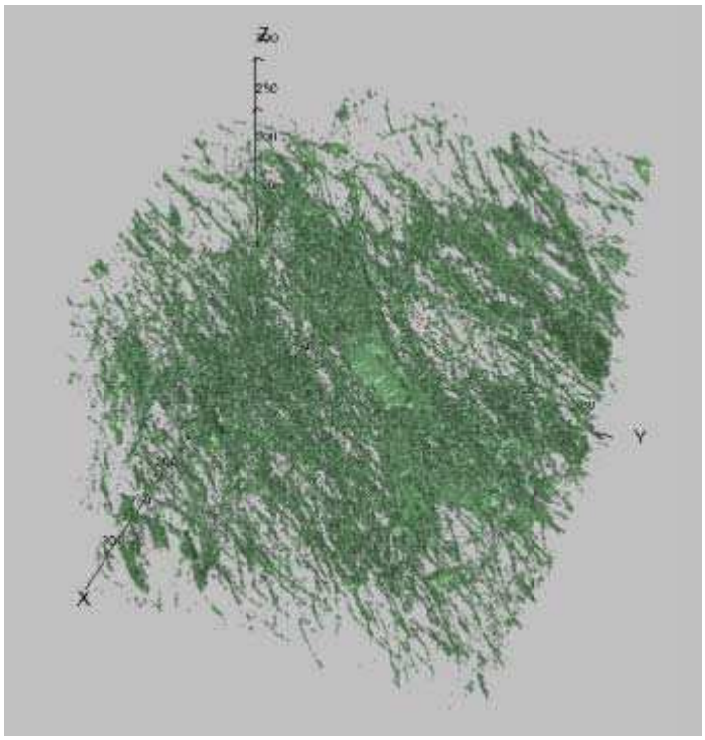

(b)

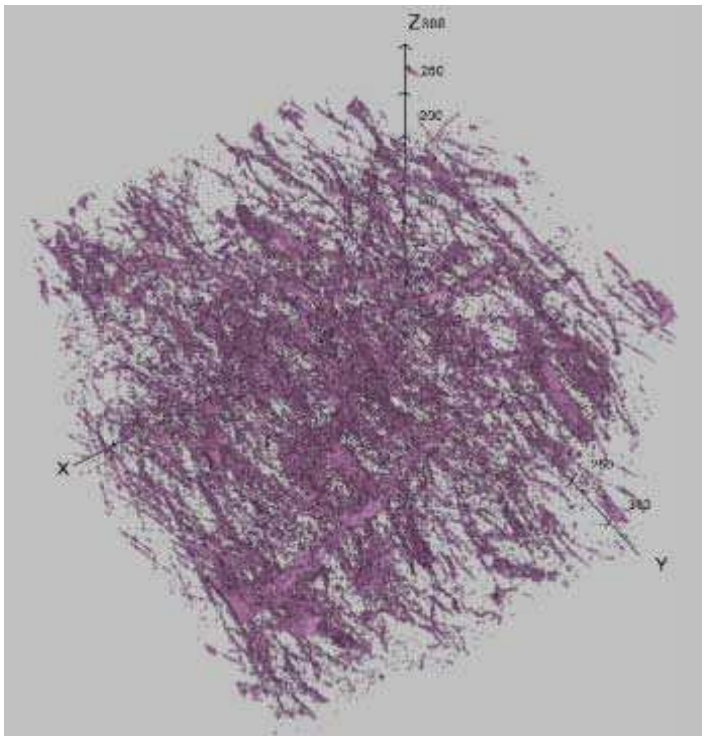

(c)

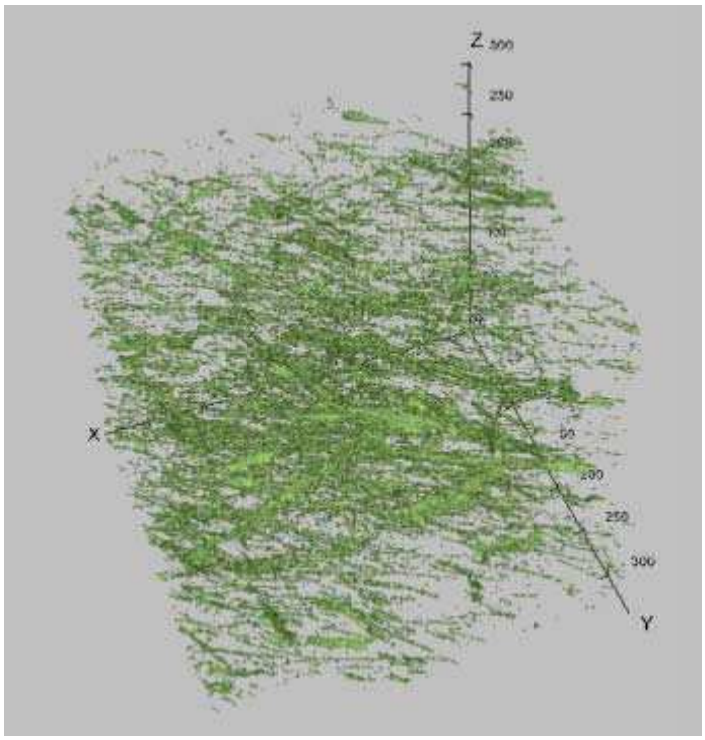

(d)

Figure VI.13: Spatial distribution of four privileged orientations in plan (θ=0) in wood/PES network

VI.2 The relation between local strain field and microstructure

This study allows us to better understand strain micromechanisms in this heterogeneous fibrous material. Under compression loading, the fibers have a vertical movement: transversal and shear deformations are negligible compared to strains in the compression direction. The same kinematics visible in 2D on the surface of the sample is measured in 3D in the bulk of the material.

We wonder at the scale of DVC, how local microstructure influences the behavior of the local point? Firstly, we will define the microstructure at the microscopic scale.

Considering a grid point (red point in Figure VI.14) which is passed by three crossed vectors, DVC gives the strain of this point by calculating the deformation of these three vectors and at the initial state, the strain is considered homogenous for the cube formed by these three vectors. In fact, we are interested in the microstructure changes of this cube during compression. As the strain is calculated, normally, we should determine the microstructure of the real deformed cube. However, extraction of the deformed cube from three deformed vectors is rather complicated. Plus, our current image analysis software does not allow us to perform morphological analysis on a non-rectangular cube. We propose a simple

method: from the studied cube passing through from points 1 to 8 which are also correlation grid points, we can easily find these points in deformed state using DVC. We will find an approximated rectangular cube whose minimum and maximum boundaries are the mean coordinates of these eight points in three directions (Figure VI.14). At the initial state, the size of the cube is twice the distance between grid points. The structural measurement at the local scale will be the one determined from this rectangular cube at different compression states.

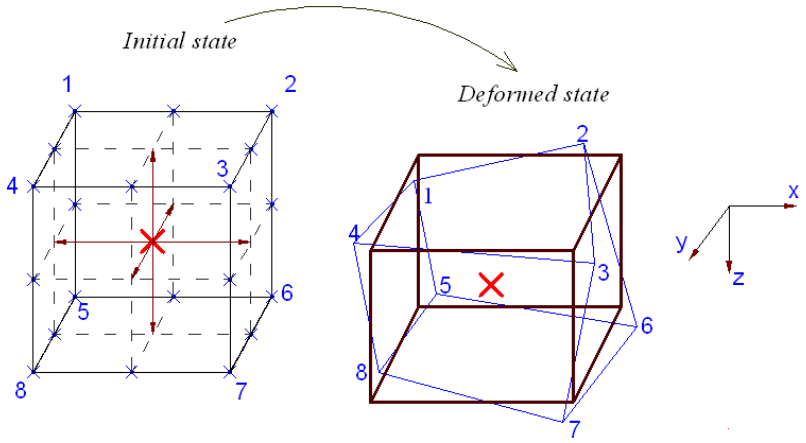

Figure VI.14: Idealized sub-volume at the initial state and deformed state based on correlation grid points

The minimum and maximum coordinates in x direction of the deformed cube is defined as

$$x_{c,\min} = \frac{x_1 + x_4 + x_5 + x_8}{4}$$
$$x_{c,\max} = \frac{x_2 + x_3 + x_6 + x_7}{4} \qquad (6.10)$$

where x_i is the x-coordinate of point i and in the same way we have in y and z directions:

$$y_{c,\min} = \frac{y_1 + y_2 + y_5 + y_6}{4}; \quad y_{c,\max} = \frac{y_3 + y_4 + y_7 + y_8}{4}$$
$$z_{c,\min} = \frac{z_1 + z_2 + z_3 + z_4}{4}; \quad z_{c,\max} = \frac{z_5 + z_6 + z_7 + z_8}{4} \qquad (6.11)$$

The next question is: do we study the microstructure at $(i\text{-}1)^{th}$ state or at i^{th} state corresponding to the local strain field at i^{th} state? There is a mutual relation between strain and microstructure: microstructure changes due to strain and the order of magnitude of the strain depends on how microstructure changes, in other saying,

microstructure modifications are the cause but also the result of the strain. In this study, two cases are studied: microstructure at $(i-1)^{th}$ state is used to predict the mechanical behavior at i^{th} state in case of numerical simulation [84] in the next paragraph and microstructure at i^{th} state is related to strain field at the same state.

At the local scale, as one can predict, not only the strain field but also microstructural properties are quite heterogeneous. That is why data at this scale will be studied under the form of probability distribution functions. The porosity at the local scale p_l is defined as

$$p_l = \frac{V_{p,l}}{V_l} \tag{6.12}$$

where $V_{p,l}, V_l$ are the volume of pore and total volume of correlation zone. $V_{p,l}, V_l$ evolve during compression.

Note that the superposition of the local strain and the microstructure takes place in 3375 grid points or 3375 sub-volumes. In the following sections, we will observe the evolution of fiber diameters and fiber orientation at the local scale during compression.

a) Evolution of fiber diameters at the microscopic scale during compression

The relation between the local strain and the fiber mean diameters measured for sub-volumes at the two strain states 18.4% and 31.6% is plotted in Figure VI.15. There is no correlation between these two parameters.

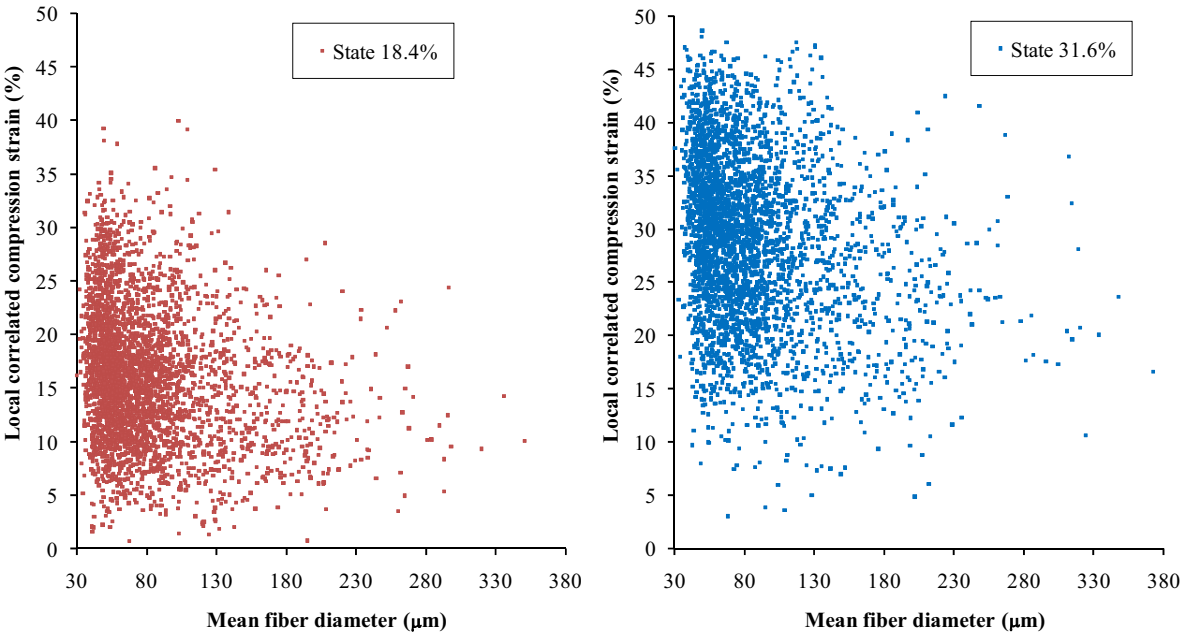

Figure VI.15: Relation inverse mean fiber diameter – Local strain at two states (a) 18.4% and (b) 31.6%

For more detail, Figure VI.16 illustrates the evolution of fiber diameter (including wood and PES fibers) of some local sub-volumes corresponding to sub-volumes used to calculate strain in DVC. Chosen sub-volumes are distributed all over the sample. We find that the distribution of fiber diameter differs clearly from one sub-volume to another but does not change for each sub-volume during the compression, as observed previously at the global scale. This result shows that fiber diameter is not a major parameter that influences material behavior even at the local scale.

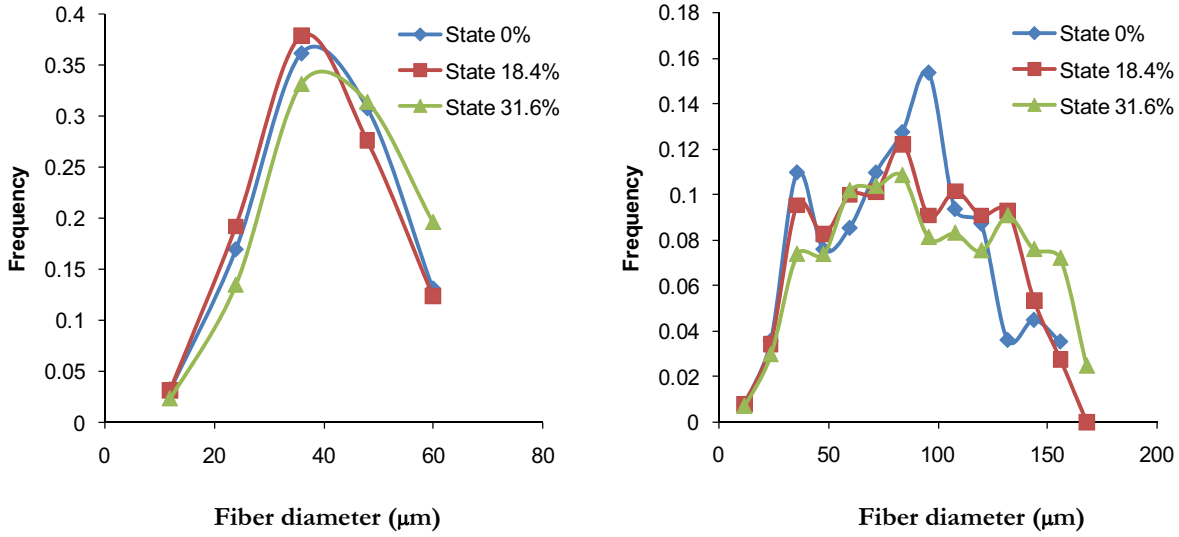

(a) Sub-volume 1

(b) Sub-volume 500

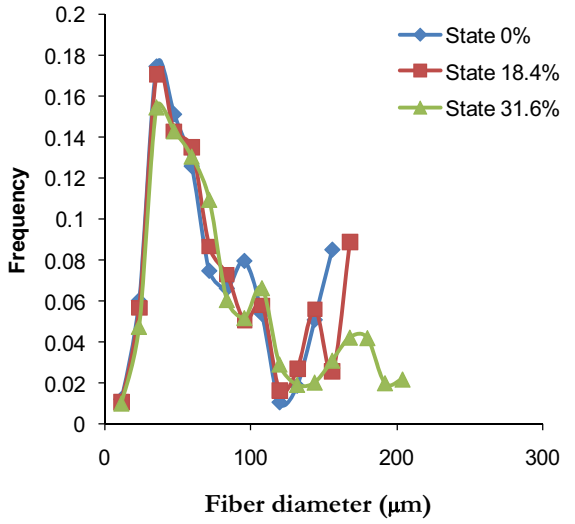

(c) Sub-volume 1000

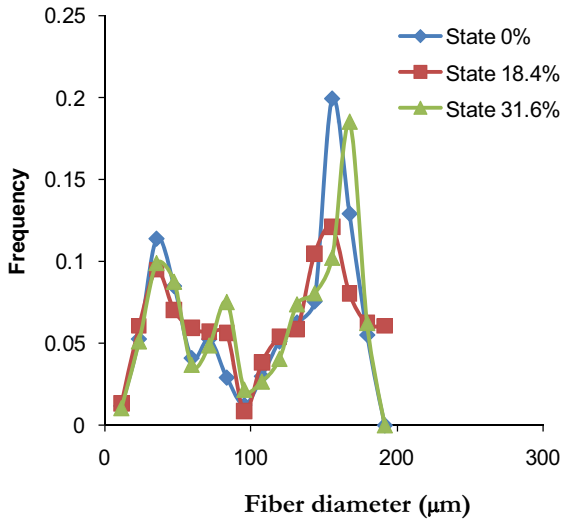

(d) Sub-volume 1500

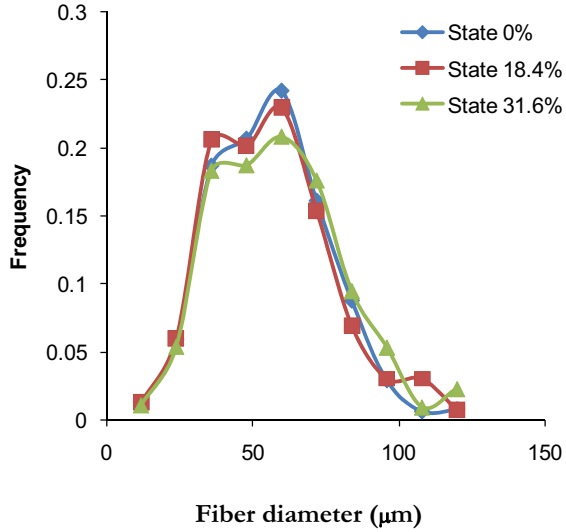

(e) Sub-volume 2500

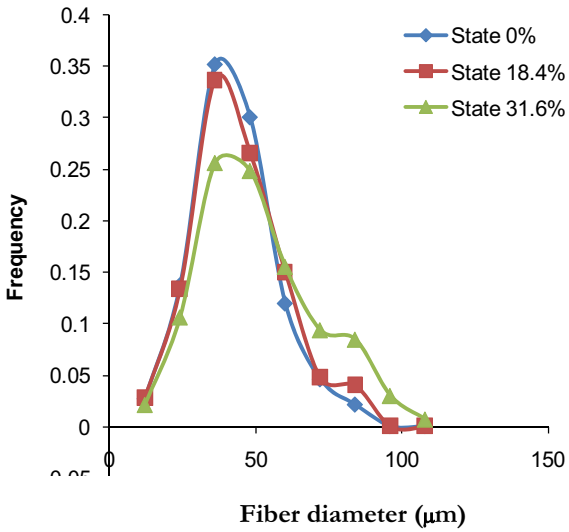

(e) Sub-volume 3000

Figure VI.16: Distribution of fiber size at three compression states in different local sub-volumes

b) Evolution of fiber orientation at the microscopic scale during compression

The same result is obtained with the local orientation of fibers: each sub-volume has its own evolution of local orientation which is different from that of other sub-volumes but changes are insignificant under compression loading (Figure VI.17). This result could be easily predicted as the variation of orientation distribution of fibers in the whole sample can be ignored (Figure VI.12). Furthermore, as observed in Figure IV.13, there is very small variation of wood fiber orientations, so the orientation variation of the whole system is essentially caused by the orientation variation of PES fibers because of its strong flexibility. However, the size of the studied correlation domain is much greater than the

diameter of PES fibers; consequently, we are not able to detect small orientation variation of PES fibers. Moreover, we must take into account the fact that the number of studied fiber orientations is limited, which required to increase the orientation number in a more local study. However, there may existe some sub-volumes that do not respect the aforementioned tendency, i.e. sub-volumes 2500 and 3000 in Figure VI.17c, d.

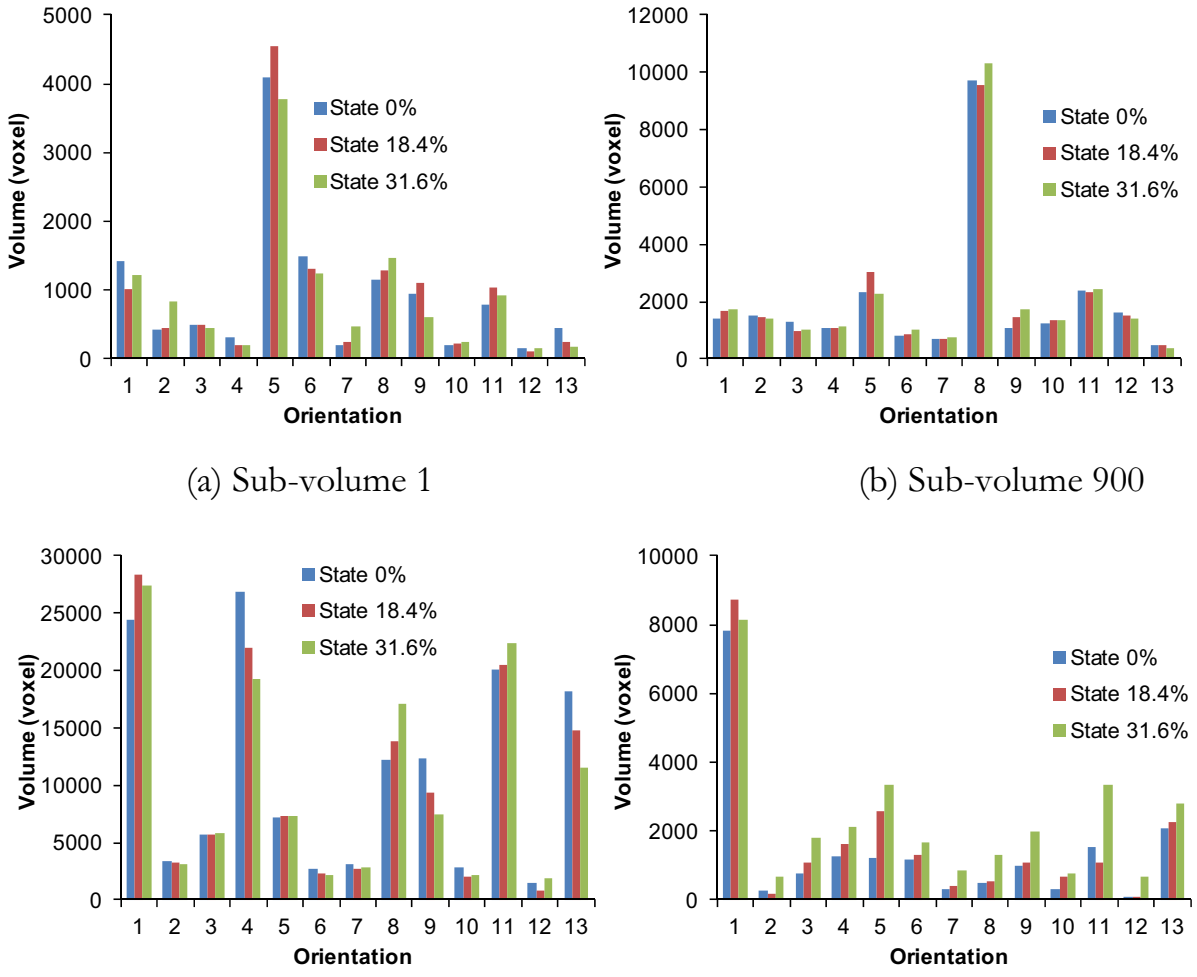

(a) Sub-volume 1

(b) Sub-volume 900

(c) Sub-volume 2500

(d) Sub-volume 3000

Figure VI.17: Variation of local orientation of fibers in different sub-volumes at three compression states. Notion of orientation in (φ,θ) as: 1 (0, 0), 2 (0, π/2), 3 (0, 3π/4), 5 (π/4, 0), 6 (π/4, π/4), 7 (π4, 3π/4), 8 (π/2, 0), 9 (π/2, π/4), 10 (π/2, 3π/4), 11 (3π/4, 0), 12 (3π/4, π/4), 13 (3π/4, 3π/4)

c) Effect of pore and fiber distribution on local strain field

The previous analyses on fiber diameters and orientation show that the deformation of fibrous assemblies may be are essentially governed by the variation of fiber volume fraction, which is directly related to pore size: the strain has the

tendency to be proportional to the fiber volume fraction. We have already seen this conclusion at the global scale in Van-Wyk's or Neckar's theory, and in experimental approaches of many researchers: the role of fiber diameter and fiber orientation, including fiber contacts etc. is then represented by a constant coefficient.

Figure VI.18 shows at the two strain states 18.4% and 31.6% that there is not a linear relation between local strain and local porosity as shown by Figure VI.18 for mean strains smaller than 35%.

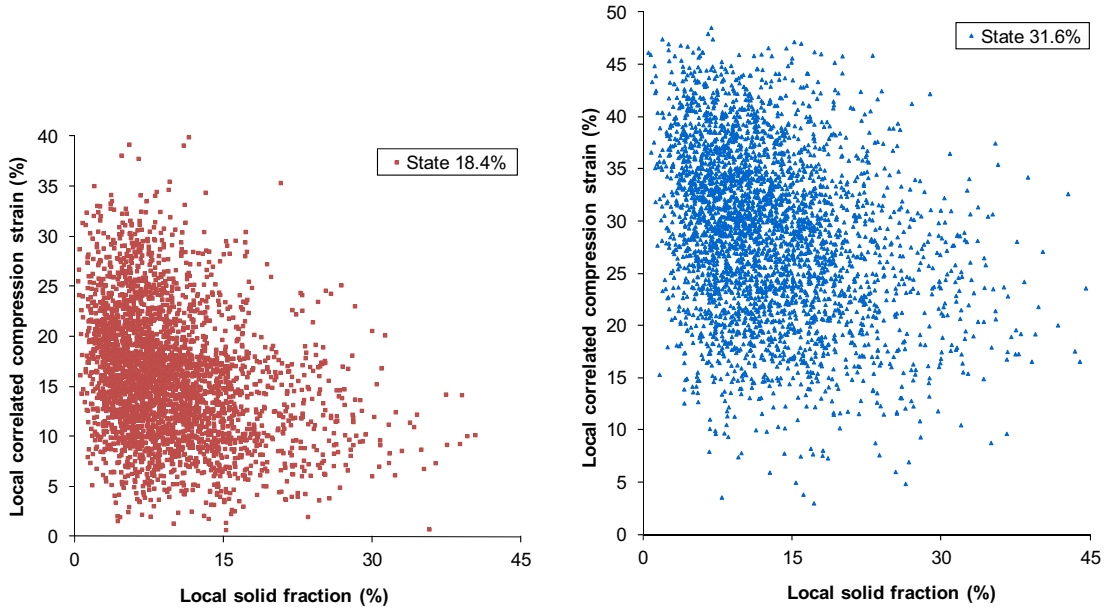

(a) State 18.4% (b) State 31.6%

Figure VI.18: Relation Local solid fraction – Local strain at two states (a) 18.4% and (b) 31.6%

Considering then the variation of strain and porosity along the sample height, mean value is calculated for each assembly of observation points which lie in the same grid plane (slice (x, y)). The thickness of slices is equal to 120 voxels for the initial state. Strain in these slices is plotted in relation to the volume fraction of the material's solid phase (Figure VI.19a) and wood or PES phase (Figure VI.19b). In comparison with Figure VI.18, we observe in Figure VI.19a the tendency of local strains to increase when the initial solid volume fraction decreases. It means that the size of mechanical REV is smaller than the size of the sample but must be larger than the size of sub-volumes. This relation shows that solid fraction seems to play a major role on local material behavior, in particular wood fraction (Figure VI.19b). Indeed volume fraction of PES fibers is quite constant along the sample thickness contrary to that of wood fibers.

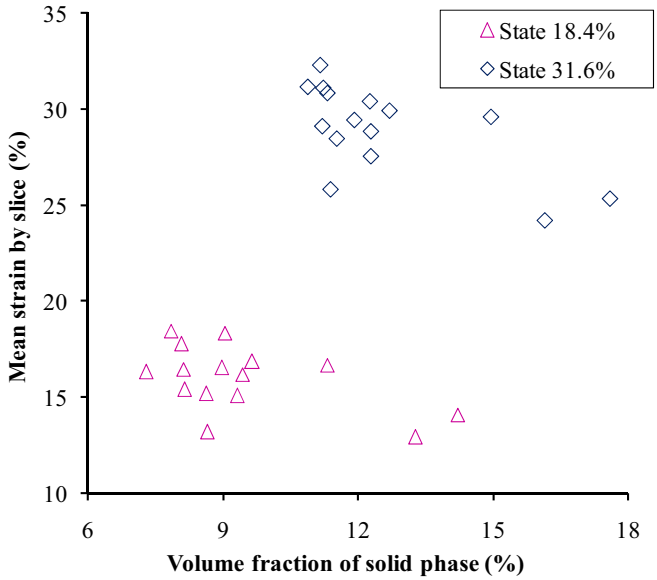

(a)

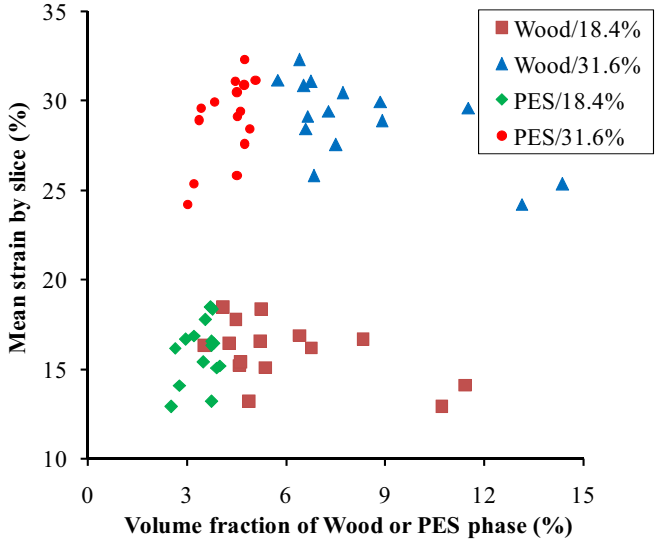

(b)

Figure VI.19: Relation between mean strain and mean volume fraction of solid phase (a) and wood or PES phase (b) for several slices along the sample height

d) Superposition of 3D microstructure with Ezz strain field

Now we will be interested in the evolution under loading of the microstructure superposed with *Ezz* strain field, we observe always the same fibers in a vertical slice and no other fibers which may appear from another slice. Figure VI.20 shows the superposition of wood fibers with *Ezz* strain for the slice 320 parallel to the compression axis. With compression, fibers get closer but the evolution of the pores is not uniform in the whole sample.

As the microstructure is complex, the localization of strain is linked to the spatial arrangement of fibers. A superposition of local strain field with microstructure will allow us to better understand the tendency mentioned in Figure VI.18 and Figure VI.19. Figure VI.20 which depicts the superposition of wood fibers and strain field shows a weak correlation between the presence of wood and level of strain. Indeed all areas of small strains do not correspond to zones with wood fibers. Figure VI.21 which shows the superposition of local wood thickness and normalized E_{zz} strain field gives the same tendency.

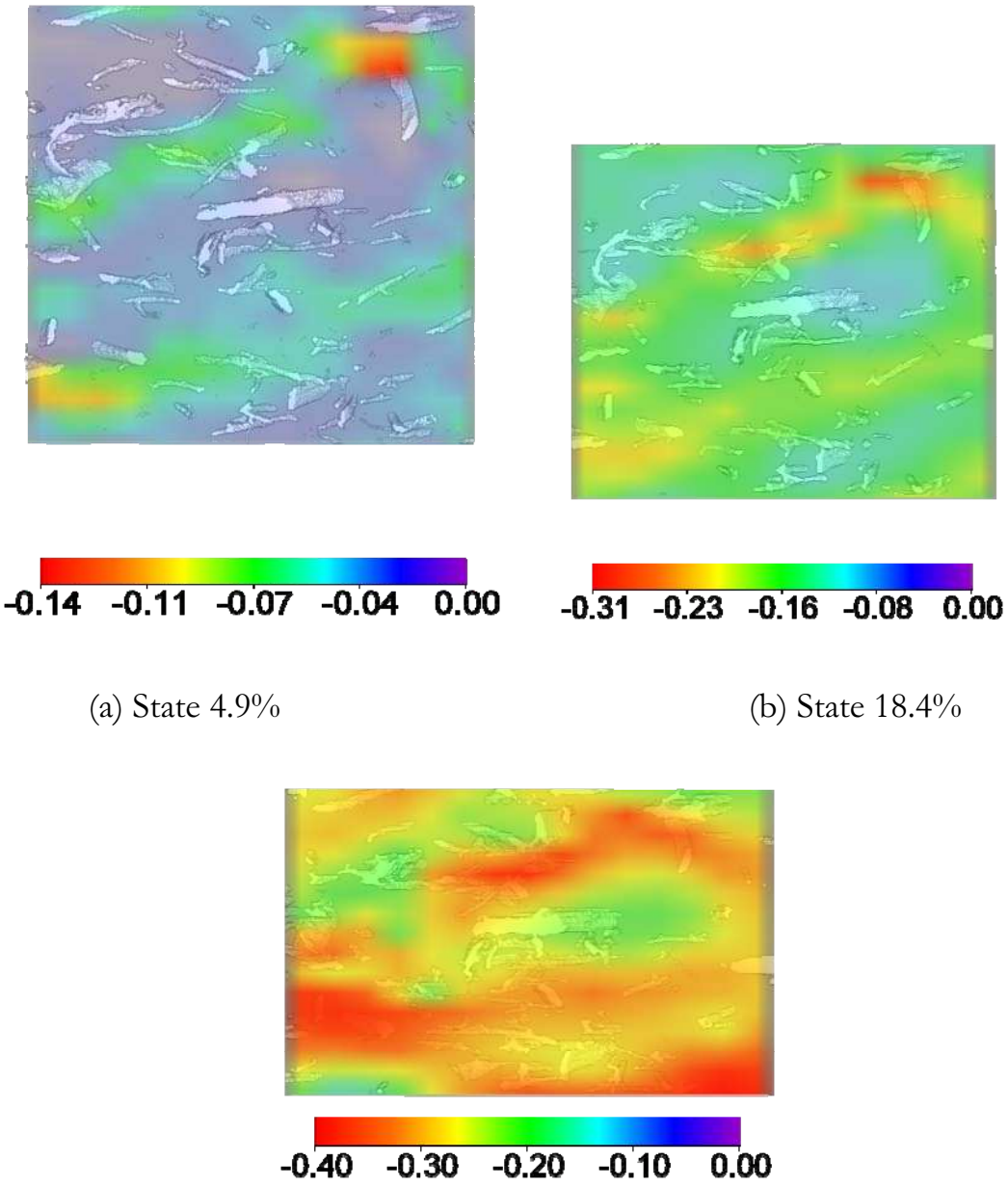

(a) State 4.9%

(b) State 18.4%

(c) State 31.6%

Figure VI.20: Superposition of wood fibers with Ezz strain for slice 320 parallel to the compression axis

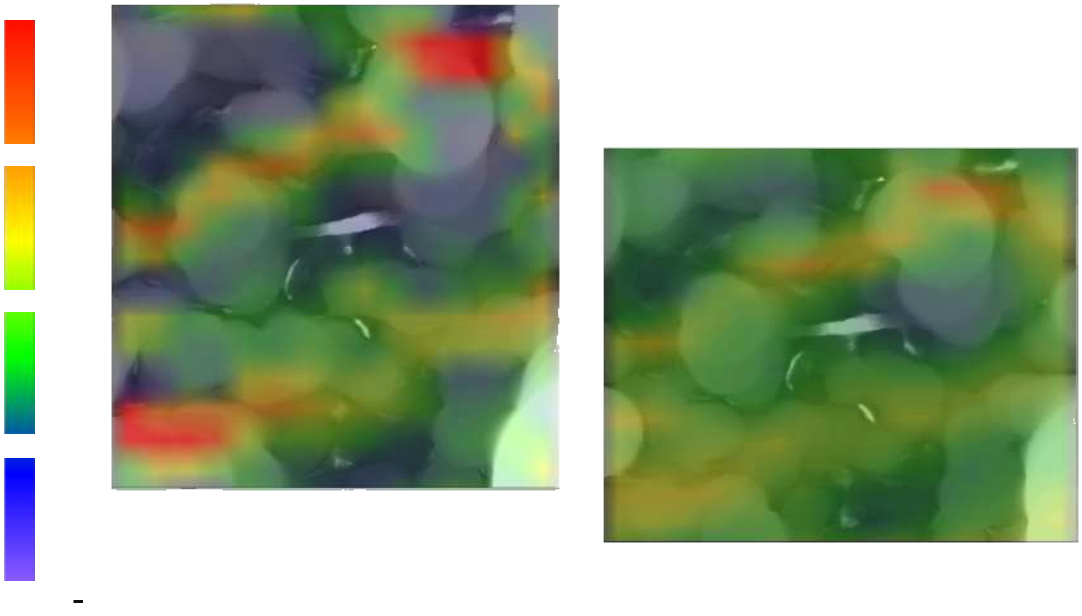

(a) State 4.9% *(b) State 18.4%*

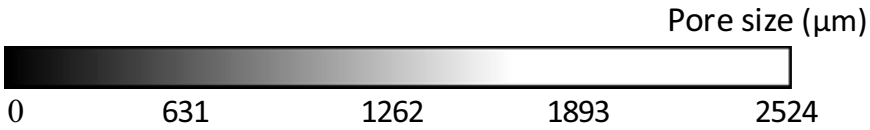

(c) State 31.6%

Figure VI.21: Superposition of local wood thickness with normalized Ezz strain for slice 320

By adding PES fibers (Figure VI.22), in comparison with Figure VI.20, the correlation is better. We can observe that the deformed areas, i.e. the less resistant areas, correspond to zones where porosity is higher (Figure VI.23). At first states of strains (small imposed strains), the porous zones with a bigger size are much more deformed than those of a smaller size. Then the more the material is deformed and the more the dimensions of the pores become close. This local analysis confirms the trends on Figure VI.2 (statistical analysis) where the distribution of pore sizes

decreases when imposed Ezz increases and on Figure V.36 where the material becomes more homogeneous when compressed. The size of pores being reduced, the material is hard to deform what is described by a nonlinear mechanical behavior with a rigidifying effect (Figure V.13).

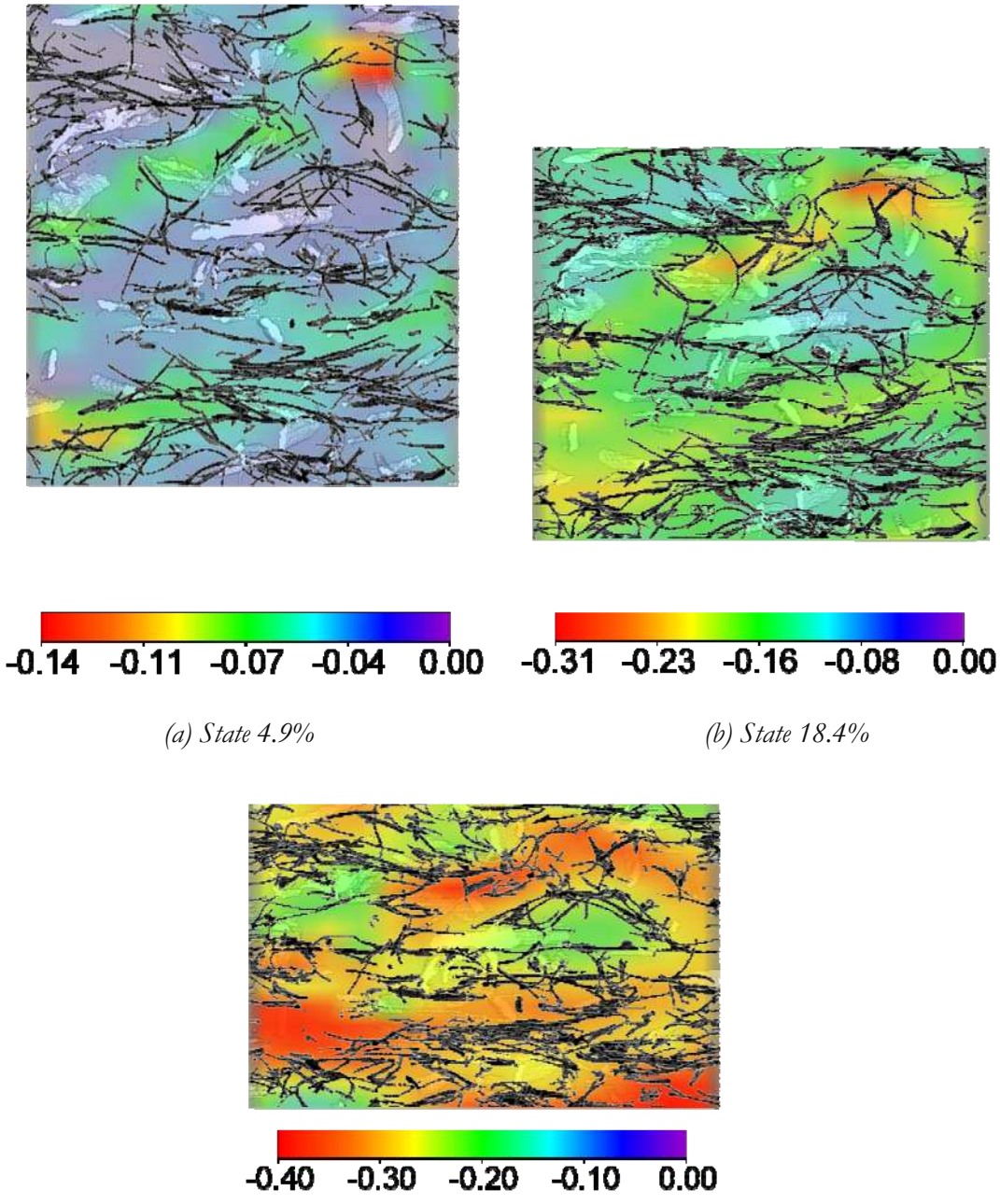

(a) State 4.9% *(b) State 18.4%*

(c) State 31.6%

Figure VI.22: Superposition of the microstructure (white = wood, black = PES) with Ezz strain for slice 320 parallel to the compression axis

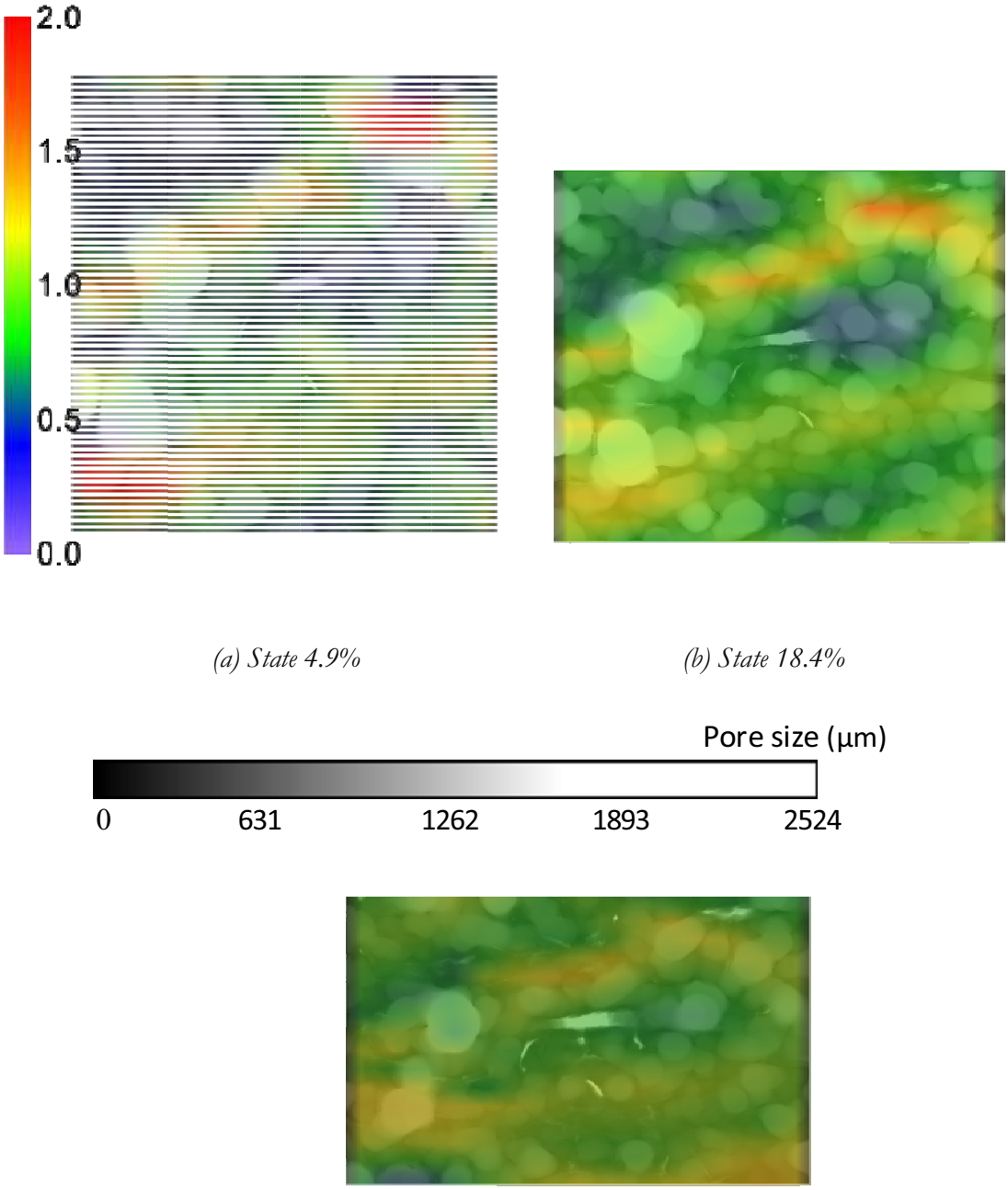

(a) State 4.9%

(b) State 18.4%

(c) State 31.6%

Figure VI.23: Superposition of wood/PES local thickness with normalized Ezz strain for slice 320

However we can observe that some zones with high porosity are not or much less deformed. Figure VI.24 shows these zones which have the smallest strains (less than 2.6%, 13%, 24.5% and at the state 4.9%, 18.4% and 31.6% respectively). These areas distributed in the whole volume (Figure VI.25) correspond to a particular arrangement of fibers which constitutes an incompatibility of vertical movement of the wood fibers and creates a more rigid local structure.

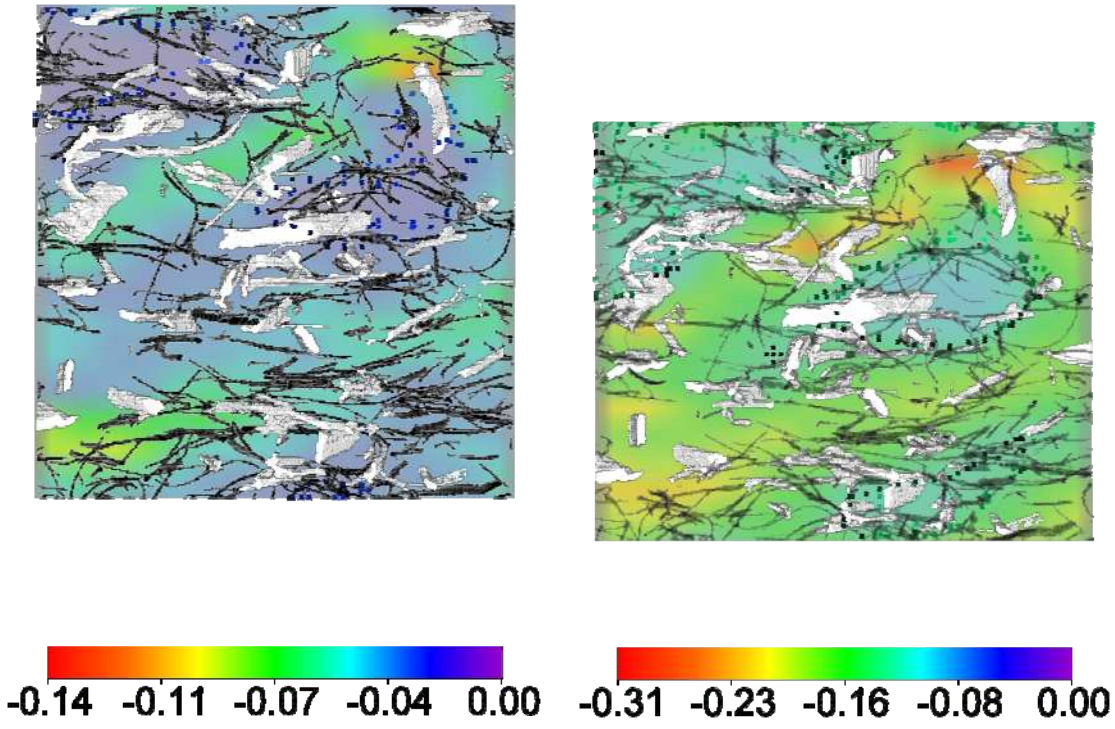

(a) State 4.9% *(b) State 18.4%*

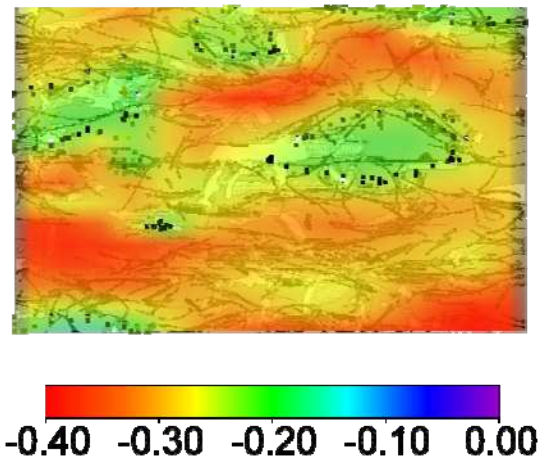

(c) State 31.6%

Figure VI.24: Superposition of the microstructure (white = wood, black = PES) with Ezz strain for slice 320, dashed lines represent less deformed zones

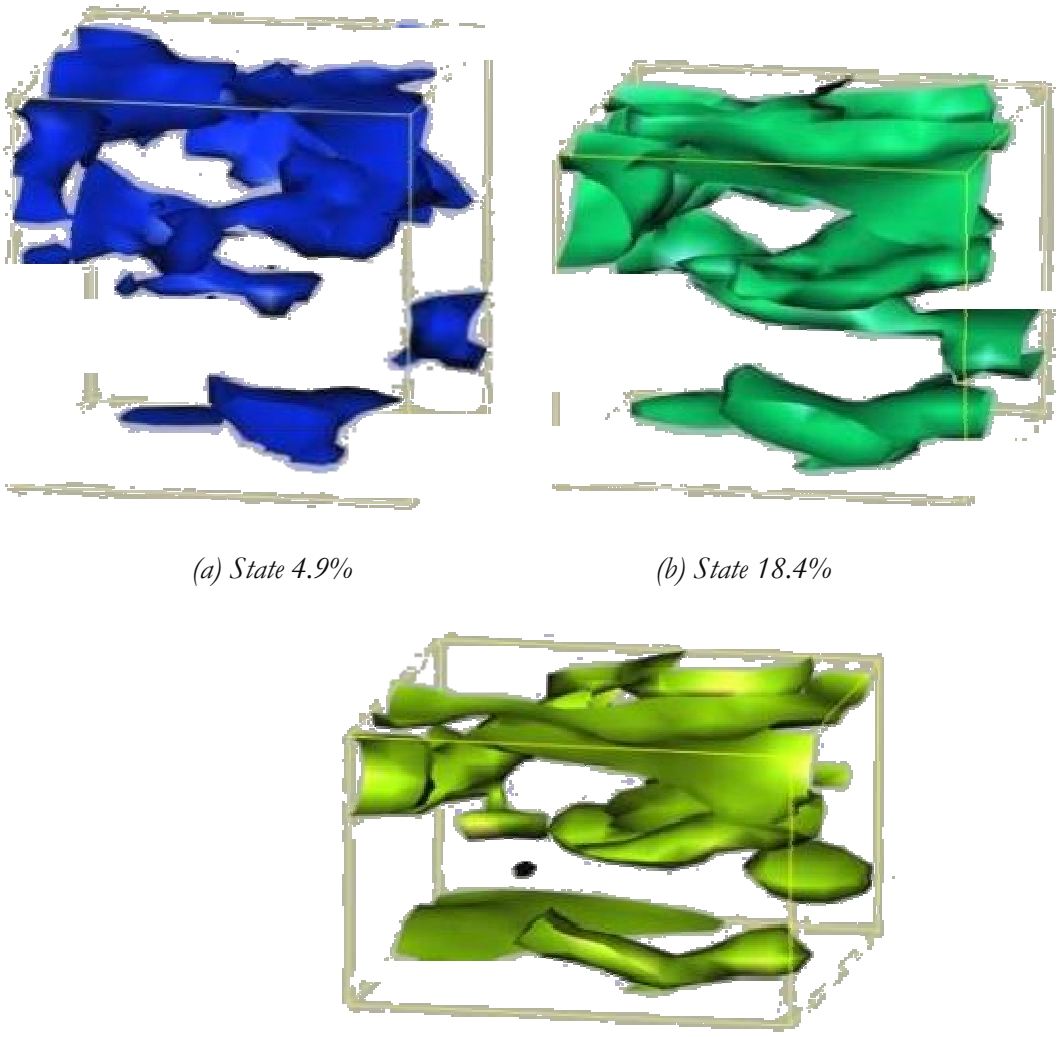

(a) State 4.9% *(b) State 18.4%*

(c) State 31.6%

Figure VI.25: Spatial distribution of more rigid areas

In conclusion, among studied microstructural properties, the mechanical response of this fibrous material under compression is principally ruled by local volume fraction of voids for the studied range of loading (0 to 30%). Then the knowledge of void geometry is almost sufficient to predict the behavior. The spatial arrangement of fibers (orientation, shape, contact…) and rigidity of fibers (for example bending rigidity) seem to have a local influence in some areas of the sample volume and a weak contribution towards mechanical behavior in compression at these levels of strain. However, there are still local areas whose behavior cannot be only explained by void characteristics, which demands further studies on other microstructural properties such as the evolution of the number of contacts between the fibers during the compression. In an attempt to obtain the contact fibers, we are able to extract contacts in the PES network by skeletonization but not yet in the wood network because of its complex geometry.

We would like to put the study of fiber contacts on the material behavior as a short-term perspective.

VI.3 Comparison between DVC displacements and displacements obtained by Cast3M

In this chapter, a numerical simulation is proposed in order to study the relationship of the mechanical behavior between the small and the global scales through the microstructural properties. An assumed relation of Young's modulus at these two scales is proposed based on preceding results (From Eq. (6.10) to Eq. (6.13)). The simulation is integrated into Cast3M, which is a code of calculation based on the finite element method and developed by the Département de Mécanique et de Technologie (DMT) of Commissariat français à l'Energie Atomique (CEA) [85]. Our main objectives in this subsection are to:

- Develop a simple simulation methodology for material behavior based on microstructure properties of the network.

- Validate this relation through the difference minimization of node displacements obtained by DVC and by simulation.

This methodology takes into account the role of local fiber volume fraction in order to reveal its influence on the global behavior. The simplest way is to use the same nodes as the DVC ones whose detail is presented above so that it can be easily related to the experimental results. The relation between mechanical behaviors at the macroscopic and the microscopic scales is characterized by making the ratio of node displacements by DVC and by Cast3M as the closest as possible to the unity value.

VI.3.1 Input parameters for Cast3M simulation

Numerical simulation uses the same system of points as DVC, which is totally included in chosen morphological volumes (908voxels as initial thickness at resolution of 6μm). The system contains 3375 nodes and creates 2744 elements of size 60x60x60voxels or 0.036x0.036x0.036mm^3 at the initial state (Figure VI.26). In total, the analyzed sample in Cast3M has the size of 840x840x840voxels or 5.04x5.04x5.04mm^3. At the global scale, until the tested compression rate, the sample still exhibits quasi-elastic behavior. So at the smaller scale, for simplification, we will also assume that the behavior of each finite element is linear elastic and the elasticity is not the same between elements. We initially model the bottom layer which is totally restrained while lateral surfaces have no deformation restriction, as

the studied sample is extracted from inside the real sample. Two parameters must be given into the simulation in the elastic model. Firstly, the Poisson coefficient: in Cast3M, we will impose a null value of Poisson coefficient for all compression states. Secondly, Young's modulus of each element (we will call it local Young's modulus) will be predetermined based on the macroscopic behavior (Figure VI.26).

In the previous chapter, we deduced that the local strain is governed by only fiber volume fraction *f*. We have conducted preliminary simulations by applying different relations between the global Young's modulus (obtained from global behavior of the CT-test) and the local Young's modulus. By intuition, the simplest relation is given based on the global behavior where the strain is linearly related to the fiber volume fraction under a polynomial relation such as:

$$E_i^k = E \times f_i^{k-1}; \qquad k = \overline{1,8} \tag{6.13}$$

and

$$E_i^k = E \times \left(f_i^{k-1} \right)^3; \qquad k = \overline{1,8} \tag{6.14}$$

where

E_i^k Young's modulus of *i*th element at studied state *k-1*

E Young's modulus obtained from global behavior, and $E = 8400Pa$

f_i^{k-1} Fiber volume fraction of *i*th element at previous compression state *(k-1)*

However the results obtained from Eq. (6.13) and Eq. (6.14) are improved by the following relations which give us the best results until now for our study whose results will be discussed in the next sections. Two other relations are proposed:

(i) First case: for any studied case *k*, local Young's modulus of *i*th element is the same as it is at the initial state or $E_i^k = E_i^0$ for Eq. (6.15) can be rewritten in this case as:

$$E_i^k = E \times \frac{f_i}{\overline{f_0}}; \qquad k = \overline{1,8} \tag{6.15}$$

where

f_i Fiber volume fraction of *i*th element

$\overline{f_0}$ Fiber volume fraction of the whole sample at the initial state

(ii) Second case: we suppose that the Young's modulus of each element is obtained from the Young's modulus from the global behavior as (Figure VI.26):